# PONTIFICIA UNIVERSIDAD CATÓLICA DEL PERÚ

## Escuela de Posgrado

# Contribution to the Tb-doped $\mathrm{AlN_xO_y}$:H/*c*-Si(p) interface study using Surface Photovoltage (SPV) techniques for potential photovoltaic applications

Tesis para obtener el grado académico de Doctor en Física que presenta:

*Jorge Alejandro Dulanto Carbajal*

Asesor:
*Prof. Dr. Jan Amaru Palomino Töfflinger*
Co-Asesor:
*Prof. Dr. Rolf Grieseler*

Lima, 2023

# Informe de Similitud

Yo, Dr. Jan Amaru Palomino Tofflinger, docente de la Escuela de Posgrado de la Pontificia Universidad Católica del Perú, asesor de la tesis de doctorado titulado "Contribution to the Tb-doped AlNxOy:H/c-Si(p) interface study using Surface Photovoltage (SPV) techniques for potential photovoltaic applications", del autor Jorge Alejandro Dulanto Carbajal, dejo constancia de lo siguiente:

- El mencionado documento tiene un índice de puntuación de similitud de 18 %. Así lo consigna el reporte de similitud emitido por el software *Turnitin* el 21/06/2023.
- He revisado con detalle dicho reporte y la Tesis o Trabajo de Suficiencia Profesional, y no se advierte indicios de plagio.
- Las citas a otros autores y sus respectivas referencias cumplen con las pautas académicas.

Lugar y fecha:
Lima, 22.06.2023

| | |
|---|---|
| Apellidos y nombres del asesor / de la asesora:<br>Palomino Tofflinger, Jan Amaru | |
| DNI: 48866095 | Firma |
| ORCID: https://orcid.org/0000-0002-2076-4046 | |

*To my loves ones...*

# Acknowledgements

I would like to start by thanking my advisors: Prof. Dr. Amaru Töfflinger, Prof. Dr. Rolf Grieseler, Dr. Steffen Fengler, and Dr. Thomas Dittrich. They shared their precious knowledge and time and gave me the opportunity to work in an exciting scientific field in collaboration with great German institutions. I would also like to thank Andres Guerra for his support and advice with nice explanatory classes. I cannot forget the whole group of materials science and renewable energies from PUCP, the old ones, the new ones, all of them. All of them have given me part of their valuable time. Also, the workshop guys, teachers and colleagues of the Physics section and the PUCP. Additionally, a special mention to our dean Prof. Dr. Francisco Rumiche for all the support to the group. Thank you very much colleagues!

I am very grateful for the financial support provided by the Peruvian PROCIENCIA (Contract N°124-2018-FONDECYT) and for the HUIRACOCHA Scholarship of the Pontificia Universidad Católica del Perú.

# Abstract

Hydrogenated Aluminum Oxynitride ($AlN_xO_y$:H) is a versatile material for the surface passivation of crystalline silicon (*c*-Si). The capability of having positive or negative fixed charges makes $AlN_xO_y$:H a suitable material for surface passivation of both n-type and p-type *c*-Si. Terbium (Tb) implemented in thin films is known for its potential for down-shifting light. This work studies the electronic properties of the Tb-doped $AlN_xO_y$:H/*c*-Si(p) interface. The studied samples' layers were deposited by reactive direct current (DC) sputtering with different hydrogen flows and then annealed.

Due to high leakage currents and high defect densities, the electronic properties of the Tb-doped $AlN_xO_y$:H layers could not be analyzed conclusively using standard techniques such as high-frequency capacitance-voltage (HF-CV) or quasi-steady-state photoconductance (QSSPC) measurements, respectively. As an alternative, the non-contact Surface Photovoltage (SPV) characterization technique enabled a profound investigation of the electronic features of the Tb-doped $AlN_xO_y$:H/*c*-Si (p) interface. Both modulated SPV and transient SPV measurements are performed. The capabilities of the SPV measurements make this technique unique and very effective in observing and measuring critical passivation properties of the Tb-doped $AlN_xO_y$:H samples.

Particularly the transient SPV of the Tb-doped $AlN_xO_y$:H samples enabled the observation of different optical transitions (band to band, band to defect, defect to band) and carrier transport mechanisms between the Si surface and the Tb-doped $AlN_xO_y$:H. The changes in relaxation times among Tb-doped $AlN_xO_y$:H samples are noticeable due to spatial separation among defects (tunneling).

This study uses complementary measurements like X-ray reflectometry (XRR), Photoluminescence (PL) and Fourier-transform infrared spectroscopy (FTIR) to obtain valuable information about the $AlN_xO_y$:H layer and the $AlN_xO_y$:H/*c*-Si(p) interface that validates the SPV results and observations. In the *c*-Si, through SPV, we observed strong accumulation with passivation of boron acceptors and the generation of defects near the interface. When the hydrogen flow was increased, the net negative charge in the Tb-doped $AlN_xO_y$:H layer decreased, and the surface photovoltage signals associated with defects increased. Transients SPV at higher hydrogen flows decayed faster, and hopping transport via an exponential distribution of trap states in energy replaced trap-limited relaxation of charge carriers separated in space.

The particular conditions that these $AlN_xO_y$:H samples have, make transient SPV spectroscopy a unique and reliable technique to observe the electronic properties of the $AlN_xO_y$:H/*c*-Si(p) interface.

# Resumen

El oxinitruro de aluminio hidrogenado ($\mathrm{AlN}_x\mathrm{O}_y$:H) es un material versátil para la pasivación superficial del silicio cristalino (*c*-Si). La capacidad de tener cargas fijas positivas o negativas hace del $\mathrm{AlN}_x\mathrm{O}_y$:H un material adecuado para la pasivación superficial de *c*-Si tanto de tipo n como de tipo p. El terbio (Tb) implementado en láminas delgadas es conocido por su potencial para desviar la luz hacia abajo. En este trabajo se estudian las propiedades electrónicas de la interfase ($\mathrm{AlN}_x\mathrm{O}_y$:H)/*c*-Si (p) dopada con Tb. Las capas de las muestras estudiadas fueron depositadas mediante sputtering reactivo DC con diferentes flujos de hidrógeno y posteriormente recocidas.

Debido a las elevadas corrientes de fuga y a las altas densidades de defectos, las propiedades electrónicas de las capas de $\mathrm{AlN}_x\mathrm{O}_y$:H dopadas con Tb no pudieron analizarse de forma concluyente utilizando técnicas estándar como las medidas de capacitancia-voltaje de alta frecuencia (HF-CV) o de fotoconductancia en estado cuasi estable (QSSPC), respectivamente. Como alternativa, la técnica de caracterización de fotovoltaje superficial (SPV) sin contacto permitió investigar en profundidad las características electrónicas de la interfaz $\mathrm{AlN}_x\mathrm{O}_y$:H/*c*-Si (p) dopada con Tb. Se realizan tanto medidas de SPV modulado como de SPV transitorio. Las capacidades de las medidas de SPV hacen que esta técnica sea única y muy eficaz para observar y medir las propiedades críticas de pasivación de las muestras de $\mathrm{AlN}_x\mathrm{O}_y$:H dopadas con Tb.

En particular, la SPV transitoria de las muestras de $\mathrm{AlN}_x\mathrm{O}_y$:H dopadas con Tb permitió observar diferentes transiciones ópticas (banda a banda, banda a defecto, defecto a banda) y mecanismos de transporte de portadores entre la superficie de Si y el $\mathrm{AlN}_x\mathrm{O}_y$:H dopado con Tb. Los cambios en los tiempos de relajación entre las muestras de $\mathrm{AlN}_x\mathrm{O}_y$:H dopadas con Tb son apreciables debido a la separación espacial entre defectos (tunelización).

Este estudio utiliza medidas complementarias como XRR, PL y FTIR para obtener información valiosa sobre la capa de $\mathrm{AlN}_x\mathrm{O}_y$:H y la interfase $\mathrm{AlN}_x\mathrm{O}_y$:H/*c*-Si (p) que valida los resultados y observaciones del SPV.

En el *c*-Si, mediante SPV, observamos una fuerte acumulación con pasivación de aceptores de boro y la generación de defectos cerca de la interfaz. Al aumentar los flujos de hidrógeno, disminuyó la carga negativa neta en la capa de $\mathrm{AlN}_x\mathrm{O}_y$:H dopada con Tb, y aumentaron las señales de fotovoltaje superficial asociadas a los defectos. Los transitorios SPV a mayores flujos de hidrógeno decaían más rápidamente, y el transporte por saltos a través de una distribución exponencial de estados trampa en energía sustituía a la

relajación limitada por trampas de portadores de carga separados en el espacio.

Las condiciones particulares que presentan estas muestras de $AlN_xO_y$:H hacen de la espectroscopia SPV transitoria una técnica única y fiable para observar las propiedades electrónicas de la interfase $AlN_xO_y$:H/*c*-Si(p).

# Contents

# List of Figures

# List of Tables

# Chapter 1

# Introduction

## 1.1 Improving Silicon Solar Cell efficiencies

Renewable energy sources are inexhaustible and follow natural cycles, unlike conventional energy sources such as coal, gas, oil, or nuclear energy. This makes them the key to creating a sustainable energy system that allows local development for future generations. Because it does not emit greenhouse gases during its production, renewable energy is an essential ally in mitigating society's impact on the environment.

The need for new clean energy sources makes photovoltaic energy one of the most promising energy sources for the future. Efficiency improvement is one of the significant challenges in photovoltaics [1]. Silicon is still the most used material for photovoltaic cell construction (around 85% of worldwide solar cell production) [2,3], and its efficiency relies mainly on surface passivation [4–7]. Silicon solar cells are advantageous options for solar cells that use just one semiconductor material due to the abundance of silicon, well-developed technology, and efficient match of the silicon absorption spectrum with the solar spectrum [8]. Surface passivation is composed of two processes achieved by a deposition of a thin layer (dielectric material): the reduction of defects at the silicon surface, known as *chemical passivation*, and the drift and separation of charge carriers in the silicon due to the presence of fixed charges at the passivation layer close to its interface with the silicon. This process is called *field effect passivation.* These two processes reduce the rate of free charge recombination and improve the collection of free charges at the respective contacts [4, 5] .

Depending on the type of doped silicon required to passivate, many materials are available for each n-type or p-type of doped silicon as passivation material. In passivating n-type silicon, the passivation layer should have fixed positive charges to repel holes and attract electrons). In contrast, the passivation layer in p-type silicon should have fixed negative charges to repel electrons and attract holes in the silicon. In this group of passivation materials, there are silicon dioxide ($SiO_2$) and silicon nitride ($SiN_x$), well-studied as n-type silicon passivation materials [9,10], aluminum oxide ($AlO_x$) well studied as p-type passivation material [11–13]. In contrast, a layer of aluminum nitride (AlN) could passivate n and p-type silicon due to its ability to exhibit positive or negative fixed charges, depending on the deposition and post-treatment parameters [14, 15].

In chemical passivation, the optimal materials are $SiO_2$ or $SiO_x$, which reduces the defects or dangling bonds at the interface silicon / passivator layer [9]. Amorphous silicon is another material that helps to passivate the defects efficiently at the crystalline silicon (absorption layer). This technique used is the so-called HIT solar cell [2,8]. Nevertheless, a good combination of field-effect and chemical passivation is required for efficient silicon passivation. In that sense, AlN is one of the most promising and not thoroughly studied materials as a passivation layer.

Silicon solar cells are close to the efficient limit. One possible way to overcome this limit is by using downshift or down-conversion layers. These layers could be done by adding a low dilution of Terbium atom to the passivation layer. The samples are doped with Terbium and exhibit photoluminescence under a 325 nm laser. The optical properties of these Tb-doped layers are well studied but the electronic properties of the interface are not studied before. The electronic properties are well described in this study and are the main subject of this thesis.

Other improvements using a Tb-doped $AlN_xO_y$:H passivation layer (not included in this study) are antireflective coatings, antireflective textures, back contact arrangements, and semiconductor heterojunctions [2] as well as concentrators [16].

## 1.2 Hydrogenated Aluminum Oxynitride ($AlN_xO_y$:H) for surface passivation

Hydrogenated aluminum nitride (AlN:H) thin films have demonstrated high potential as alternative anti-reflecting and passivating layers for crystalline silicon (*c*-Si) solar cells [14, 17–20]. This potential is due to their relatively high negative fixed charge (of the order of $-1 \times 10^{12}\,\mathrm{cm}^{-2}$), suitable for p-type silicon, and low density of interface states at the *c*-Si surface $5 \times 10^{10}\,\mathrm{eV}^{-1}\mathrm{cm}^{-2}$. Aluminum oxynitride ($AlO_xN_y$) has demonstrated similarly suitable passivation properties [21]. It has been shown that sputtered $AlO_xN_y$ layers can also serve as a host material for adequate luminescent emission from rear earth ions [22], bearing a high potential for optical down-conversion and downshift layer systems [23]. Furthermore, rare-earth doping for downshifting and down-conversion in other wide-bandgap semiconductor host materials was already shown and might increase solar cell efficiency even above the Shockley-Queisser limit. This is due to the possible use of parts of the solar spectrum that are commonly unavailable for silicon solar cells [24–26]. However, a reliable combination of the passivating properties of AlN:H and of $AlO_xN_y$ layers as hosts for luminescing rare-earth ions is still challenging. A practical reason can be the hydrogen's impact on the corresponding technological processes and the necessary annealing temperatures ranging between 500 °C and 1000 °C to achieve the rare-earth activation. The optical properties of AlN and $AlN_xO_y$ are well-studied [20, 22, 23, 27–29] but little is known about the electronic properties at the interface between these layers and silicon.

On one hand, hydrogen plays a vital role in numerous processes in semiconductor technology, for example, for passivation of recombination active defects at silicon interfaces [6, 30, 31] or in amorphous silicon [32] or for the formation of macroscopic defects after proton implantation for cutting silicon crystals [33]. In other host materials for luminescing rare-earth ions, such as hydrogenated amorphous silicon carbide, hydrogen enhances the optical bandgap of the host and reduces host-related luminescent centers, thus improving the excitation probability of rare earth ions [34, 35]. Polycrystalline hydrogenated AlN also experiences a similar behavior, the optical bandgap is enhanced through a reduction of Urbach tails, whilst the grain size is larger only for low hydrogen dilution conditions [20]. Hydrogen also passivates dopants in semiconductors and surface states affecting their electronic behavior [36–40]. In addition, hydrogen plasma treatment causes defect formation in bulk silicon and the formation of a disordered surface region at prolonged treatment, as shown by in-situ photocurrent and ellipsometry measurements [41].

Aiming towards developing a passivating layer functioning as a host for luminescing rare-earth ions, we studied defects at/near the *c*-Si and terbium-doped $AlN_xO_y$:H interface evolving during layer deposition and post-treatment. For this purpose, we applied transient surface photovoltage (SPV) spectroscopy. In comparison to the application of modulated or conventional SPV for studying surface passivation [15, 42], transient SPV spectroscopy provides information about transition energies and the role of defects in dynamic response [43, 44]. Furthermore, transient SPV spectroscopy can be even applied when other techniques such as high-frequency capacitance voltage and quasi steady-state photoconductance are strongly limited by high leakage currents or short lifetimes caused by high bulk or interface recombination rates [45, 46]. In contrast to the transient SPV spectroscopy we applied in this work, the conventional large signal SPV with varied applied potentials (see [23] and references therein) cannot be applied for the study of surface passivation for silicon surfaces covered with heavily charged layers.

Structurally, aluminum nitride (AlN) is a wide bandgap ceramic and semiconductor. AlN presents two crystalline systems (structures). The first is the cubic system (metastable) or zinc blende structure ($\beta$-phase, $a_0 = 0.436\,\mathrm{nm}$ at $300\,\mathrm{K}$). The second is the hexagonal system or also called wurtzite structure ($\alpha$-phase, $a_0 = 0.498\,\mathrm{nm}$ at $300\,\mathrm{K}$) which is the most stable crystal structure for this material [24–27]. The lattice constant of the AlN makes this material suitable for a passivation layer over silicon.

## 1.3 Surface Photovoltage Spectroscopy

Surface Photovoltage (SPV) Spectroscopy is a well-studied contactless technique for semiconductor characterization. SPV signals emerge when photogenerated charge carriers (electrons, holes) are spatially separated [51]. The fundamental processes of light absorption that cause mobile charge carriers photogeneration, charge carrier recombination, relaxation of a space charge disturbance and charge transport are crucial for SPV signals. All phenomena related to those processes can be studied mainly by SPV techniques [22, 23].

The SPV technique uses illumination-induced changes in the surface potential. During the last five decades, SPV has been used to obtain surface and bulk information on numerous semiconductors. SPV gives meaningful information as:

- Surface potential and flat band potential at semiconductor surfaces.
- Oxide thickness, oxide integrity, oxide charge and plasma damage at oxides deposited on surfaces.
- Minority carrier lifetimes, diffusion lengths and doping densities in bulk parameter [8, 22, 23].

All this information and relevant parameters depend on the photon energy (light wavelength) and the photon flux that induces the surface photovoltage (SPV) [8, 22, 23].

A surface photovoltage (SPV) variant, surface photovoltage spectroscopy (SPS), is a technique where the SPV signal changes are monitored as a function of the photon energy. The wavelengths range from below to above the bandgap spectral regions. Significant results that surface photovoltage spectroscopy (SPS) can obtain are the determination of energy gaps, density of states related features, electronic transitions at defect states, and band tails in semiconductors. For the development of this thesis, two main SPV techniques are used: the modulated SPV and the transient SPV. Both SPV techniques use a capacitor arrangement with the sample for its measurement. Modulated SPV has a better sensitivity, while transient SPV can measure several orders of magnitude in time (tens of nanoseconds to hundreds of seconds) for SPV processes observations in time (transitions, relaxation, and transport). More information about these two techniques is in the following chapters and [51]. Deeper details about the SPV fundamentals are in [22, 23, 29].

# Chapter 2

# Fundamental Theory

## 2.1 Surface Passivation on *c*-Si

Since silicon technology can produce ultra-high purity *c*-Si wafers, the primary source of solar cell efficiency losses comes from the *c*-Si surface [4, 5, 11, 55]. In order to reduce surface recombination losses, an insulator layer is placed on top of the *c*-Si surface. This passivation layer can contribute to two types of passivation mechanisms. One type is chemical passivation, and the second is field-effect passivation. Passivation aims to reduce the recombination of electrons and holes produced by illumination.

The field effect passivation separates the electron and holes due to an electric field originated by a distribution of positive or negative fixed charges presented at the passivation layer [56, 57].

The chemical passivation reduces the number of defects or dangling bonds that appear at the *c*-Si bulk's surface. Dangling bonds are centers of recombination where electrons or holes are trapped and facilitate the recombination with the opposite mobile charge carriers [4, 5, 58]. To reduce recombination losses, silicon dangling bonds at the surface are bonded to the atoms of the passivation layer.

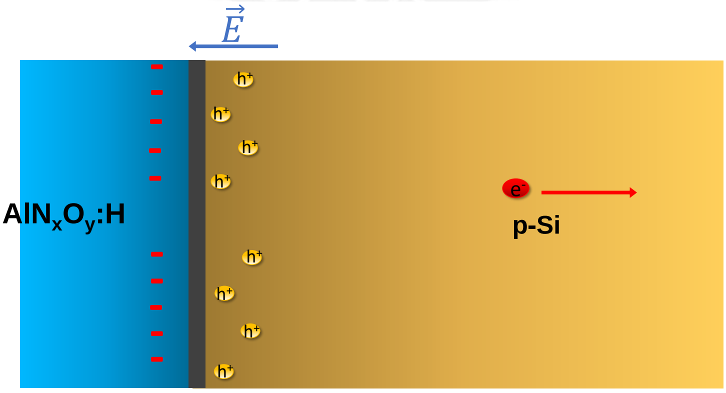

Figure 2.1: Depiction of field effect passivation (separation of charge carriers by an electric field). Holes are attracted by negative charges and the electrons are repelled.

Figure 2.1 shows the field effect passivation of a n-type *c*-Si. Fixed positive charges at the passivation layer attract electrons and repel holes separating them, reducing the possibilities of recombination of charge carriers.

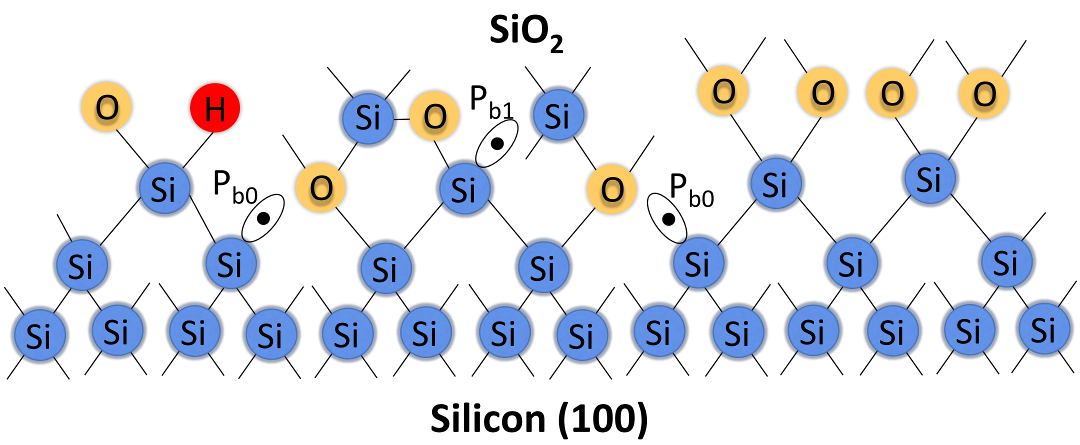

Figure 2.2: Depiction of chemical passivation (bonding of defects by passivation layer atoms or hydrogen atoms). $P_{b0}$ refers to dangling bonds from a silicon atom connected to other silicon atoms. $P_{b1}$ refers to dangling bonds from a silicon atom connected to silicon atoms and an oxygen atom.

Figure 2.2 shows the chemical passivation of a silicon surface by the bonding of Si dangling bonds with atoms of the passivation layer. This effect reduces the number of possible centers of recombination (dangling bonds), increasing the efficiency of the photovoltaic cell.

During surface recombination, electrons in the conduction band recombine with holes in the valence band at a defect level (*surface state*) within the bandgap. The Shockley Read-Hall (SRH) theory describes the process mathematically [59].

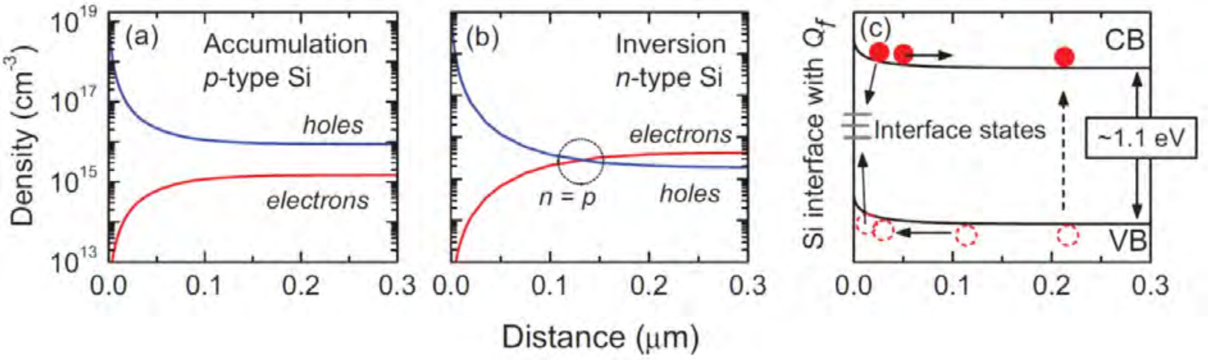

Figure 2.3: Electron and hole density below the Si surface for (a) p-type and (b) n-type Si under influence of a negative fixed surface charge of $Q_f = 2 \times 10^{12}\,\mathrm{cm}^{-2}$; (c) band bending under influence of $Q_f$ Data simulated by PC1D for 2× cm wafers under illumination in [60].

Figure 2.3 shows how a fixed negative interface charge $Q_f = 2 \times 10^{12}\,\mathrm{cm}^{-2}$ (in units of elementary charge) affects electron and hole densities near the surface of p-type and n-type silicon. The p-type Si exhibits accumulation condition at the surface due to a higher majority carrier density, whereas the n-type Si surface is inverted (Figure 2.3 (b)). Both cases are expected to exhibit a decrease in recombination due to a strong reduction in ns. In inversion conditions, electrons and holes are equally separated from the interface. An enhancement of recombination in the subsurface is expected when bulk defects are present. Figure 2.3 (c) shows the band bending due to charge at the surface. With ns strongly reduced, recombination can be expected to decrease in both cases. When the electrons and holes are inverted, the density becomes equal a distance away from the interface. Bulk defects can enhance recombination in the subsurface as a result of this phenomenon.

In this work, the analysis of passivation processes is studied under the scope of surface photovoltage (SPV) techniques where other conventional methods like high frequency capacitance-voltage (HF-CV) and quasi steady-state photoconductance (QSSPC) methods are not able to give conclusive information. Further information is developed in [4, 5, 56].

## 2.2 Surface Photovoltage (SPV)

### 2.2.1 Introduction

The fundamental principle of SPV signal generation is the separation of photogenerated charge carriers in space. A SPV signal depends on the processes of photogeneration of mobile charge carriers, recombination of charge carriers, charge transport, and relaxation of a disturbance of a space charge caused by light absorption. In photoactive materials, SPV techniques are generally applicable to investigate phenomena related to those fundamental processes.

A brief overview of photogeneration and recombination mechanisms is presented to understand the basis of surface photovoltage phenomena. The relaxation of a disturbance of a space charge by dielectric relaxation and by transport over a barrier is briefly explained for the transient SPV measurements. The SPV is defined as the negative charge of CPD due to illumination. For more extended information on the fundamentals, [51, 52] present a complete SPV theory.

### 2.2.2 Light Absorption and Recombination Processes

In the course of light absorption, the energy of a photon ($h\nu$) is converted into an increase of the energy of an electron ($E_e$). During the absorption event, the photon ($\gamma$) disappears. In photovoltaics and photocatalysis, light absorption is related to photon absorption from the sun. Sun photons have energies from the near-infrared (0.4–0.5 eV) to the ultraviolet (UV) range (4–5 eV).

During an absorption event, an electron is excited from an occupied into an unoccupied state at higher energy. Electronic states are occupied or unoccupied if their energy is below or above the Fermi energy ($E_F$), respectively. Photoactive materials are distinguished by their distributions of occupied and unoccupied states. Due to the overlap of wave functions, electronic states form extended states or bands at high densities. Charge carriers are mobile (or free) in extended states and not mobile (or trapped) in localized states. Absorption resulting in the excitation of charge carriers from states where they are not mobile into states where they are mobile is called photogeneration of free or mobile charge carriers. In solar cells, photogenerated electrons ($e^-$) are separated from an absorber at a charge-selective contact and their energy is converted into electric power at an external load. After that, the electrons flow back into the absorber at reduced energy. In photocatalysts, photogenerated electrons, for example, can be separated toward reactive sites where they participate in photocatalytic reactions.

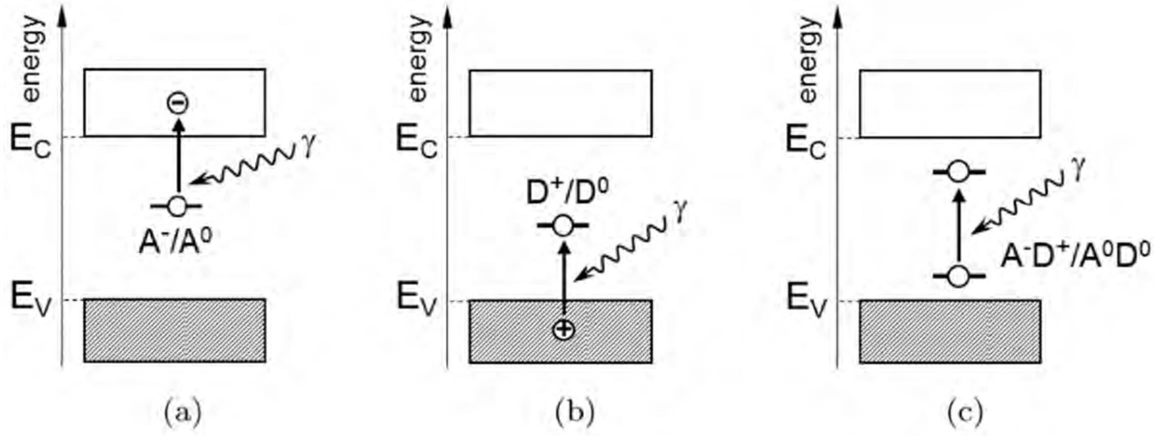

Figure 2.4: Schematic diagram of absorption events for photogeneration (a) of an electron from an occupied acceptor state, (b) of a hole from an unoccupied donor state, and (c) for excitation of an electron from an occupied acceptor into an unoccupied donor state. The diagram taken from [51].

A free electron can be photogenerated by the excitation of an electron from $A^-$ into the conduction band (Figure 2.4 (a)). A free hole can be photogenerated from an unoccupied donor state into the valence band (Figure 2.4 (b)). The excitation of an electron from $A^-$ into $D^+$ (Figure 2.4 (c))) does not result in the photogeneration of free charge carriers.

Recombination, i.e. the annihilation of free charge carriers, limits the density of free charge carriers in photoactive materials. As charge carriers recombine, their energy is transferred either to photons (radiative recombination), to another charge carrier (Auger recombination), or to vibrations of the lattice (Shockley–Read–Hall (SRH) and Surface recombination) [59, 61].

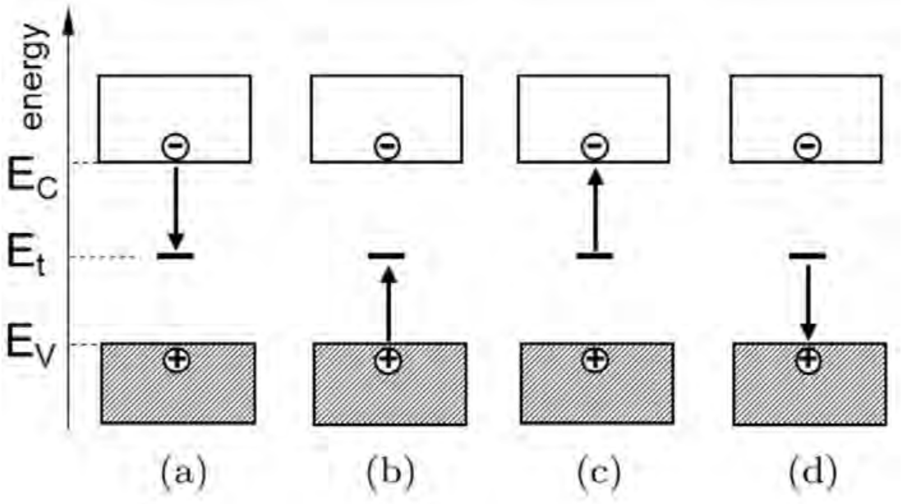

Figure 2.5: Elementary processes at a trap state in the band gap of a semiconductor: (a) capture of an electron from the conduction band at an unoccupied trap state, (b) capture of a hole from the valence band at an occupied trap state, (c) emission of an electron from an occupied trap state into the conduction band and (d) emission of a hole from an unoccupied trap state into the valence band. Depiction taken from [51].

Figure 2.5 (a) shows how an electron can be captured from the conduction band at an unoccupied trap state. Free electrons and free holes recombine non-radiatively via a trap state in both capture processes. The valence band can be occupied at a trap state to capture holes (Figure 2.5 (b)). Additionally, electrons can be emitted from occupied trap states into the conduction band (Figure 2.5 (c)) and holes from unoccupied trap states into the valence band (Figure 2.5 (d)).

### 2.2.3 Relaxation Rates of SPV Signals

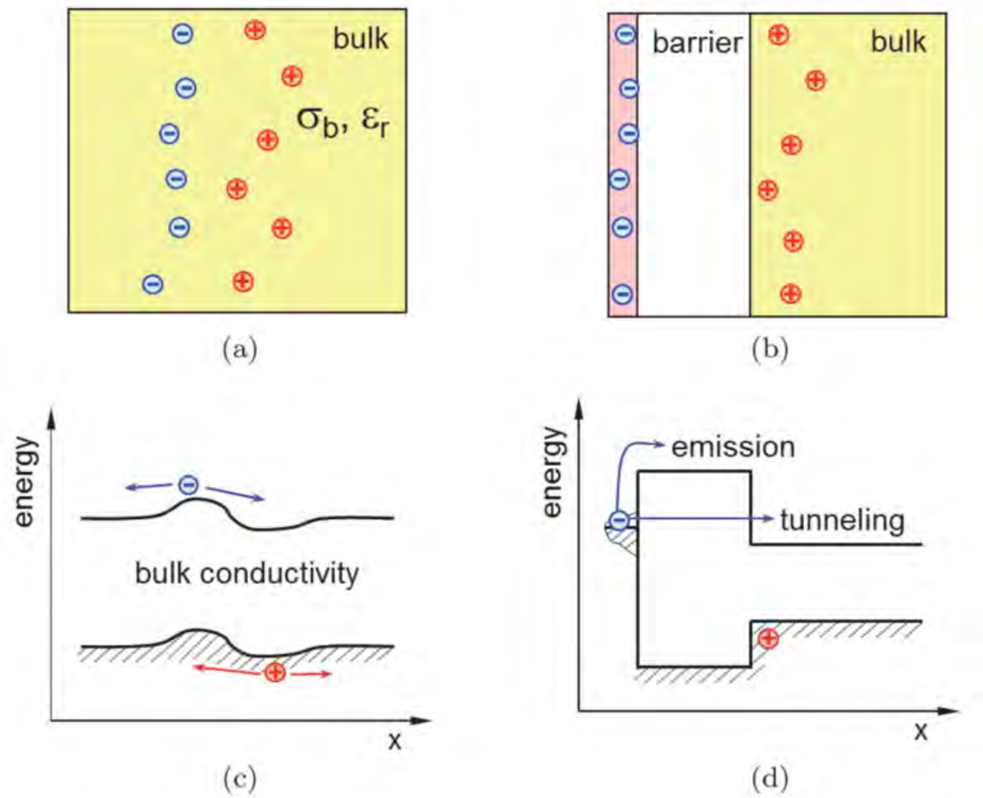

(a) (b) (c) (d)

Figure 2.6: Schematic diagram of a disturbance of a charge distribution from equilibrium due to charge separation in (a) a homogeneous bulk or (b) across a barrier and (c) schematic band diagrams depicting relaxation due to bulk conductivity or (d) due to charge transfer over a barrier by emission or through a barrier by tunneling. Figure taken from [51].

The space charge can be disturbed when photogenerated charge carriers are separated in space. For example, diffusion can disturb a space charge within the bulk of a photoactive material (Figure 2.6 (a)). The separation of a charge over a barrier can also disturb a space charge (Figure 2.6 (b)). Charge transport is limited by the bulk electrical conductivity of a photoactive material ($\sigma_b$, Figure 2.6 (c)). It is possible for charge carriers to overcome large barriers through thermally activated emission or tunneling if the barrier layer is extremely thin (Figure 2.6 (d)). SPV measurements can be used to investigate processes limiting the relaxation of photogenerated charge carriers separated in space.

### 2.2.4 Band Bending due to Illumination

SPV can also be referred to as changes in the band bending close to the interface or surface. Figure 2.7 (a), shows an intrinsic semiconductor. Under these conditions the bands are flat. Figure 2.7 (b) shows an n-type doped semiconductor at disequilibrium, $E_F$ (bulk) is closer to the conduction band. At this condition, the $E_F$(bulk) is higher than $E_F$(surf) under disequilibrium. To reach equilibrium electrons will transfer from the bulk to the surface ($E_F$(bulk) drops and $E_F$(surf) rises). The energy bands bend upward (Figure 2.7 (c)). Similarly, in Figure 2.7 (d), in p-type semiconductor, $E_F$(bulk) is lower than $E_F$(surf) under disequilibrium. The electron transfer will be from the surface to the bulk, producing a downward band bending (Figure 2.7 (e)).

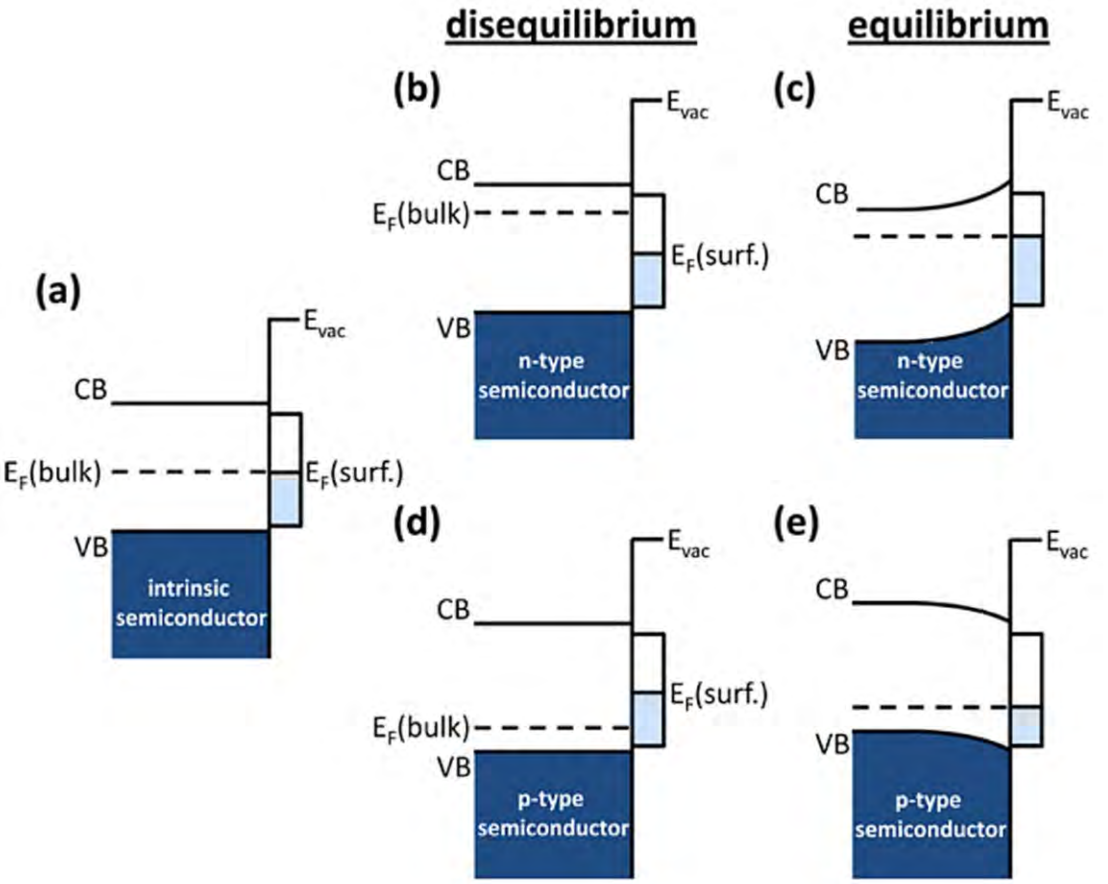

Figure 2.7: Schematic electron energy levels near the surface of a clean semiconductor: (a) undoped (intrinsic) semiconductor; (b) disequilibrium and (c) equilibrium between n-type bulk and its surface; (d) disequilibrium and (e) equilibrium between p-type bulk and its surface. Band diagrams taken from [66].

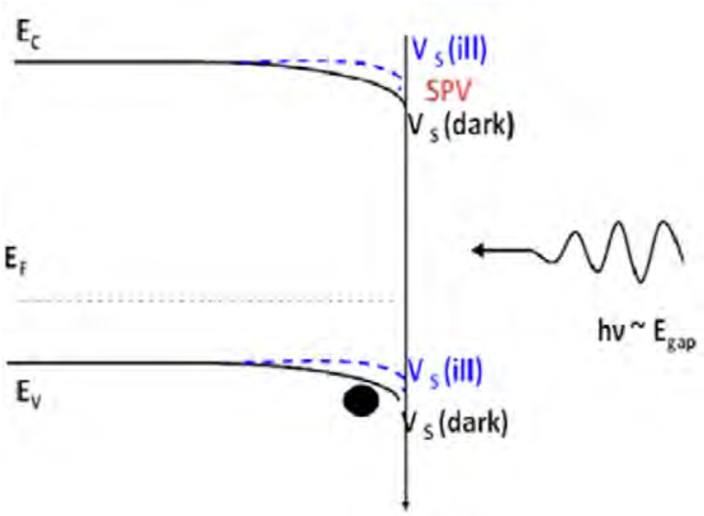

Figure 2.8: Band diagram of a p-type semiconductor close to the surface under illumination. Band diagram taken from [53].

At super-band gap illumination ($h\nu > E_{gap}$), the surface band bending decreases (Figure 2.8) for a p-type semiconductor. At photon energy equal to the band gap, the resulting SPV is negative for p-type semiconductors (downward band bending is positive by definition). The opposite is true for n-type semiconductors. The optical band gap can be calculated from this variation in the SPV spectrum.

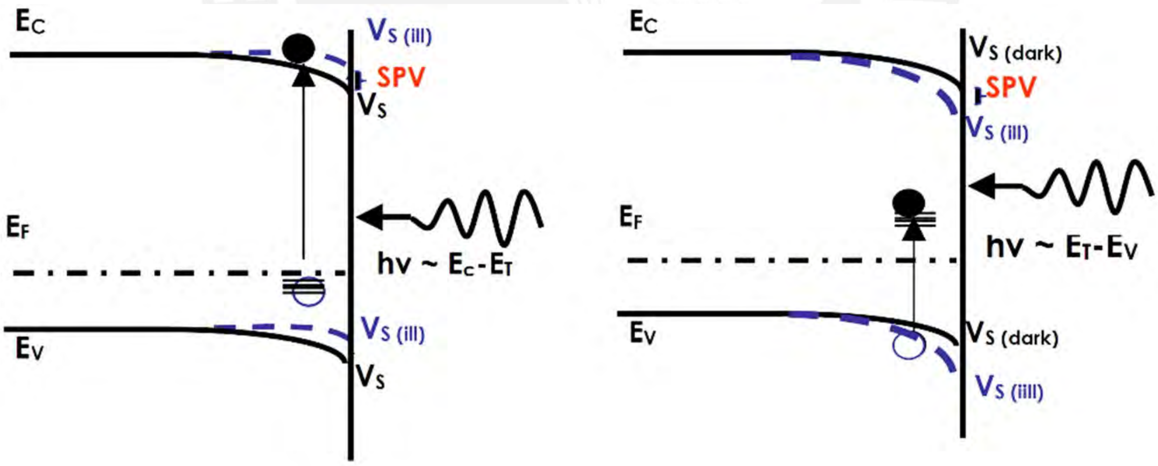

Figure 2.9: Band diagram of a p-type semiconductor close to the surface under below band gap illumination. Band diagrams taken from [53].

Figure 2.9 shows the two possibilities when an electron is promoted with a photon energy lower than the band gap. Figure 2.9 at left shows the transition of an electron from a trap state close to the valance band towards the conduction band. In this situation, the illumination tries to flatten the band (SPV is negative). The second situation is when an electron is promoted from the valance band to a trap state, producing a downward in the bands close to the surface producing a positive SPV.

### 2.2.5 Contact Potential Difference and Surface Photovoltage

Figure 2.10 shows how the contact potential difference, which is the difference of work functions between a reference electrode and a working electrode, changes with illumination. SPV is defined as the negative of the changes of CPD due to illumination.

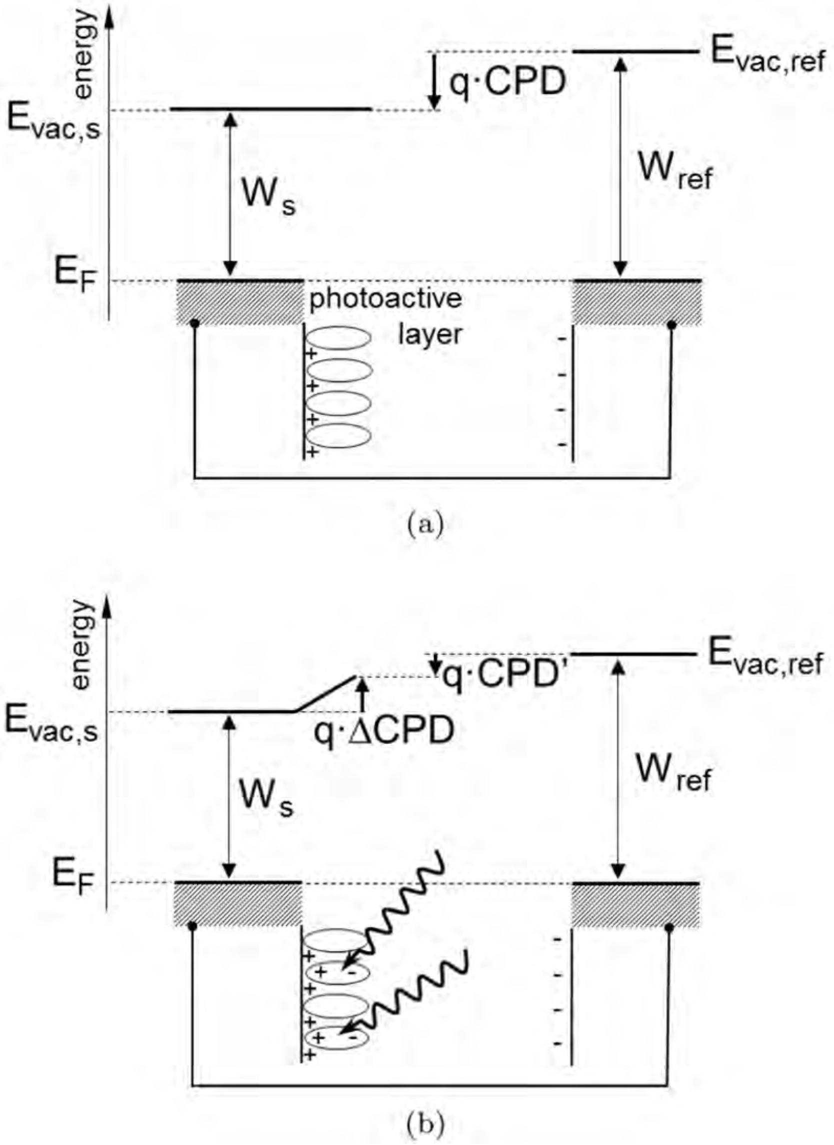

(a)

(b)

Figure 2.10: Schematic diagram of energies for a sample electrode coated with a photoactive layer and connected with a reference electrode in (a) the dark and (b) under illumination. $-\Delta$CPD denotes the change of the CPD due to the separation of photogenerated charge carriers in space. Depiction taken from [51].

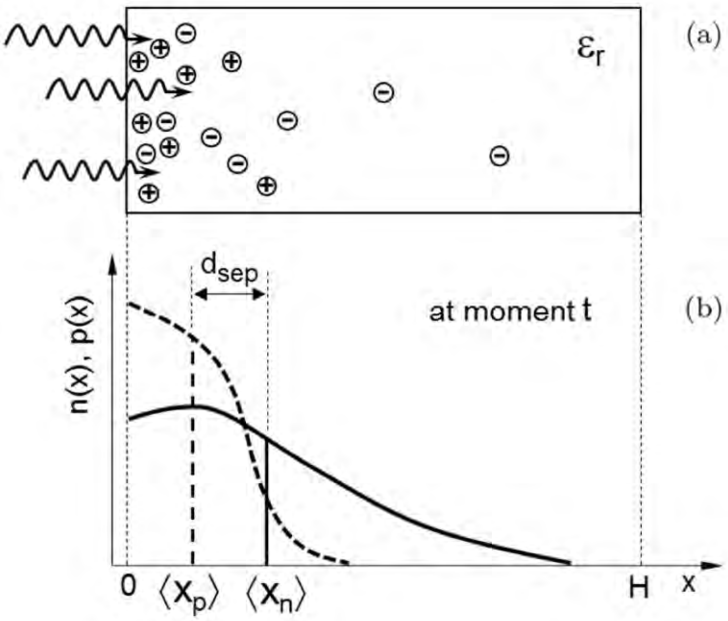

Figure 2.11: (a) Schematic diagram of positive and negative charge carriers in a homogeneous sample and corresponding distributions ($\Delta n(x)$ and $\Delta p(x)$, solid and dashed lines, respectively). (b) $\langle x_n \rangle$, $\langle x_p \rangle$, and $d_{sep}$ denote the centers of negative and positive charge and the charge separation length, respectively. Graphic taken from [51].

An important approximation for simplifying SPV analysis is to consider the centers of negative and positive charge. Figure 2.11 shows the centers of negative and positive charge from a homogeneous sample. This approximation also can be interpreted as a plate capacitor where the distance between the centers is the distance between plates.

Another important concept in SPV analysis is the superposition principle. The resulting measured SPV signals are the sum of all the processes involved. Isolate the processes involved is part of the transient SPV analysis done in Chapter 4.

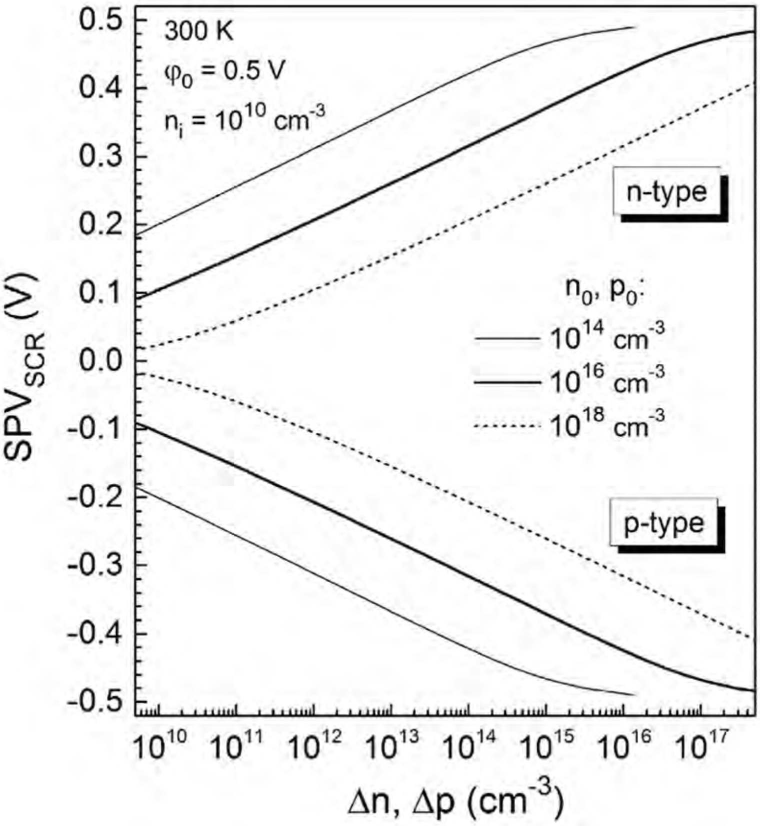

Figure 2.12: Dependence of SPV$_{SCR}$ on $\Delta n$ or $\Delta p$ for n- and p-type doped *c*-Si ($n_i = 10^{10}\,\mathrm{cm}^{-3}$) with $\phi_0 = 0.5$V and $n_0(p_0)$ equal to $10^{14}$, $10^{16}$ and $10^{18}\,\mathrm{cm}^{-3}$ (thin solid, thick solid and dashed lines, respectively). Plot taken from [51].

Figure 2.12 shows the dependence of SPV$_{SCR}$ on $\Delta n$ or $\Delta p$ and how it changes with the level of doping. This result will be useful for understanding later in Chapter 4 the passivation of boron-doped silicon atoms by hydrogen.

# Chapter 3

# Experimental Techniques

## 3.1 Sample Preparation

P-type doped *c*-Si(100) wafers (*c*-Si(p), resistivity 1-3 $\Omega$ cm) were coated with terbium doped $AlN_xO_y$:H layers by reactive DC-sputtering (LA 440S by Von Ardenne) from an Aluminum target (Sigma Aldrich, 9.95% purity) and pieces of Terbium (99.9% purity) for co-sputtering. These samples were used for the transient SPV measurements. Additionally, p-type CZ *c*-Si (111) wafers (resistivity 0.001-0.005 $\Omega$ cm) and p-type CZ *c*-Si (100) wafers (resistivity 1-3 $\Omega$ cm) were used for the modulated SPV measurements. The Aluminum target diameter was 3 inches and 0.125 inches in width at a 5 cm distance from the substrate. Three small Tb pieces were located on the Al target, to create a co-sputtering effect [67]. The Tb was placed in the sputter trace to enhance the deposition rate. The process was at 200 W and at constant Ar and $N_2$ flows of 80 and 20 sccm, respectively. The $H_2$ flows were 1, 3, and 5 sccm. The base pressure was $1.5 \times 10^{-5}$ Pa, and the working pressure was 1.0 Pa, keeping the chamber at room temperature (RT). All these conditions are presented in Table 3.1.

Fourier-transform infrared spectroscopy measurements to estimate the hydrogen bond density [35] confirmed the increase of hydrogen content in the different samples. The substrate was not heated during deposition, and the temperature stayed below 300 °C. The deposition rate is based on the experiments shown in [68]. The deposition time was about 240 s. The thicknesses of the Tb doped $AlN_xO_y$:H layers were obtained by x-ray reflection being 86, 88, and 74 nm for the samples with Tb-doped $AlN_xO_y$:H layers deposited at 1, 3, and 5 sccm $H_2$ flow, respectively. These conditions gave similar deposition rates of about 3.4 nm/s.

After the sputtering process, the samples were treated by rapid thermal processing (RTP) with a preheating at 200 °C and maximum temperature of 850 °C for 300 seconds to activate the luminescent properties of the embedded Tb ions [22, 23, 27, 68]. Such a thermal process can also activate fixed negative charges in the AlN layer for field-effect passivation [46, 69, 70].

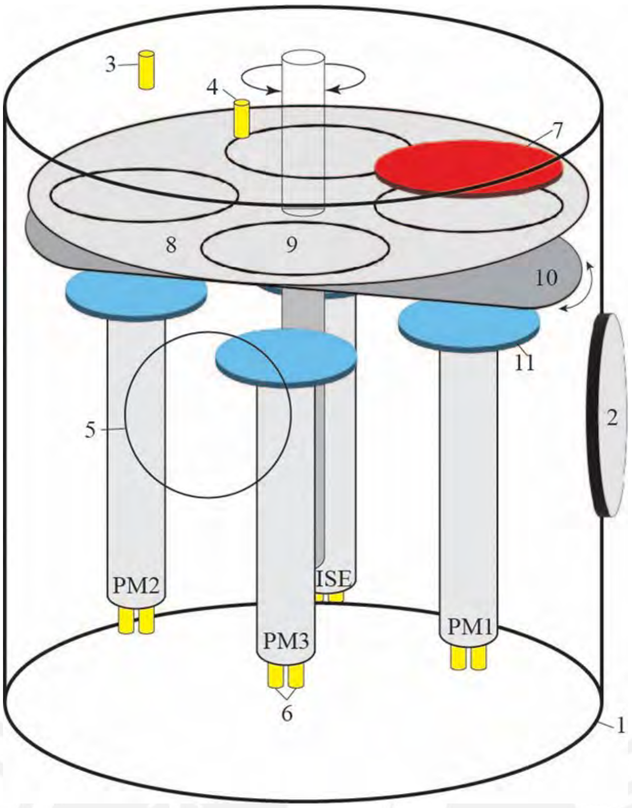

Figure 3.1: Schematic of DC-sputtering with four sample-holders [71].

Figure 3.1 shows the schematics of the sputtering equipment used for the sample preparation. In this equipment, a single target can be used at a time. Four rotative sample holders can be used to perform the sputtering processes.

| Code | Large code | Target | Power (W) | Nitogen flow (sccm) | Hidrogen flow (sccm) | Temperature at chamber |
|---|---|---|---|---|---|---|
| S-18 | Al-Tb-20N-1H-RT | Al+Tb | 200 | 20 | 1 | RT |
| S-19 | Al-Tb-20N-3H-RT | Al+Tb | 200 | 20 | 3 | RT |
| S-20 | Al-Tb-20N-5H-RT | Al+Tb | 200 | 20 | 5 | RT |

Table 3.1: Sputtering deposition conditions of samples.

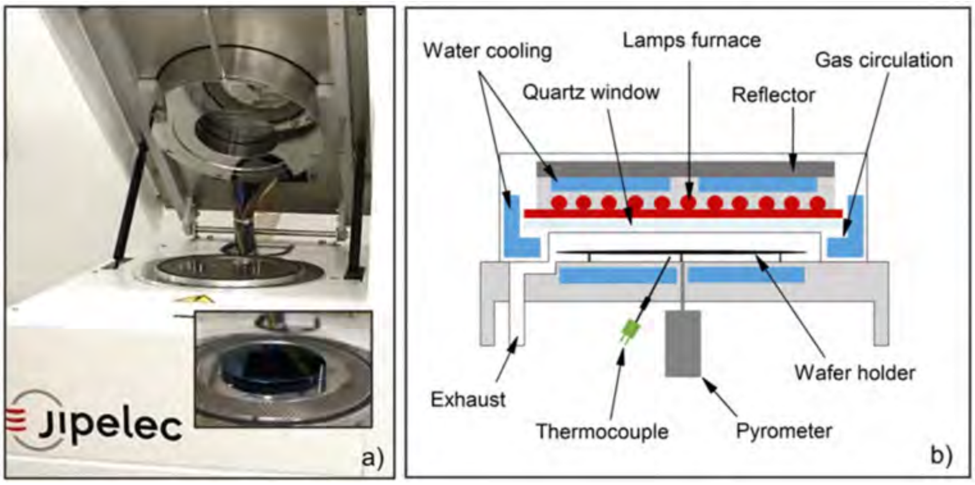

Figure 3.2: Rapid thermal annealing apparatus (Jipelec JetFirst RTA furnace)

Figure 3.2 shows the RTA furnace used to anneal the samples and activate the negative fixed charges and the terbium ions for luminescence.

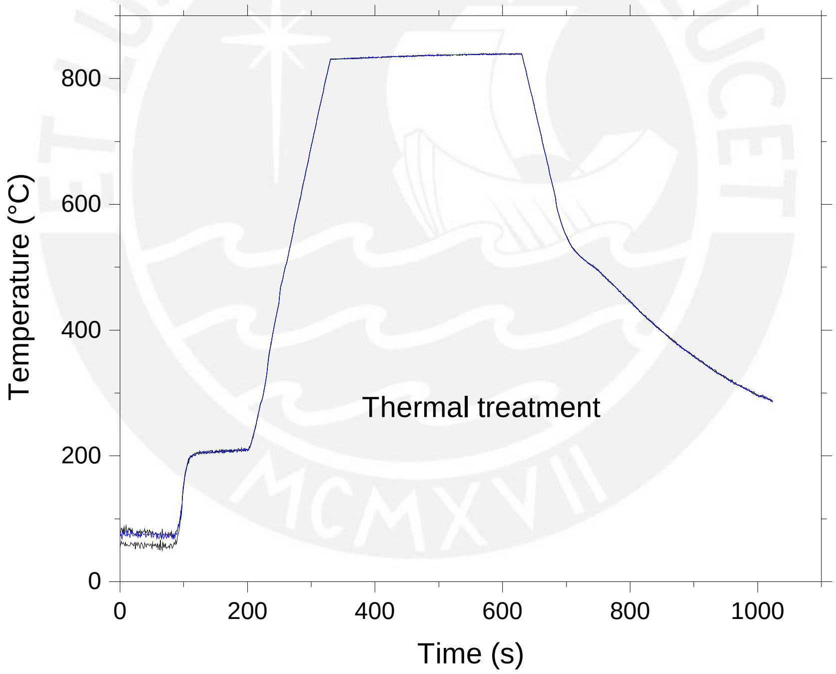

Figure 3.3: Rapid thermal annealing temperature response of AlN$_x$O$_y$:H/$c$-Si(p) samples.

Figure 3.3 shows the temperature versus time for the RTA of the AlN$_x$O$_y$:H/$c$-Si(p) samples. The maximum temperature (850 °C) was kept for 300 seconds.

## 3.2 Surface Photovoltage Techniques

In the present study, the modulated and the transient SPV techniques are used to analyze the interface properties of the $AlN_xO_y$:H/*c*-Si(p) samples. These two techniques are based on the capacitive out-coupling of SPV signals. Figure 3.4 depicts this capacitive out-coupling arrangement [51].

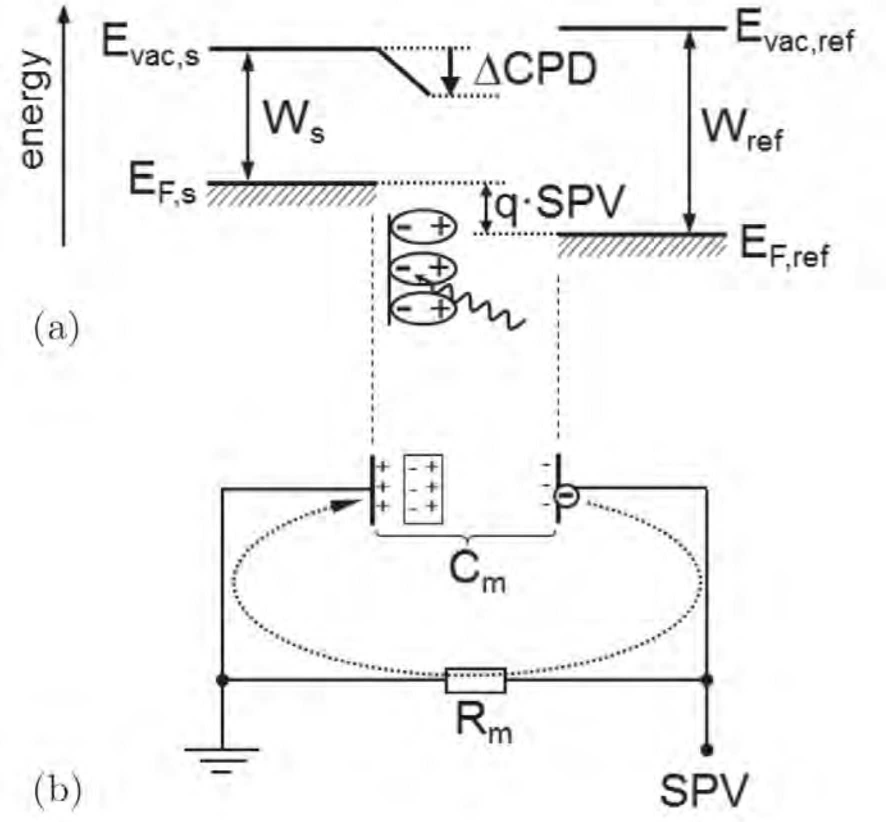

Figure 3.4: Energy scheme of (a) a reference electrode and a sample electrode with a photoactive layer under illumination and (b) simplified equivalent circuit for capacitive out-coupling of SPV signals. Figure and captions from [51]. In this diagram, $E_{vac,s}$ is the semiconductor vacuum energy at the surface, $E_{F,s}$ is the semiconductor Fermi energy at the surface, $E_{F,ref}$ is the reference electrode Fermi energy at the surface $\Delta CPD$ is the change of the contact potential difference, $W_s$ is the work function of the semiconductor, $W_{ref}$ is the work function of the reference electrode, $E_{vac,ref}$ is the reference electrode vacuum energy, $C_m$ is the measurement capacitance and $R_m$ is the measurement resistant.

In order to obtain the SPV signal under this configuration, it is necessary to have a very high impedance. In capacitance-resistor circuits, the discharge of the capacitor has a $R_mC_m$ as a time constant. In the case of the transient SPV, it is possible to measure SPV signals at times shorter than the $R_mC_m$ time constant.

### 3.2.1 Modulated Surface Photovoltage Spectroscopy

Modulated SPS measurements were performed using a MIS capacitor setup with a prism monochromator and a halogen lamp [72], as depicted in Figure 3.5. At the MIS configuration the modulated SPS method is very sensitive to small SPV signals (up to the $<100\,\text{nV}$) [52]. To reduce stray light effects, a cut-off filter was included between the exit slit of the monochromator and the mechanical chopper (modulation frequency 8 Hz). The SPV signals were detected with a double-phase lock-in amplifier (EG&G 5210).

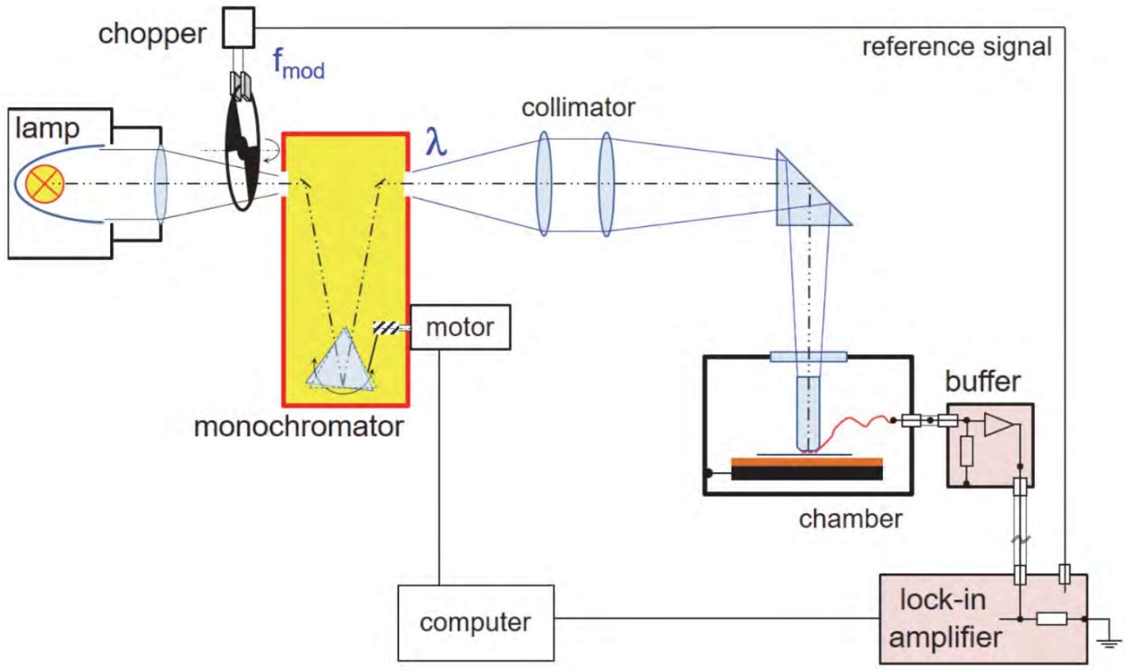

Figure 3.5: Schematic setup for modulated SPV. Adapted from [51].

Any monochromator has *white* stray light which is usually suppressed by about 3 orders of magnitude at a given wavelength. First, stray light can cause SPV signals in spectral regions without any absorption, i.e. stray light can cause artefacts. Second, SPV signals caused by stray light very drastically reduce the sensitivity for signals related to very weak photogeneration as for defect states in the band gap. The purpose of the cut-off filters is to eliminate the stray light [72, 73], i.e. non-monochromatized light originating from the monochromator.

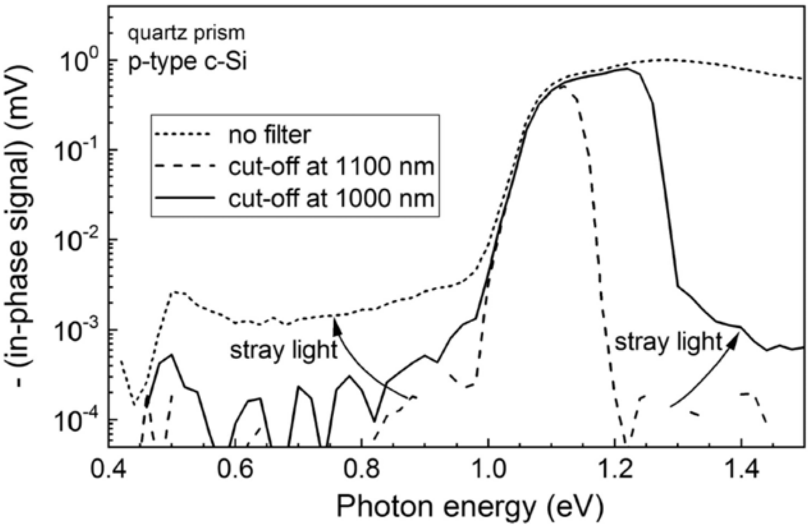

Figure 3.6: Modulated spectra of the negative in-phase SPV signals of moderately p-type doped *c*-Si measured without a filter (short dashed line) and with long-pass filters with cut-off wavelengths at 1000 and 1100 nm (dashed and solid lines, respectively) [51].

Figure 3.6 shows the effect of reducing the stray light by using a long-pass filter. In this example, two long-pass filters are used: a 1000 and 1100 nm of cut-off wavelength.

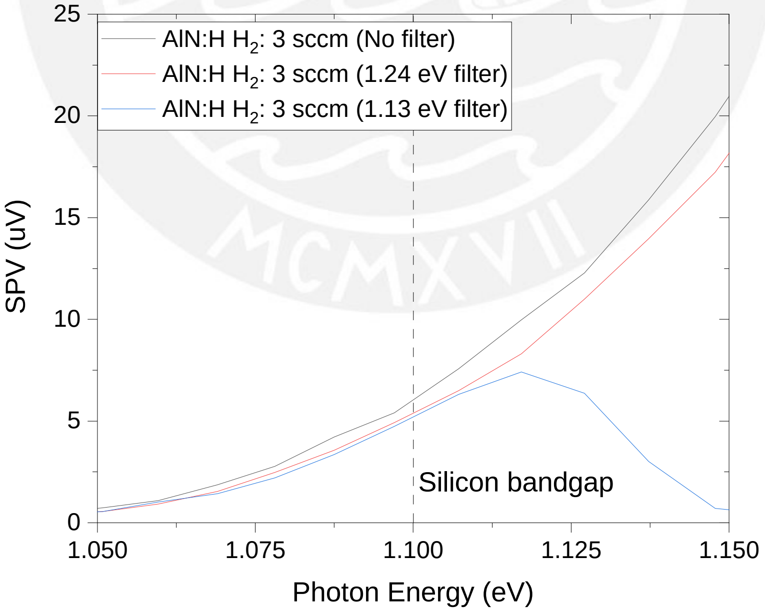

Figure 3.7: Modulated SPV spectra near the band gap of *c*-Si measured for the bare substrate without and with cut-off filters (no filter, 1000 nm, 1100 nm - black, red and blue lines, respectively) [15].

Figure 3.7 shows SPV spectra near the bandgap for the bare *c*-Si substrate (used for the fabrication of the samples in this study) without and with using cut-off filters at 1000 nm and 1100 nm (1.24 eV and 1.13 eV, respectively). The shapes of the spectra were unchanged below the cut-off energies whereas the signal heights were reduced by additional optical losses and reduced stray light. Since the absorption coefficient of *c*-Si strongly increases between 1.13 eV and 1.24 eV, the filter with the cut-off at 1100 nm has been used in the following.

### 3.2.2 Transient Surface Photovoltage

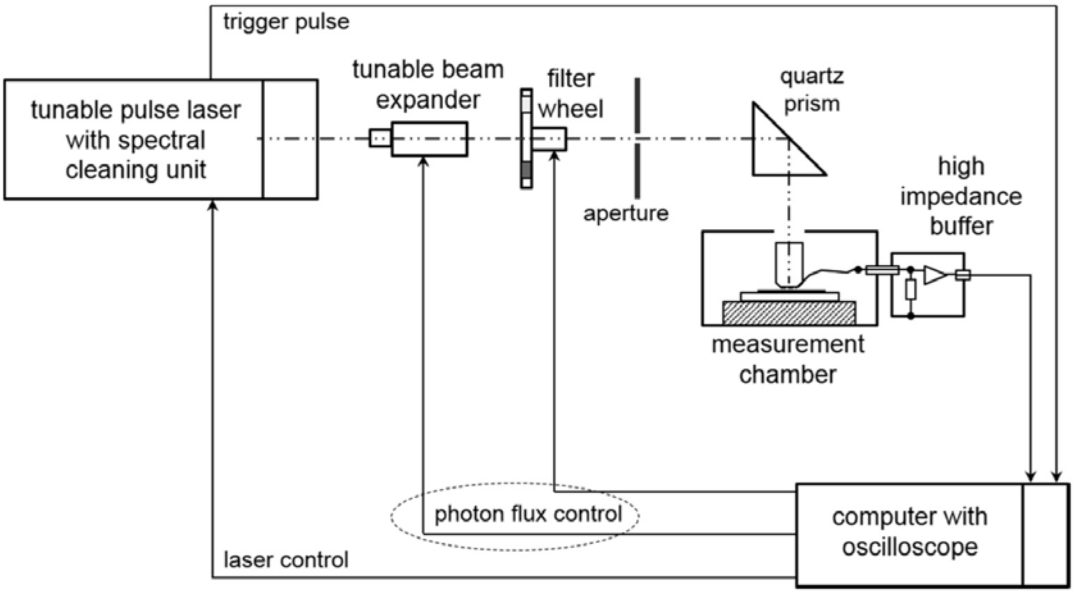

Figure 3.8: Schematic setup for transient SPV at constant photon flux [44].

Figure 3.8 shows the transient SPV setup. It consists of a tunable pulse laser, a tunable beam expander for the generation of a fixed photon flux. The measurement chamber is in the capacitive out-coupling mode. In this configuration, the light-induced potential drop across a parallel plate capacitor with high-impedance buffers (fixed capacitor techniques), and the signal is registered in a computer with an oscilloscope. For more details of the configuration setup, see [44].

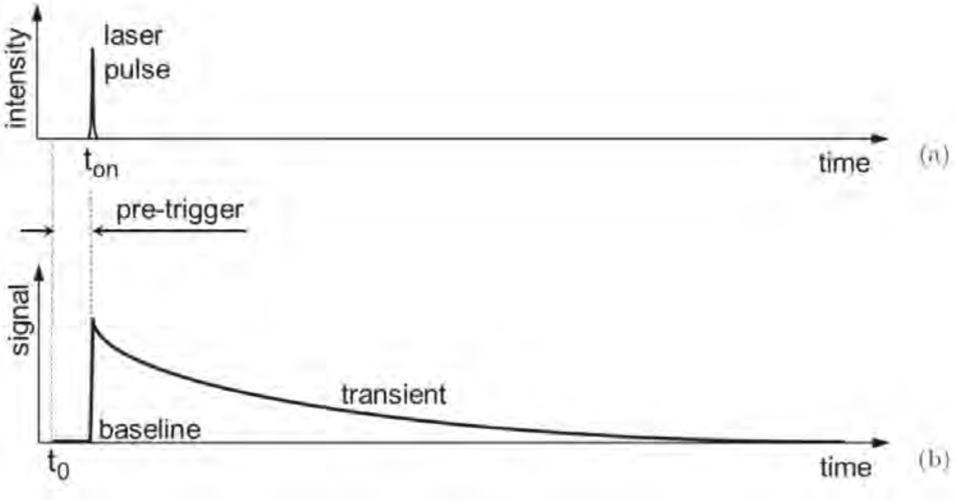

Figure 3.9: Schematic diagram of (a) exciting laser pulse and (b) corresponding SPV transient. For determining the baseline, a pre-trigger time $t_{on}$-$t_0$ has to be set on the oscilloscope ($t_{on}$ and $t_0$ denote the time when switching on the laser and when starting the measurement, respectively). Plot taken from [51].

Figure 3.9 shows the SPV signal evolution produced by the pulse laser. The SPV transient after the laser pulse is present after a pre-trigger time of 75 ns at the study of the $\mathrm{AlN}_x\mathrm{O}_y$:H/*c*-Si(p) samples.

The transient SPV spectroscopy is the main experimental technique where the information obtained from the $\mathrm{AlN}_x\mathrm{O}_y$:H/*c*-Si(p) interfaces is abundant due to the ternary measurements that involve SPV signal, time and photon energy (chapter 4). From this data, SPV curves can be obtained by photon energies or relaxation times cuts. From this data is possible to obtain SPV curves by photon energies or by relaxation times. At the SPV curves by relaxation time further analysis can be done in order to obtain information about tail energies and deep defects at / close to the $\mathrm{AlN}_x\mathrm{O}_y$:H/*c*-Si(p) interfaces. This extensive analysis is shown in detail in sub-chapter 4.3 and in [74].

# Chapter 4

# Analysis of Terbium doped $AlO_xN_y$:H on $c$-Si(p) interface

## 4.1 Introduction

This chapter deeply analyzes the electronic properties of the $AlN_xO_y$:H layer and the $AlN_xO_y$:H/$c$-Si(p) interface with different hydrogen flows at deposition (1 sccm, 3 sccm, and 5 sccm). For this purpose, this chapter starts with complementary measurements: Fourier Transform Infrared (FTIR), Energy Dispersive X-ray (EDX), X-ray Reflectometry (XRR), and Photoluminescence (PL). These techniques are used to estimate hydrogen content and analyze element composition, thickness, superficial roughness, interfacial roughness, density, and emission activation of terbium ions at the Tb doped $AlN_xO_y$:H layers at the $AlN_xO_y$:H layer.

Taking into account these complementary measurements, two experimental techniques: the modulated surface photovoltage (modulated SVP) and the transient surface photovoltage (SPV) are performed to analyze in detail the electronic properties of the $AlN_xO_y$:H/$c$-Si(p) interface. Modulated SPV detects the presence of defect state energies and tail states energies due to its high resolution at variations in SPV signals. At the same time, transient SPV adds crucial information about the dynamics of charge transfer, transitions, relaxation of charge carriers, and most processes related to charge carriers separated in space [51].

Transient SPV provides essential information about how the hydrogen affects the optical, electronic, and structural properties of the $AlN_xO_y$:H/$c$-Si(p) interface. Since the SPV techniques measure the superposition of all processes that involve SPV signal generation (charge carrier separation in space) [51], this study aims to identify and separate parallel processes that hydrogen impacts on the interface properties.

Subsection 4.3 shows and analyzes the different information that transient SPV provides for presenting some conclusions. This study reinforces the vast capability of transient SPV to analyze buried interfaces.

## 4.2 Complementary measurements - Further material property study

The estimation of the hydrogen content at the Tb-doped AlN$_x$O$_y$:H layer is done with Fourier Transform Infrared (FTIR) measurements. This study uses Energy Dispersive X-ray (EDX) for the elemental composition. The thickness, superficial roughness, interfacial roughness, and density are measured by X-ray Reflectometry (XRR). The activation of terbium ions at the Tb-doped AlN$_x$O$_y$:H layers for optical emission is verified by Photoluminescence (PL) measurements. Additionally, modulated SPV is used as a complementary measurement technique to obtain a first idea of the electronic properties of the AlN$_x$O$_y$:H/*c*-Si interface.

### 4.2.1 Hydrogen Content: Fourier Transform Infrared (FTIR) measurements

FTIR measurements were carried out using an infrared spectrometer FTIR model Spectrum 1000 from Perkin Elmer (resolution: 8 cm$^{-1}$). The FTIR measurements allow determining the number of bonds related to hydrogen inside the bulk of the AlN$_x$O$_y$:H layer. Other measurements, like Energy Dispersive X-ray (EDX), cannot measure the amount of hydrogen inside the AlN$_x$O$_y$:H bulk due to its light atomic weight. The method used to calculate the hydrogen bond is described in detail in [35].

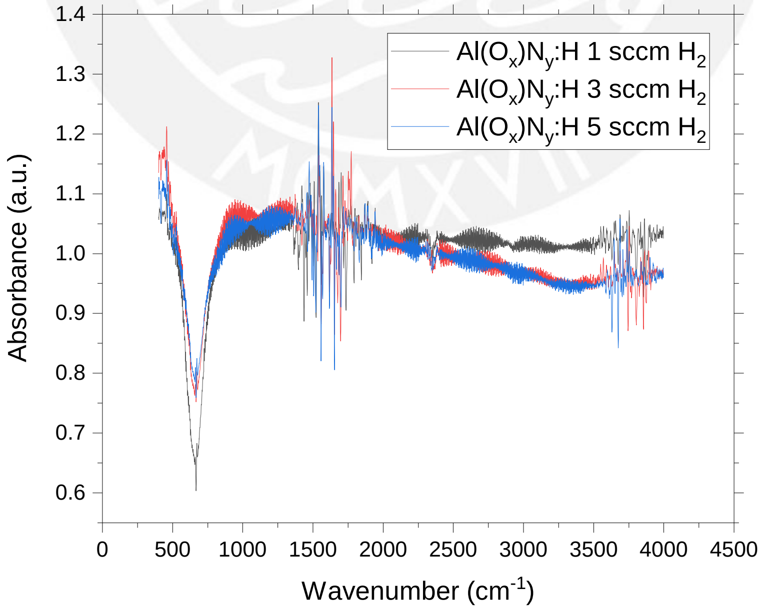

Figure 4.1: Original FTIR measurements of the AlN$_x$O$_y$:H layers for the 1, 3, 5 sccm of H$_2$ flow at deposition

Figure 4.1 shows a relatively high distortion of the FTIR measurements. It is necessary to apply a Fourier filter (low pass) to obtain viable curves, as shown in Figure 4.2. From these curves, the calculation of the hydrogen bonds is possible. This distortion is likely due to topographic changes at the silicon surface by hydrofluoric acid dip [75,76].

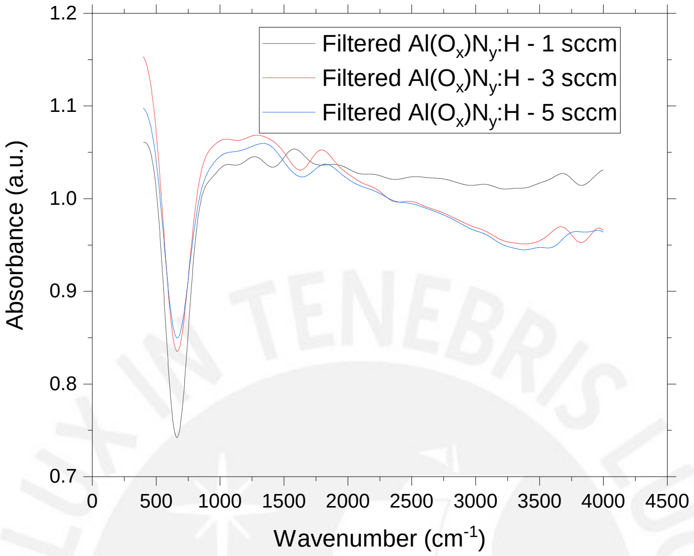

Figure 4.2: FTIR measurements after a Fourier filter (low pass). Fast variations over the FTIR signals are eliminated. Three vibration modes of Al-N, Al-O and Al-O-Al modes at 654 $\mathrm{cm}^{-1}$, 561 $\mathrm{cm}^{-1}$ and 764 $\mathrm{cm}^{-1}$, respectively are presented at the FTIR measurements. There is a broad band from 2900 $\mathrm{cm}^{-1}$ to 3800 $\mathrm{cm}^{-1}$ is due the H-O vibrations modes.

The absorbance is calculated from the FTIR data in Figure 4.3.

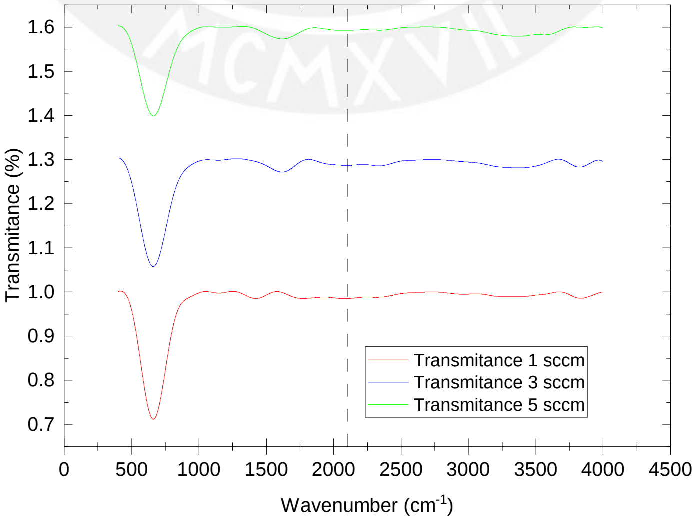

Figure 4.3: Calculated transmittance from FTIR.

To estimate the number of hydrogen bonds, the $\mathrm{AlN}_x\mathrm{O}_y$: H thickness must be included to calculate the absorption coefficient. The resulting absorption coefficients are divided by the wavenumber to normalize the function. Following the procedure described in [35], it is possible to obtain an estimation of the hydrogens bond at the $AlN_xO_y$:H layer (Figure 4.4).

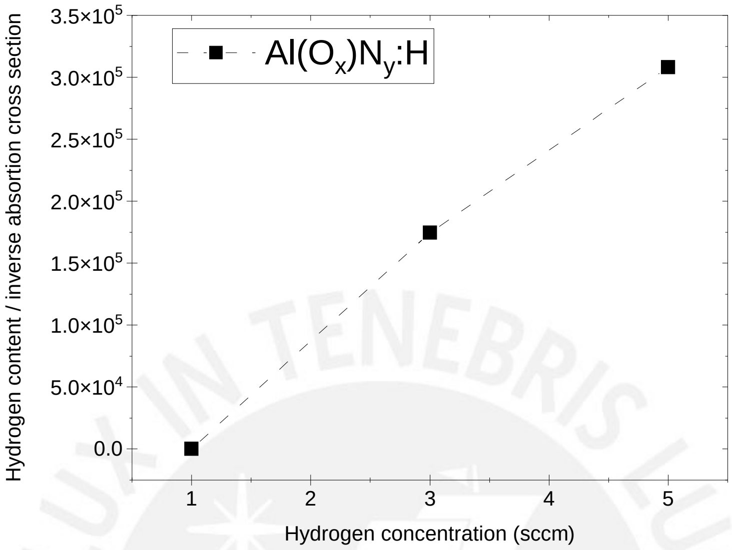

Figure 4.4: Hydrogen content (number of hydrogen bonds)

As a result, an estimated number of hydrogen bonds is presented for the three samples (Figure 4.4). The amount of hydrogen bonds increases with the hydrogen flow introduced at deposition. This result indicates the amount of hydrogen at the bulk of the $AlN_xO_y$:H layers. The passivation inside the $AlN_xO_y$:H layers bulk by hydrogen could reduce some bulk defects, but there is no indication from this FTIR measurement about the passivation or defect distribution at/near the interface $AlN_xO_y$:H/*c*-Si.

### 4.2.2 Energy Dispersive X-ray (EDX) measurements

For the element composition, an energy-dispersive X-ray spectroscopy (Octane Pro by EDAX) inside a scanning electron microscope (FEI Quanta 650) chamber was used. The acceleration voltage ($V_{acc}$) was set as 3 kV, because an efficient acceleration voltage should be at least $V_{acc} > 2E_C$, where $E_C$ is the minimum emission voltage ($E_C(Al) = 1.486\,\text{keV}$, $E_C(N) = 0.392\,\text{keV}$, $E_C(O) = 0.525\,\text{keV}$, $E_C(Tb) = 1.240\,\text{keV}$) and the thicknesses of the $\text{AlN}_x\text{O}_y$:H layers are thinner than 100 nm and a higher acceleration voltage could penetrate the substrate.

The composition of the $\text{AlN}_x\text{O}_y$:H layer is obtained by the EDX. The variation of the relative amount of the elements (Al, N, O, and Tb) among samples is shown in the following table.

| | Al (% at) | N (% at) | O (% at) | Tb (% at) |
|---|---|---|---|---|
| 1 sccm (H flow) | 47.16 | 34.59 | 17.91 | 0.34 |
| 3 sccm (H flow) | 44.62 | 28.68 | 26.46 | 0.29 |
| 5 sccm (H flow) | 44.45 | 25.66 | 29.51 | 0.39 |

Table 4.1: Atomic percentage of the elements at the $\text{AlN}_x\text{O}_y$:H layers.

From Table 4.1, the N content decreases from 34.59% to 25.66%; the O content increases from 17.91% to 29.51% when the hydrogen flow rate at deposition increases. On the other hand, aluminum content slightly changes from 47.16 %to 44.45 % when the hydrogen flow rate at deposition increases. These three surfaces have different element content giving the possibility of three different $\text{AlN}_x\text{O}_y$:H interfaces. In the case of the hydrogen content, the FTIR analysis was necessary because EDX measurements can not detect light elements like hydrogen.

### 4.2.3 X-ray reflectometry (XRR) measurements

The equipment used for X-ray reflectivity measurements was a D8 DISCOVER diffractometer from Bruker. The diffractometer is operated in the configuration $\theta/\theta$. the X-ray beam is produced in a copper source (Cu-radiation, K$\alpha$=1.5406 Å) with an accelerating voltage of 40 kV and filament current of 40 mA. XRR measurements are performed to obtain information on important properties of the $\text{AlN}_x\text{O}_y$:H layer and the $\text{AlN}_x\text{O}_y$:H / *c*-Si(p) interface. These properties are thickness, density, the surface roughness of the $\text{AlN}_x\text{O}_y$:H layers, and interface roughness of the $\text{AlN}_x\text{O}_y$:H / *c*-Si(p) interface. Figure 4.5 shows the results for the three samples.

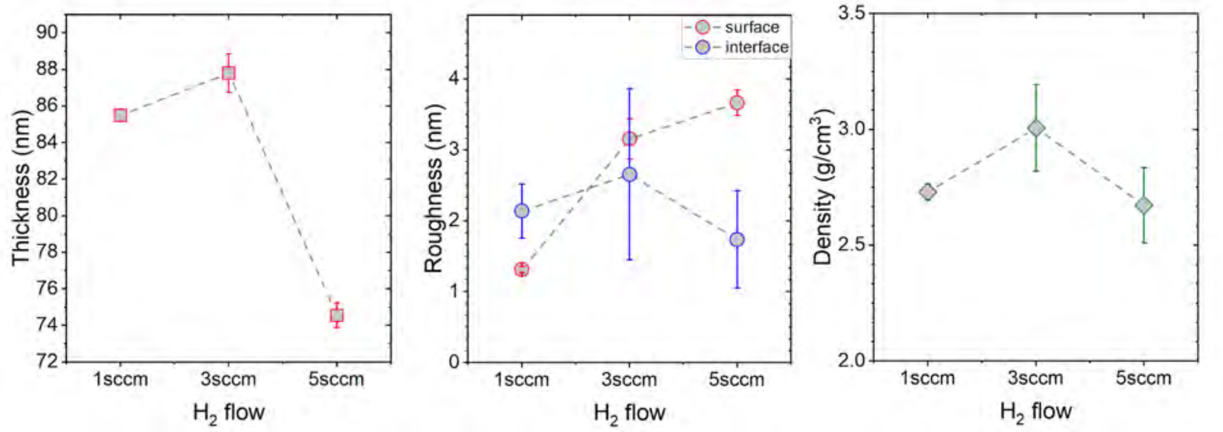

Figure 4.5: Plots of thickness, roughness, and density by XRR spectroscopy ($AlN_xO_y$:H layers and $AlN_xO_y$:H/*c*-Si interfaces).

Table 4.2 shows the values of the properties measured by XRR. One significant result is that the layer thicknesses are about the same, from which we can assume that photogeneration is similar in the three samples. The roughness of the surface increases while the $H_2$ flow. The interfacial roughness ($AlN_xO_y$:H/*c*-Si) and the density of the $AlN_xO_y$:H layer did not show a tendency with $H_2$ flow. The variation on the $H_2$ did not change considerably the values of the layer density.

| Sample | Thickness | ± | Superficial Roughness | ± | Interfacial Roughness | ± | Density | ± | $\chi^2$ |
|---|---|---|---|---|---|---|---|---|---|
| | [nm] | | [nm] | | [nm] | | [g/cm$^3$] | | |
| 1 sccm ($H_2$) | 85.4 | 0.3 | 1.3 | 0.04 | 2.1 | 0.39 | 2.7 | 0.03 | 1.9E-01 |
| 3 sccm ($H_2$) | 87.8 | 1.1 | 3.2 | 0.28 | 2.7 | 1.20 | 3.0 | 0.19 | 1.9E-01 |
| 5 sccm ($H_2$) | 74.6 | 0.7 | 3.7 | 0.18 | 1.7 | 0.68 | 2.7 | 0.16 | 1.3E-01 |

Table 4.2: XRR measurements of thickness, superficial roughness, and density for $AlN_xO_y$:H layers and interfacial roughness for $AlN_xO_y$:H/*c*-Si interfaces.

### 4.2.4 Photoluminescence (PL) measurements

Photoluminescence measurements of AlN$_x$O$_y$:H/*c*-Si(p) were recorded at room temperature in a back reflection geometry using an inVia- Renishaw micro-Raman spectrometer. The films were excited with a wavelength of 325 nm (3.81 eV) from a He Cd laser with an average power density of approximately 1.5 W/m. The recorded spectra cover the visible range from 400 nm to 700 nm. A 40× objective lens was used to focus the laser on the surface of the thin films studied.

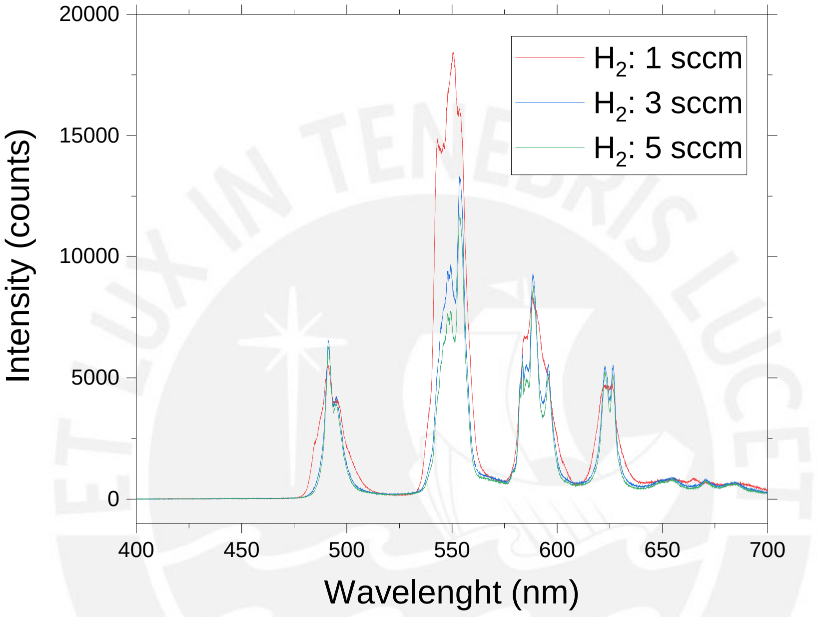

Figure 4.6: Photoluminescence (PL) measurements of the AlN$_x$O$_y$:H layers

Figure 4.6 shows the photoluminescence of the three hydrogenated samples. The photoluminescence intensity decays when the hydrogen flow at deposition increases. This effect is probably due to the reduction of defects at the AlN$_x$O$_y$:H layer by hydrogen passivation. The energy-transfer mechanism most probably used by the terbium ions is the energy transfer by defects. The photoluminescence is reduced at fewer defect concentrations (more H$_2$ flow at deposition), as shown in Figure 4.6. Similar studies are found in [34, 76, 77].

### 4.2.5 Modulated surface photovoltage

Chemical passivation of silicon surfaces by hydrogenated thin-film layers is well studied [69, 70]. For example, hydrogenated aluminum nitride (AlN:H) thin layers are suitable for the passivation of crystalline silicon [17, 18]. Modulated SPV can also analyze other materials and interfaces such as $ZrO_2$/GaAs, $SiO_2$/GaAs, GaP/GaAs, $MAPbI_3$ Perovskite, CdSe quantum dot films and ZnO/GaP heterojunction [80–83].

Studies revealed indirectly the improvement of the surface passivation by measuring the lifetime of the minority charge carriers in the bulk by quasi steady QSSPC [84,85] and the density of interface defect states ($D_{it}$) using the HF C-V method [86, 87].

Furthermore, it is also possible to estimate $D_{it}$ from large signal transient SPV measurements by applying external potentials [88,89]. However, numerous samples, such as the sample investigated in this work, cannot be studied by QSSPC and C-V, for example, due to short lifetimes caused by high bulk or interface recombination rates or due to leakage currents [45, 90], respectively. In contrast, modulated SPS measurements allow a very sensitive study of defect states below the bandgap of a semiconductor [91].

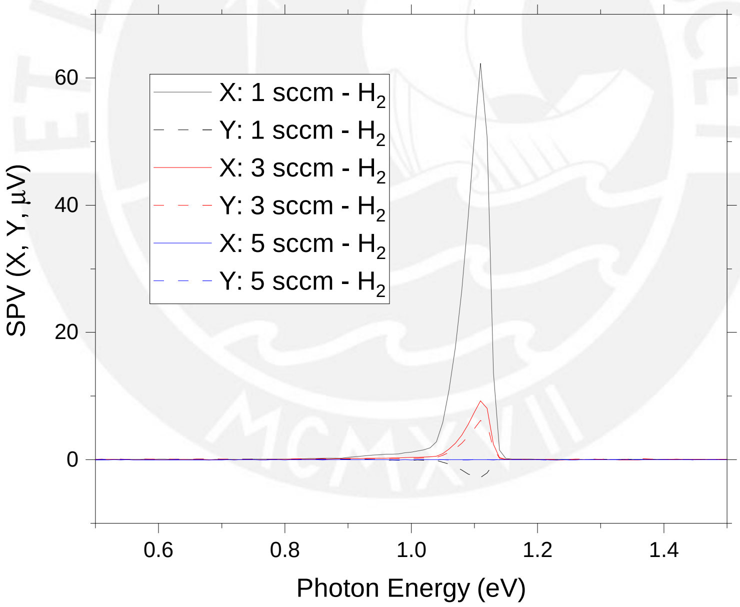

Figure 4.7: In phase (X) and 90 °C phase shifted (Y) signal from modulated SPV $AlN_xO_y$:H at 1 sccm, 3 sccm, 5 sccm of hydrogen flow at deposition (cut-off filter 1100 nm, chopper frequency: 1033 Hz, monochromator aperture: 2 mm)

Figure 4.7 shows the in phase signal (X) with 60 µV, 10 µV and about 0 V for the 1 sccm, 3 sccm and 5 sccm of hydrogen flow at deposition. This technique does not have enough sensitivity to observe the 5 sccm sample while the transient SPV can be observed clearly for the mentioned sample.

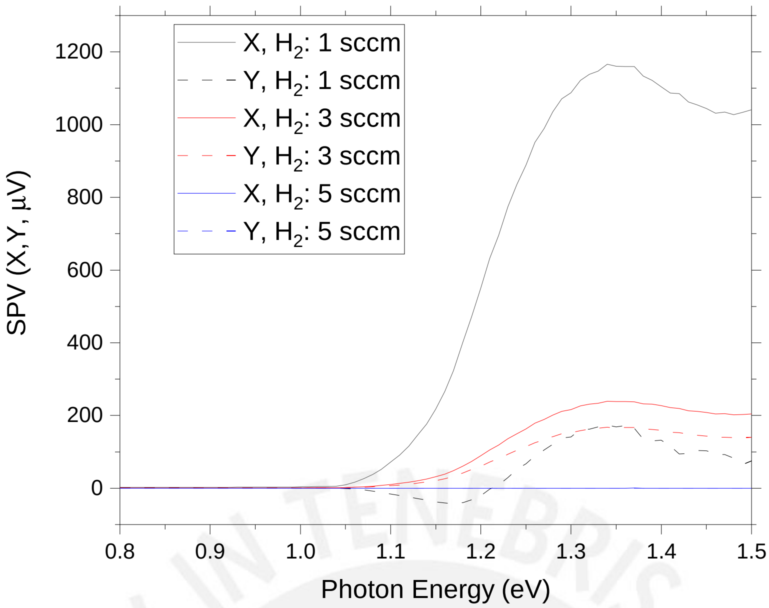

Figure 4.8: In phase (X) and 90 °C phase shifted (Y) signal from modulated SPV $AlN_xO_y$:H at 1 sccm, 3 sccm, 5 sccm of hydrogen flow at deposition (without filter 1100 nm, chopper frequency: 1033 Hz, monochromator aperture: 2 mm)

In Figure 4.8, the in-phase signal (X) and the 90 degree-shifted signal (Y) were plotted for the three $AlN_xO_y$:H/*c*-Si samples. The X signal is the fast SPV response with respect to the chopper frequency, while the Y signal is the slow response with respect to the chopper frequency. It is possible to say for the 5 sccm sample that the is a change in the direction of the charge carrier relaxation (change in sign). These results will be noticed in detail using the transient SPV spectroscopy.

Modulated SPV measurements are performed to give a first observation of the electronic properties of the $AlN_xO_y$:H/*c*-Si interfaces and the impact of hydrogen in such interfaces. In order to avoid the effect of the stray light at the monochromator, an 1100 nm (1.13 eV) cut-off filter is used, as explained in Chapter 3.

From Figure 4.9, with the cut-off filter, signals in the sub-bandgap region (energies below $E_g$) are detected for the 1 sccm and 3 sccm of hydrogen flow at deposition samples. The modulated SPV signal for the 5 sccm sample is negligible to be analyzed. The amplitude of the SPV signals decreases with an increase in hydrogen flow during deposition. From the shapes of the 1 sccm and the 3 sccm is possible to recognize SPV signals from defects: deep states and tails states.

The SPV responses in Figure 4.9 indicated that a higher hydrogen content in the sample leads to a reduced SPV signal. These changes in response could be attributed to the interface defect passivation by the hydrogen. At higher hydrogen contents, more defects near or at the interface are passivated, thus, reducing their charge and band bending in the *c*-Si. This may be translated into a reduced SPV signal.

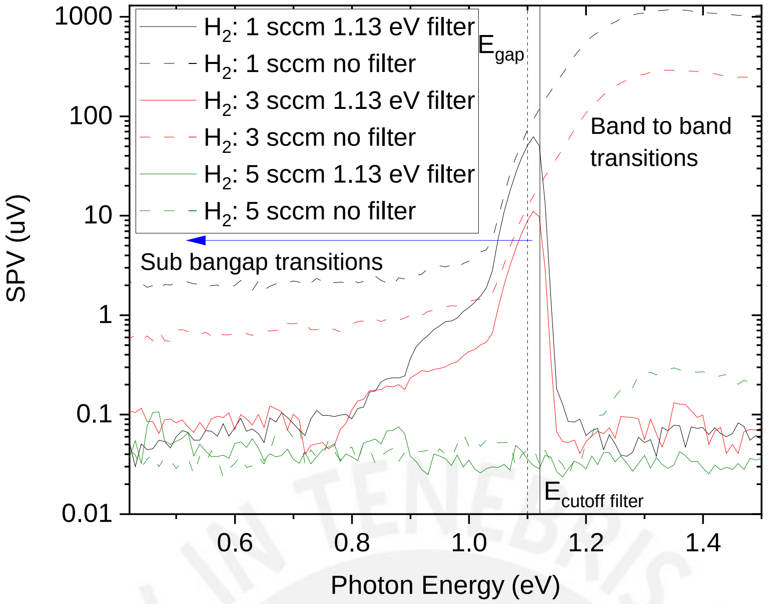

Figure 4.9: Modulated SPV spectroscopy for the AlN$_x$O$_y$:H/*c*-Si(p) samples with 1 sccm, 3 sccm, 5 sccm of hydrogen flow at deposition.

To discuss this hypothesis, in Figure 4.10(a), we assign the SPV signals at different photon energies for the 1 sccm and 3 sccm samples (with filter) to possible electronic transitions, as depicted in Figure 4.10(b). For this interface (Tb doped AlN$_x$O$_y$:H/*c*-Si), we propose three possible transitions: A) band-to-band transitions from valence ($E_V$) to conduction band ($E_C$) for $E_{h\nu} \geq E_{gap}$; B) from tail states or acceptor states ($E_a$) to conduction band for $E_{h\nu}$ below but close to $E_{gap}$. An exponential function in Figure 4.10(a) estimates an onset of the fundamental absorption ($E_{on}$) around 1.02 eV [43]; and C) sub-bandgap transitions from interface defect states, represented by Gaussian functions in Figure 4.10(a), to conduction band when $E_{h\nu}$ is smaller than $E_{gap}$. In the latter case, we postulate that after the transition from an interface defect state to the conduction band (C), the promoted electron is repelled by the negative charge in the dielectric (Tb doped AlN$_x$O$_y$:H) as depicted in Figure 4.10(b). The resulting separation of charges induces a change in the band bending, giving rise to the SPV signal [51]. The amount of these transitions depends on the number of defects: a higher defect density results in a higher SPV signal. Hence, we can conclude that the sample deposited at 1 sccm of hydrogen flow has more defect states near or at the interface and, thus, a higher SPV signal. Whereas the 3 sccm sample has a lower defect state density and, thus, a lower SPV signal. In the case of the 5 sccm sample, the defect state density is below the sensitivity of the modulated SPS technique. Therefore, in Figure 4.10 only the signal from band-to-band transitions (A) can be observed without the filter.

The SPV signal is positive for all cases, indicating that the silicon surface is in accumulation, given that it is p-type doped silicon. Under these conditions, the Tb doped

$AlN_xO_y$:H layer presents a negative fixed charge.

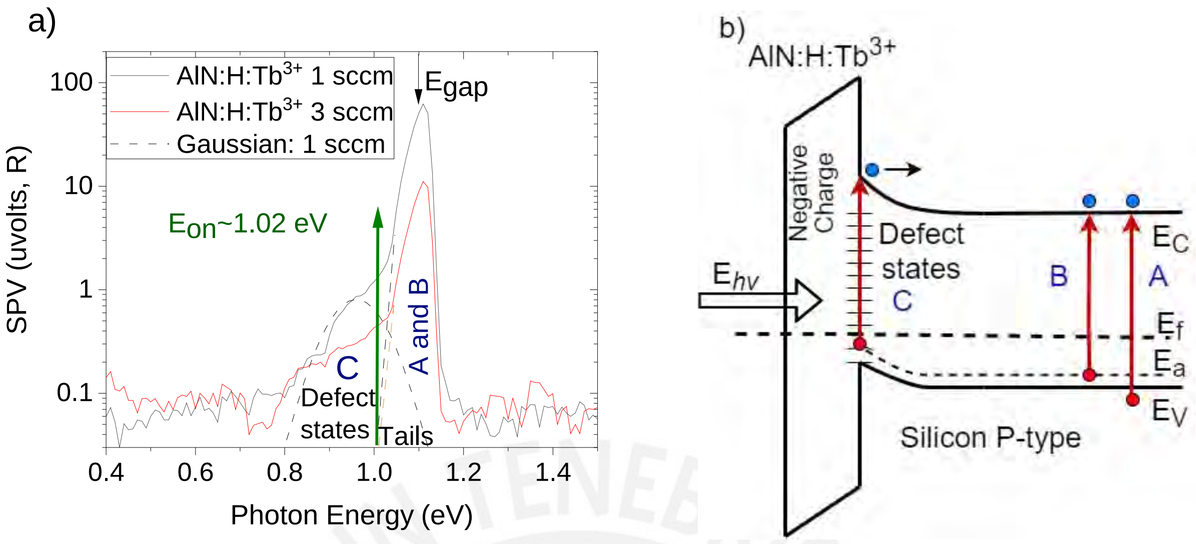

Figure 4.10: Fitting of deep defects (gaussian curves) and tail states (exponential curves) from modulated SPV spectroscopy for the $AlN_xO_y$:H/*c*-Si(p) samples with 1 sccm, 3 sccm, 5 sccm of hydrogen flow at deposition.

Figure 4.10(a) shows the fitting with gaussian curves for deep defects and with exponential curves for tail states. In the case of deep defects, the 1 sccm sample has a higher SPV signal than the 3 sccm sample. However, the range of photon energies in the 3 sccm sample is wider than the 1 sccm sample. The tail states may indicate the presence of a disordered layer close to the $AlN_xO_y$:H/*c*-Si(p) interfaces. The onset energy ($E_{on}$) is approximated to 1.02 eV from the exponential fittings of both samples.

The modulated SPV measurements indicate the presence of a negative fixed charge, deep states, and tail states (disorder layer) close to the $AlN_xO_y$:H/*c*-Si(p) interfaces for the 1 sccm and 3 sccm samples. For the given conditions of the modulated SPV measurements, the 5 sccm sample, the sub-bandgap SPV signal is not accessible. In order to obtain more details about the dynamics of the SPV signals (electron/hole trapping, electron/hole de-trapping, charge transfer), the nature of deep states and tail states (disorder layer), transient SPV measurements are performed. An important observation for the Tb-doped $AlN_xO_y$:H sample with 5 sccm of hydrogen flow is that the SPV is negligible due to the fast recombination due to the presence of deep defects at the interface.

## 4.3 Interface analysis of Terbium doped $AlN_xO_y$:H by Transient Surface Photovoltage (SPV) spectroscopy

Transient surface photovoltage (transient SPV) is a spectroscopic technique that can provide information about the electronic interface properties of distinct materials [51, 52]. The inability of other methods, such as HF-CV and QSSPC techniques, to provide conclusive information on these samples makes transient SPV an alternative technique for analyzing the electronic properties of the terbium-doped $AlN_xO_y$:H/*c*-Si(p) interfaces. Current leakages and high recombination rates quench the ability to obtain reliable C-V curves and bulk lifetimes (QSSPC) [45, 90]. The high sensitivity and wide time range of transient SPV, described in Chapter 2 of this work, allow this method to obtain electronic information about the terbium-doped $AlN_xO_y$:H/c-Si(p) interface, even with the constraints mentioned above. This subchapter will discuss the results obtained by transient SPV in more detail.

### 4.3.1 Ternary measurements: SPV signal, photon energy, and relaxation time

Transient surface photovoltage measurements were performed on bare *c*-Si(p) wafers and terbium doped $AlN_xO_y$:H/*c*-Si(p) samples with hydrogen flows of 1 sccm, 3 sccm, and 5 sccm at deposition (see the experimental details in Chapter 3). These measurements obtain the entire register of the SPV signals (mV) under different values of photon energy (eV) and time (second). The data acquired via transient SPV spectroscopy can be fully visualized using three variable plots (contour plots).

Figure 4.11 shows the ternary (contour) plots of the transient SPV measurements of the bare c-Si and the terbium doped $AlN_xO_y$:H/*c*-Si(p) samples with 1 sccm, 3 sccm, and 5 sccm: The variables are photon energy (in eV at *x*-axis), time (in seconds at *y*-axis, logarithmic scale) and, a color-graded SPV signal (in mV and logarithmic scale). From the ternary measurement information, it is possible to obtain different plots by selecting specific photon energies or specific relaxation times. These *cuts* allowed further analysis of the buried terbium-doped $AlN_xO_y$:H/*c*-Si(p) interfaces.

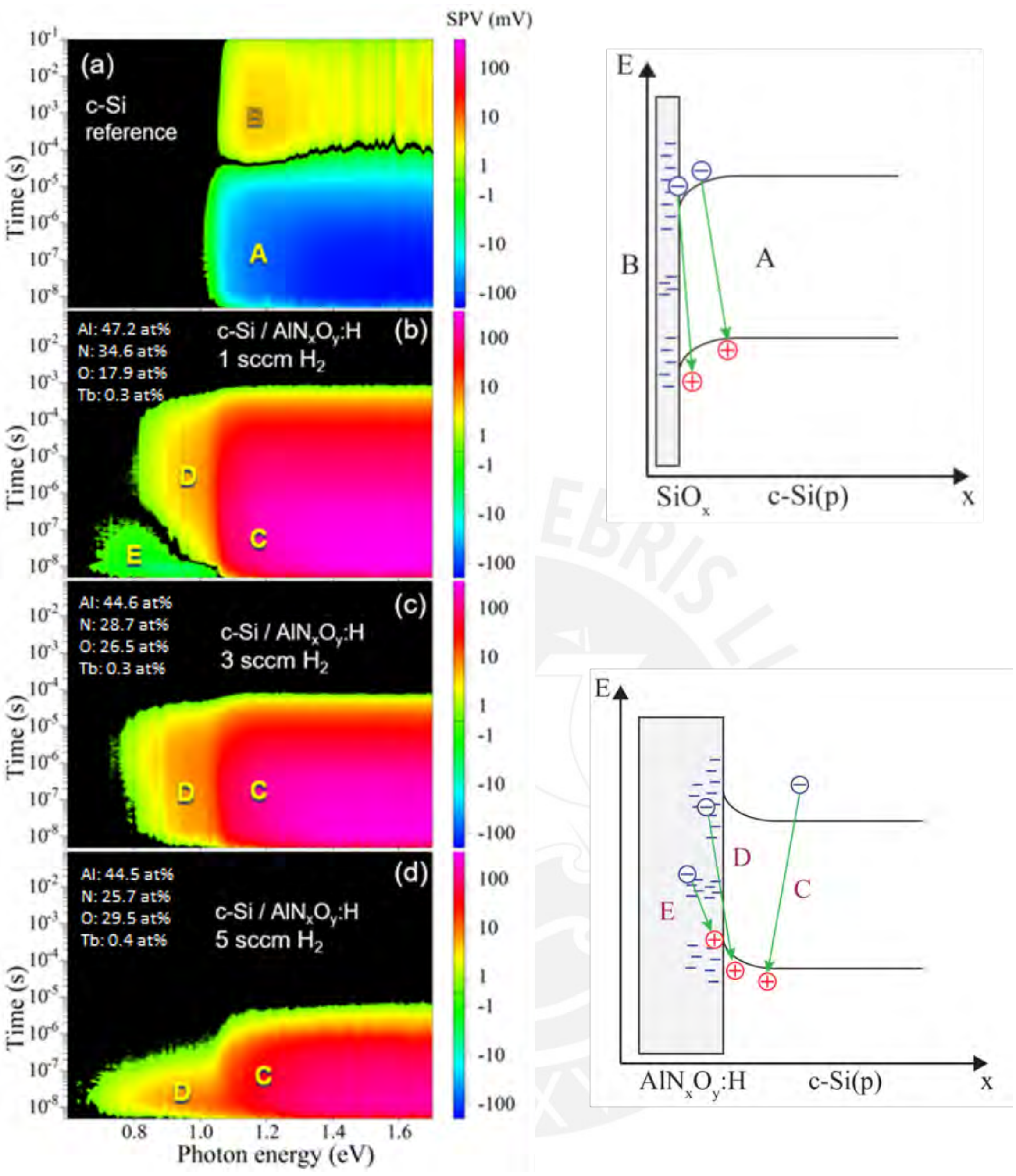

Figure 4.11: Contour plots of the transient SPV spectroscopy for the bare *c*-Si sample (a) and for the AlN$_x$O$_y$:H/*c*-Si samples deposited with 1, 3 and 5 sccm H$_2$ flow ((b), (c) and (d), respectively). Numbers in (b-d) give the relative amounts of Al, N, O and Tb obtained by EDX. The SPV signals were discriminated at 0.15 mV. A-E denote charge separation dominated by the surface space charge region of depleted p-type *c*-Si (A), by electron trapping at surface states (B), by an accumulation layer at the surface (C), by electron trapping at deep surface states (D), by hole trapping at deep surface states (E). Adapted from Dulanto et al, 2022 [74].

Figure 4.11(a) plots the transient SPV measurement for the reference sample (*c*-Si(p)). The SPV signal started from photon energies around 1 eV, just below the bandgap energy of c-Si. This signal under the bandgap energy gave evidence of defect states close to the bandgap. SPV signals started at negative values up to about 30 µs and reached a maximum of more than - 0.15 V. This behavior was from a depleted p-type doped semiconductor dominated by charge separation processes in the surface space charge region (denoted by A). After 30 µs, the SPV signals change to positive values (denoted by B), indicating the slow emission of trapped electrons at the native oxide. These states were close to the *c*-Si(p) surface. The evolution of weak positive SPV signals at long times gave evidence for hole trapping at the surface, which can be caused, for example, by hole transfer to water species at/near the surface oxide [92, 93].

Figure 4.11(b-d) shows the SPV signal from the $\mathrm{AlN}_x\mathrm{O}_y$:H/*c*-Si(p) samples. The $H_2$ flows at the deposition were 1, 3, and 5 sccm (b-d, respectively). In contrast to the reference sample, these samples exhibited positive SPV signal (denoted by C) for photon energies above 1.1 eV giving evidence of a change of the direction of the built-in-electric field near the surface, i.e., to the formation of an accumulation layer. This sign change was due to a fixed negative charge formed in the $\mathrm{AlN}_x\mathrm{O}_y$:H layer. These positive signals were relaxed in hundreds of $\mu$s, tens of $\mu$s, and $\mu$s for 1, 3, and 5 sccm, respectively.

The legends in Figure 4.11(b-d) give the relative element contents of aluminum (Al), oxygen (O), nitrogen (N), and terbium (Tb) in the $\mathrm{AlN}_x\mathrm{O}_y$:H layer. The nitrogen content decreased from 34.6 to 25.7 at %, and the oxygen content increases from 17.9 to 29.5 at % when the hydrogen flow rate at deposition increases. On the other hand, aluminum slightly changed from 47.2 to 44.5 at %, increasing the hydrogen flow rate at the deposition. These different relative contents could result in various stoichiometries with a different distribution of defects at/near the surface of *c*-Si. This defects distribution was responsible for the formation of the fixed negative charge. Silicon nitride ($\mathrm{SiN}_x$), silicon dioxide ($\mathrm{SiO}_2$), and aluminum oxide ($\mathrm{Al}_2\mathrm{O}_3$) are well-studied passivation materials that served as a reference of the possible defects distribution presented at the $\mathrm{AlN}_x\mathrm{O}_y$:H due to their element composition [94–97].

The content of elements was measured in atomic % and the content of hydrogen is not considered. A calculation of the hydrogen bonds by FTIR measurements was done in order to prove the presence of hydrogen and its growth while the hydrogen flow at the deposition is incremented.

These transient SPV measurements (visualized as ternary variable plots) contained important information about the electronic features of the samples. In order to analyze the ternary variable measurement information, *cuts* in time and photon energy of these plots are used to divide and organize the observations.

In order to understand the ternary variable measurements, the following band diagrams explain, in a first simplified form, the SPV results at the 1 sccm, 3 sccm, and 5 sccm of hydrogen flow at the $\mathrm{AlN}_x\mathrm{O}_y$:H/*c*-Si(p) interface. Figure 4.12 shows the band diagram in the dark, the optical transitions, and the charge carrier separation at the $\mathrm{AlN}_x\mathrm{O}_y$:H/*c*-Si(p). These band diagrams do not consider the acceptor passivation on the

Si bulk (developed later in this subchapter).

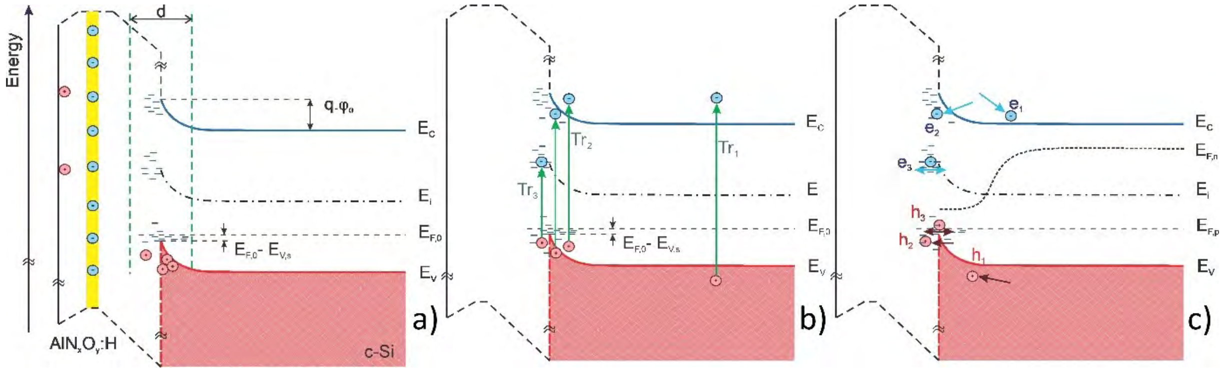

Figure 4.12: Examples for suitable a) charge distribution across a sample in the dark, b) possible transitions and, c) charge carrier separation

Figure 4.12(a) depicts the charge distribution in the dark. Due to the negative fixed charge presented at the AlN$_x$O$_y$:H layer, the band bending at the semiconductor is upwards at the accumulation regime.

Figure 4.12(b) depicts the possible optical transitions in the AlN$_x$O$_y$:H/*c*-Si samples: Band-to-band transitions that require energies higher or equal to the bandgap energy (Tr$_1$). Defect to conduction band transition and valence band to defect transition (Tr$_2$). These transitions could be excited by photon energies lower than the bandgap energy. Finally, defect-to-defect transition (Tr$_3$) could be excited by photon energies lower than the bandgap energy.

Figure 4.12(c) depicts the charge separation mechanisms after illumination. The first mechanism is when the electron/hole moves inside the conduction/valance band (e$_1$, h$_1$, respectively). The second mechanism is when the electron/hole moves from the conduction/valance band to the defect state at/near the interface (e$_2$, h$_2$, respectively). Finally, the third mechanism is when the electron/hole moves from one defect to another via tunneling (e$_3$, h$_3$, respectively). This last diagram is crucial to understanding the SPV time variations due to their different relaxation mechanisms.

### 4.3.2 Relaxation of SPV signals at different photon energies

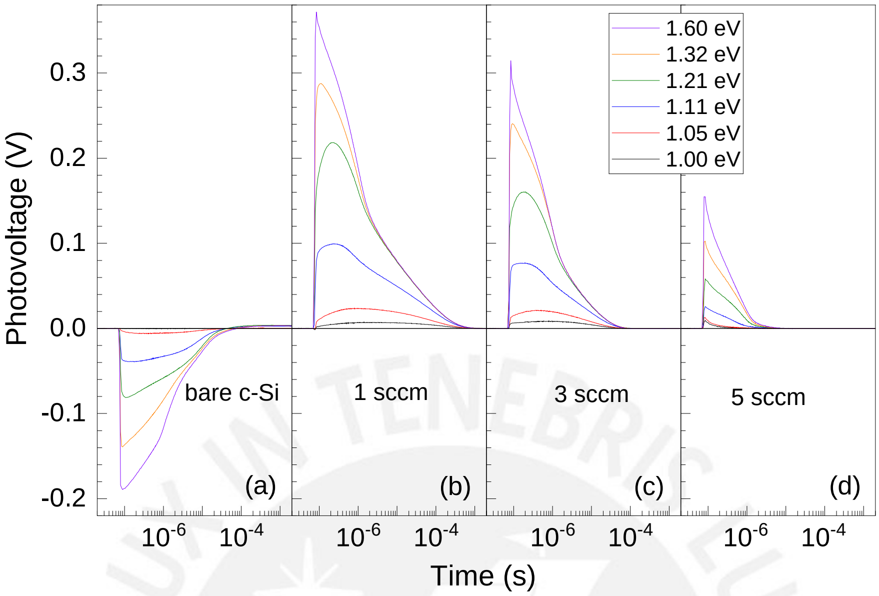

Figure 4.13: SPV transients at photon energies of 1.60, 1.32, 1.21, 1.11, 1.05 and 1.00 eV (black, red, green, blue, orange and dark yellow lines, respectively) for the reference *c*-Si (a), and the 1 sccm (b), 3 sccm (c), and 5 sccm (d) of $H_2$ flow at deposition of $AlN_xO_y$:H/*c*-Si(p) samples

Figure 4.13 is obtained by “cuts” at six different photon energies (1.60, 1.32, 1.21, 1.11 1.05 and 1.00 eV) of the ternary plots previously shown. The maximum SPV signals are -190 mV, 370 mV, 310 mV, and 155 mV for the reference, 1 sccm, 3 sccm, and 5 sccm of $H_2$ flow at deposition $AlN_xO_y$:H/*c*-Si(p) samples, respectively. The relaxation times among the samples, decays in around one order of magnitude from the 1 sccm to the 3 sccm of $H_2$ flow sample. From the 3 sccm to the 5 sccm of $H_2$ flow sample, the relaxation time decays around another order of magnitude.

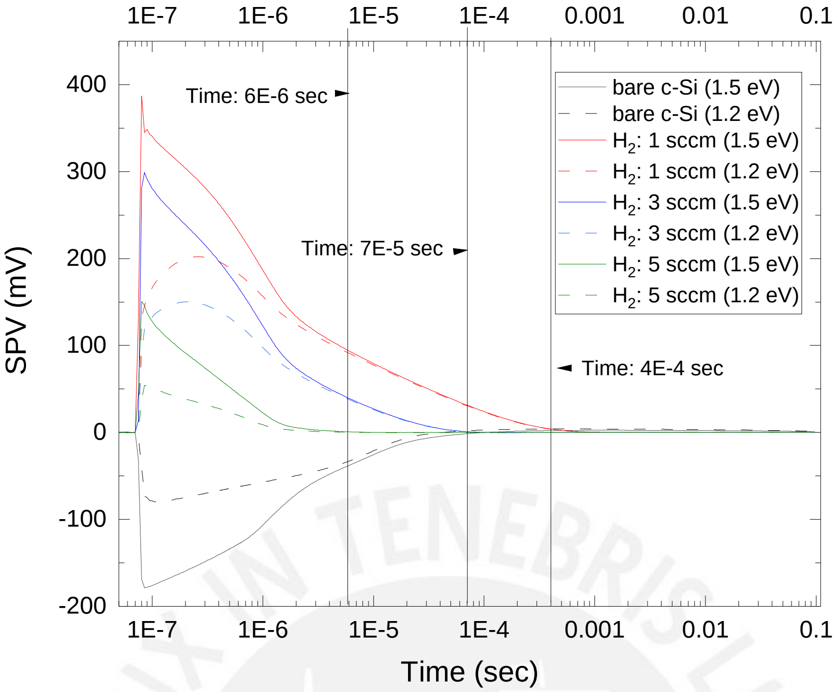

Figure 4.14: SPV transients excited at two photon energies higher than $E_g$ (1.5 and 1.2 eV; solid and dashed lines, respectively) for the reference sample and for the samples deposited at 1, 3 and 5 sccm of $H_2$ flow (black, red, blue and green lines, respectively).

Figure 4.14 compares the SPV signal relaxations of the four samples at 1.5 and 1.2 eV. The relaxation times are about 70 µs, 400 µs, 70 µs and 6 µs for the reference, 1 sccm, 3 sccm, and 5 sccm of $H_2$ flow at deposition $AlN_xO_y$:H/*c*-Si(p) samples, respectively. The shape of the 1.5 eV photon energy curve reaches the maximum SPV signal value at the beginning of the excitation while at the 1.2 eV of photon energy, the 1 sccm and the 3 sccm samples reach their maxima hundreds of nanoseconds after. This effect is possible due to an artifact of the double-side coated *c*-Si(p) by the $AlN_xO_y$:H layer.

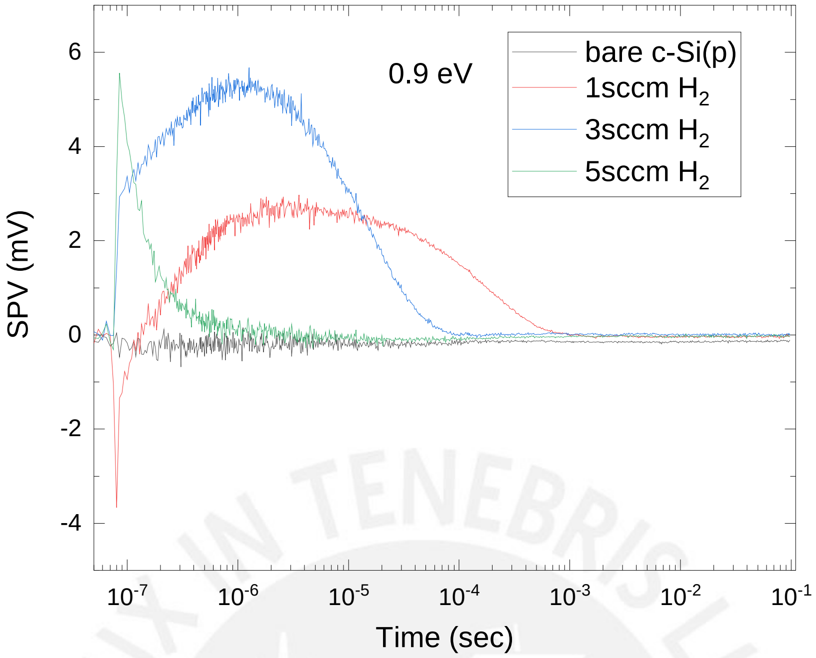

Figure 4.15: SPV transients excited at sub bandgap (0.9 eV) for the bare *c*-Si and $AlN_xO_y$:H/*c*-Si(p) samples deposited at 1, 3 and 5 sccm of $H_2$ flow (black, red and blue lines, respectively).

Figure 4.15 shows the SPV signal at the sub-bandgap (photon energies below $E_g$) region of 0.9 eV excitation. SPV signals at the sub-bandgap regime exhibited transitions from/towards defect states at energies within the bandgap. The 1 sccm of $H_2$ flow at deposition sample started a negative SPV signal and passed to positive before equilibrium. The 5 sccm of $H_2$ flow at deposition sample exhibited a faster decay regarding the other samples.

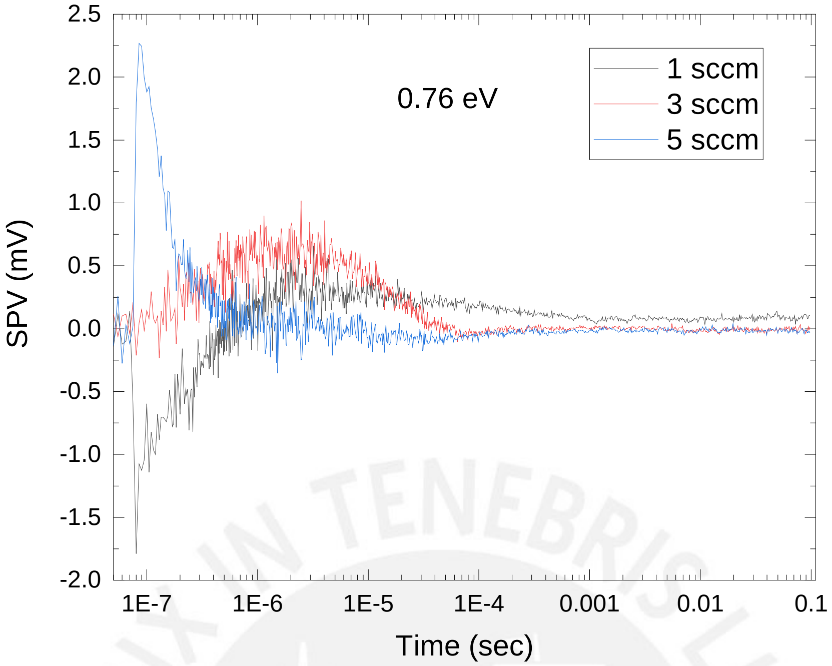

Figure 4.16: SPV transients excited at sub bandgap (0.76 eV) for the AlN$_x$O$_y$:H/*c*-Si(p) samples deposited at 1, 3 and 5 sccm of H$_2$ flow (black, red and blue lines, respectively).

Figures 4.16 shows the SPV responses of the AlN$_x$O$_y$:H/*c*-Si(p) samples at sub-bandgap 0.76 eV excitation. SPV signals for the 1 sccm and the 3 sccm of hydrogen flow at deposition samples were reduced significantly after the laser pulse. The 5 sccm of hydrogen flow AlN$_x$O$_y$:H/*c*-Si(p) sample did not considerably reduce the SPV signal after the laser pulse, and its decay is the fastest of the three samples, probably due to another transport mechanism (hopping between defects).

### 4.3.3 Passivation of p-doped silicon atoms by hydrogen at *c*-Si(p)

The maximum values of the SPV signals are given in Figure 4.17 (a) for the bare *c*-Si(p) sample and the samples with $AlN_xO_y$:H layers. At 0.9 eV, the SPV signal was approximately -3.6 mV for $H_2$ flow of 1 sccm sample. Under this condition, electrons excited from defect states were located slightly in front of the *c*-Si surface and preferentially separated towards the surface of *c*-Si. For comparison, the maximum SPV signal at 0.9 eV was only about -0.2 mV for the reference (bare *c*-Si(p)) sample. In contrast, the maximum SPV signals at 0.9 eV were positive and amounted to 3.0 and 6.7 mV for $H_2$ flow of 3 and 5 sccm, respectively. This condition suggests that electrons excited from defect states near the *c*-Si surface were preferentially separated towards the $AlN_xO_y$:H layers for those samples. Furthermore, the separation of electrons excited from defect states near the *c*-Si surface was remarkably stronger for $H_2$ flow of 5 sccm than 3 sccm.

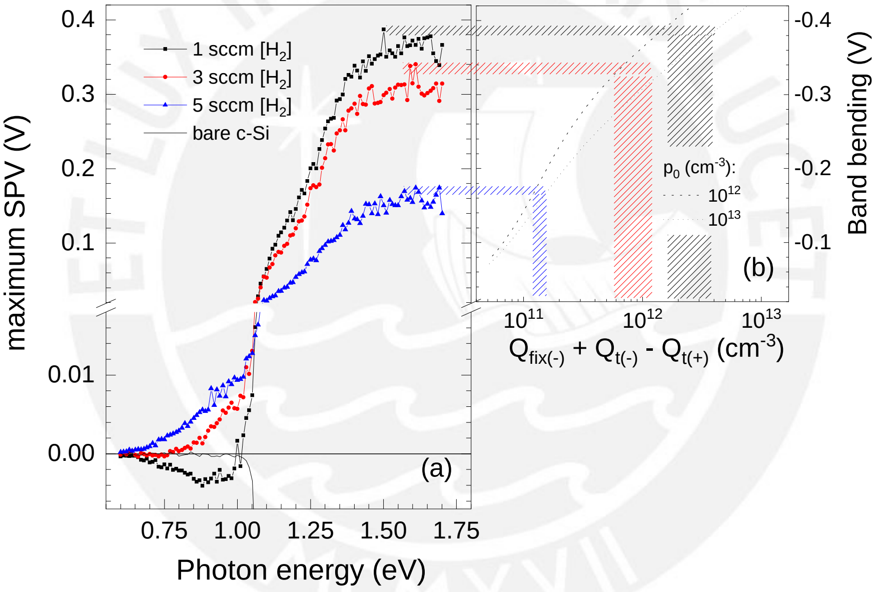

Figure 4.17: Dependence of the maximum SPV signals on photon energy for the $AlN_xO_y$:H layers deposited at $H_2$ flow of 1, 3 and 5 sccm and the reference sample (black squares, red circles, blue triangles, and thin solid line, respectively; (a)) and calculated band bending at an ideal silicon surface under accumulation as a function of the net negative charge for hole densities of $10^{12}$ and $10^{13}$ $cm^{-3}$ (dashed and dotted lines, respectively; (b)) [74]

The maximum SPV signals are saturated at higher photon energies for excitation with photon energies above the band gap. They reached the highest values ($SPV_{max}$) of 387, 341, and 175 mV for $H_2$ flow of 1, 3, and 5 sccm, respectively. The extensive positive SPV signals are related to strong band bending caused by an accumulation layer near the surface.

For p-type doped $c$-Si with a resistivity of 1 – 3 ohm/cm, which corresponds to (an original) density of holes of 1.5 - 0.5 × $10^{16}\,\mathrm{cm}^{-3}$, the difference between the Fermi-energy in equilibrium ($E_{F0}$) and the valence band edge in bulk ($E_{V,b}$) is about 180 meV. SPV signals of semiconductors are defined as the difference between band bending under illumination and band bending in the dark [52, 98]. Under strong illumination, the bands are practically flat. Therefore, $(E_{F0} - E_{V,b})/q$ with $q$ denoting the elementary charge gives an upper limit for SPV signals of a semiconductor under accumulation, i.e., maximum SPV signals up to about 180 mV would be expected for samples with the original density of holes. However, the SPVmax of the sample with the $\mathrm{AlN}_x\mathrm{O}_y$:H layer deposited at an $\mathrm{H}_2$ flow of 1 sccm was larger than 180 mV by more than 200 mV. Therefore, $(E_{F0} - E_{V,b})/q$ of the sample with the $\mathrm{AlN}_x\mathrm{O}_y$:H layer deposited at $\mathrm{H}_2$ flow of 1 sccm was much larger than $(E_{F0} - E_{V,b})/q$ for the original doping. This result indicates that most acceptors have been passivated during the deposition and post-treatment of the $\mathrm{AlN}_x\mathrm{O}_y$:H layer. As mentioned before, the passivation of acceptors in silicon by atomic hydrogen is well known [36]. As a result, the short post-annealing up to 850 °C in the air did not result in significant de-passivation, i.e., sufficient dissociation of B-H pairs with simultaneous out-diffusion of hydrogen. This minor de-passivation is probably due to the presence of water molecules during the post-annealing process and $\mathrm{AlN}_x\mathrm{O}_y$:H acting as diffusion barriers. Additionally, sputtered aluminum oxide films post-annealed were found to contain high hydrogen concentrations exceeding $10^{21}\,\mathrm{cm}^{-3}$ [99].

Based on the difference between the highest maximum SPV signals and $(E_{F0} - E_{V,b})/q$, it was possible to estimate the order of magnitude of the density of holes after layer deposition at 1 sccm of $\mathrm{H}_2$. A difference of about 200 mV indicates that the density of holes ($\mathrm{p}_0$) after layer deposition was approximately $10^{12}$ – $10^{13}\,\mathrm{cm}^{-3}$. In addition, there is no reason to assume that the hydrogen flow during the deposition of the $\mathrm{AlN}_x\mathrm{O}_y$:H layers would cause a lower degree of acceptor passivation. For samples with $\mathrm{AlN}_x\mathrm{O}_y$:H layers deposited at $\mathrm{H}_2$ flow of 3 and 5 sccm, the reduced maximum SPV signals were due to a reduction in (net) negative charge.

By assuming an ideal metal-insulator-semiconductor capacitor, it is possible to estimate the densities of (net) negative charge fixed in the $\mathrm{AlN}_x\mathrm{O}_y$:H layer ($Q_{fix(-)}$). For $\mathrm{p}_0$ values of $10^{12}$ and $10^{13}\,\mathrm{cm}^{-3}$, Figure 4.17 (b) shows the dependence of band bending on $Q_{fix(-)}$.

At $\mathrm{H}_2$ flow of 1 sccm, $\mathrm{AlN}_x\mathrm{O}_y$:H layers exhibit $Q_{fix(-)}$ ranging from 1.5 to 4 × $10^{12}\,\mathrm{cm}^{-3}$. In comparison, after short annealing [17] with peak temperatures of 820 °C, $Q_{fix(-)}$ was about 1 - $10^{12}\,\mathrm{cm}^{-3}$ in AlN:H layers [2]. For the $\mathrm{AlN}_x\mathrm{O}_y$:H layers deposited at $\mathrm{H}_2$ flows of 3 and 5 sccm, $Q_{fix(-)}$ was reduced to about 0.5 - 2 × $10^{12}\,\mathrm{cm}^{-3}$ and 1 - 2 × $10^{11}\,\mathrm{cm}^{-3}$, respectively.

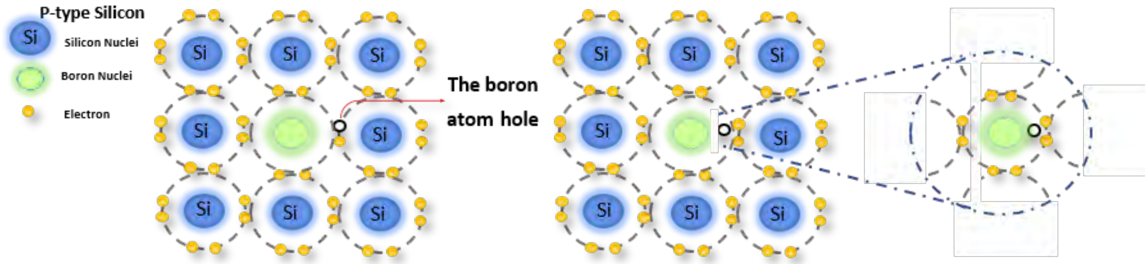

Figure 4.18: Schematic of acceptor's passivation by hydrogen.

The diagram depicted in Figure 4.18 explains the acceptors' passivation by hydrogen. Hydrogen passivates silicon atoms connected to boron atoms and reduces the effective number of acceptor atoms that dope *c*-Si(p) bulk. This effect reduces the density of holes, and the Fermi level shifts towards the mid-gap. This diagram also illustrates how the transient SPV results and the boron passivation of the *c*-Si(p) bulk can be explained coherently using a four-layer model.

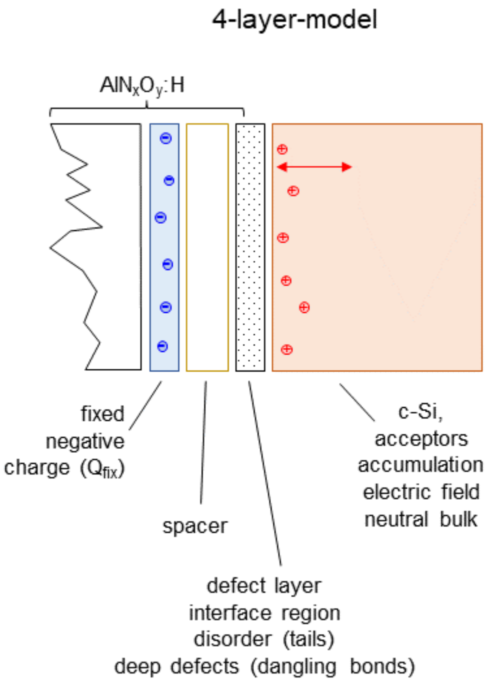

Figure 4.19: Four-layer model for AlN$_x$O$_y$:H/*c*-Si(p).

The four-layer model depicted in Figure 4.19 has the following constituents:

1. A spacer layer that is required to avoid neutralization of negative fixed charge (there would not be fixed negative charge without a spacer layer with thickness above the tunneling distance).

2. A defect layer with a high degree of disorder caused by damage in the interface region (thickness of the order of several nm).

3. A charge separation across the built-in electric field in *c*-Si for excitation with photon energies above the band gap, maximum SPV signals up to 350 mV (accumulation, partial passivation of acceptors by hydrogen)

4. A charge separation within the defect layer and in *c*-Si (in case of transfer into *c*-Si) for excitation of mobile charge carriers with photon energies below the band gap.

The hypothesis obtained for this 4-layer model is the limitation of back-transfer or recombination by trap-limited transport across the defect layer. At strong accumulation, only a weak change of band bending across the layer is possible due to the high density of states at the valence band edge; therefore, the maximum of SPV signals can only be explained by partial compensation or passivation of acceptors in *c*-Si.
$E_{V,bulk} - E_{F,bulk}$ (no treatment) $\approx 180\ldots200$ mV, $p_0 = 10^{16}\,\text{cm}^{-3}$
$E_{V,bulk} - E_{F,bulk}$ (1 sccm $H_2$) $\approx 350$ mV, $p_{com} < 10^{14}\,\text{cm}^{-3}$

### 4.3.4 Band bending estimation from a simplified Metal-Insulator-Semiconductor Capacitor Model

The implicit relationship for the metal gate voltage $V_g$ (in V), and the band bending $\psi_s$ (in V), including insulator effective charge density $Q_{(ox,eff)}$ (C cm$^2$) in a metal-insulator-semiconductor capacitor [100, 101] is:

$$V_g = \psi_s(V_g,\ldots) - \frac{(Q_sc\ (\psi_s\ (V_g,\ldots),\ N_A,\ T))}{C_{ox}} - \frac{Q_{(ox,\ eff)}}{C_{ox}} \tag{4.1}$$

Here, the general expression for the semiconductor surface space-charge-density $Q_{sc}(\psi_s, N_A, T)$, which also depends on the doping concentration $N_A$, and the device temperature T, has been taken from [101]. Additionally, $C_{ox}$ (in Fcm$^{-2}$) represent the insulator capacitance per unit area:

$$C_{ox} = \frac{\epsilon_0 \epsilon_{ox}}{d_{ox}} \tag{4.2}$$

Where $\epsilon_0$ and $\epsilon_{ox}$ are the vacuum and the insulator relative electrical permittivity, respectively, and $d_{ox}$ represents the insulator thickness.
Since we did not apply a bias voltage under the SPV measurements, we reduced Equation (4.1) in:

$$0 = \psi_s(0,\ldots) - \frac{(Q_sc\ (\psi_s(0,\ldots),\ N_A,\ T))}{C_{ox}} - \frac{Q_{(ox,\ eff)}}{C_{ox}} \tag{4.3}$$

Equation (4.3) directly relates the effective insulator fixed charge density and the band bending without considering the interfacial trapped charges (ideal interface). In this work, we considered $\epsilon_{ox} = 9.2$ for Aluminium Nitride from [102], $d_{ox}$=80 nm as a representative thickness of our samples and we assumed T=293 K (room temperature) as the SPV measurement temperature. $\psi_s$ is solved in equation (4.3) by the algorithm used in [103]. This last allows us to estimate the band bending corresponding to the maximum SPV signal from our experiments.

### 4.3.5 SPV Signals at Different Relaxation Times

Previously, plots of SPV signals versus time at fixed photon energies gave a critical observation, the passivation of acceptors by hydrogen. The following five figures show SPV signals versus photon energy at fixed times. These figures give information about the deep defects and exponential tails [51].

Figure 4.20 shows the SPV signal for the four samples at 10 ns and 1 µs after the laser pulse. The reference sample had practically no SPV signal associated with deep defect states. The $AlN_xO_y$:H/*c*-Si(p) samples had SPV signals associated with deep defect states right after the pulse excitation.

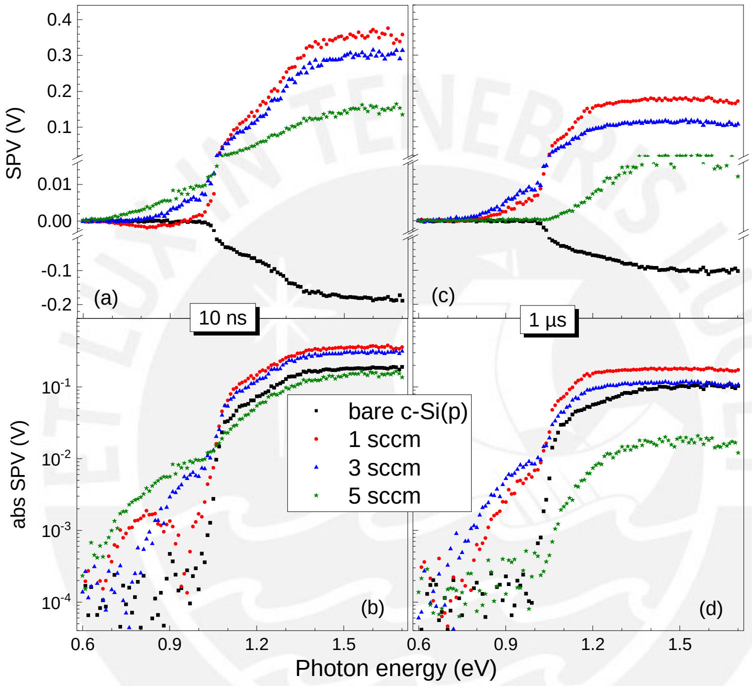

Figure 4.20: SPV signals obtained at 10 ns (a, b) and at 1 µs (c, d) on linear (a, c) and logarithmic scales (absolute values, (b, d)) for the reference samples and for the samples deposited at 1, 3 and 5 sccm of $H_2$ flow (black squares, red circles, blue triangles and green stars, respectively).

In Figure 4.20, the 1 sccm sample presents a change of sign from the overlap of two processes: negative SPV from photon energies below 0.9 eV and positive from photon energies above 0.9 eV. The 3 sccm of $H_2$ flow at the deposition sample presents positive SPV and an onset above 0.8 eV. Finally, the 5 sccm of $H_2$ flow at the deposition sample presents positive SPV and an onset below 0.7 eV with the strongest signal.

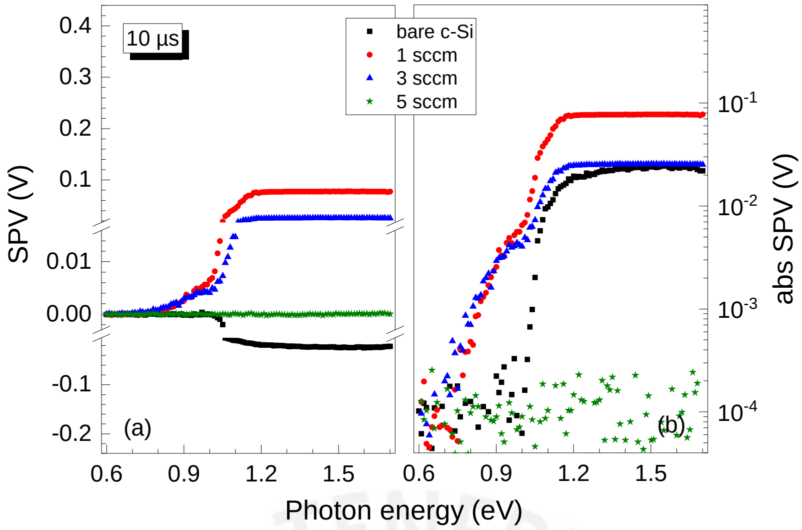

Figure 4.21: SPV signals obtained at 10 µs after pulse excitation for the four samples on linear (a) and logarithmic scales (absolute values, (b)) for the reference sample and for the samples deposited at 1, 3 and 5 sccm of $H_2$ flow (black squares, red circles, blue triangles, and green stars, respectively).

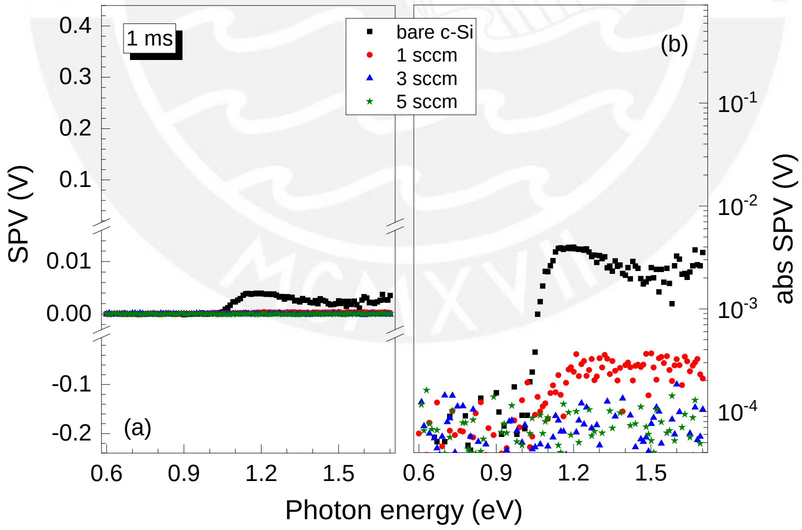

Figure 4.22: SPV signals obtained at 1 ms after pulse excitation for the four samples on linear (a) and logarithmic scales (absolute values, (b)) for the reference sample and for the samples deposited at 1, 3 and 5 sccm of $H_2$ flow (black squares, red circles, blue triangles and green stars, respectively).

Figures 4.21 and 4.22 show the relaxation in time for 10 µs and 1 ms, respectively. It was shown that the SPV signal decreased the fastest for the 5 sccm of $H_2$ flow at deposition sample (at 10 µs there was no SPV signal). The 3 sccm sample exhibits no SPV signal at 1 ms. This behavior will be explained by adding exponential and offset fittings to analyze the disorder layer and deep defects presented in the terbium doped $AlN_xO_y$:H/$c$-Si(p) interfaces.

#### 4.3.5.1 Fitting of the tail states (disorder layer) and offset (deep states)

The transient SPV measurements also allow the fitting of the tails of the samples. From these fittings, it is possible to estimate the energy of the tails. Figure [?] shows the fitting of the energy tails ($E_t$) for the reference and the sample with 1 sccm, 3 sccm, and, 5 sccm of $H_2$ flow at deposition.

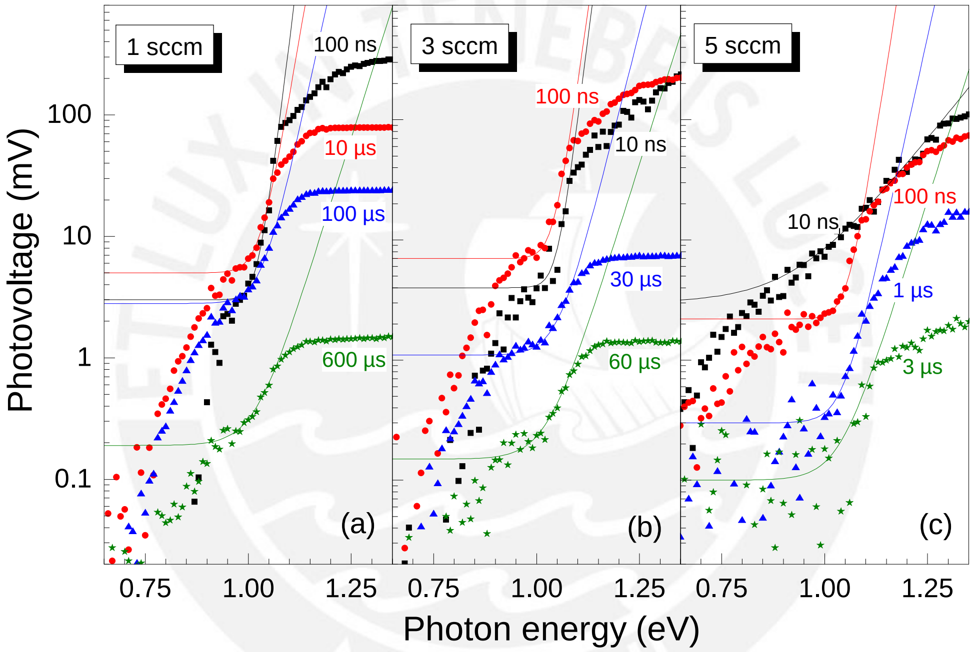

Figure 4.23: a) Typical dependencies of SPV signals obtained at relaxation times of 100 ns, 10 µs, 100 µs and, 600 µs (black squares, red circles, blue triangles and green stars, respectively) on photon energy for the Tb-doped $AlN_xO_y$:H layer deposited at $H_2$ flow of 1 sccm, b) typical dependencies of SPV signals obtained at relaxation times of 10 ns, 100 ns, 30 µs and 60 µs (black squares, red circles, blue triangles and green stars, respectively) on photon energy for the Tb-doped $AlN_xO_y$:H layer deposited at $H_2$ flow of 3 sccm and, c) typical dependencies of SPV signals obtained at relaxation times of 10 ns, 100 ns, 1 µs and 3 µs (black squares, red circles, blue triangles and green stars, respectively) on photon energy for the Tb-doped $AlN_xO_y$:H layer deposited at $H_2$ flow of 5 sccm.

Figure 4.23 (a) shows SPV spectra obtained at relaxation times ($t_{relax}$) of 100 ns, 10 µs, 100 µs, and 600 µs for the sample with the $AlN_xO_y$:H layer deposited at $H_2$ flow of

1 sccm on a logarithmic scale. The regions of the substantial increase of SPV signals near the band gap of c-Si were fitted with an exponential function combined with an offset. The characteristic energy of the exponential ($E_t$) describes the distribution energy of tail states from which mobile charge carriers were excited. In contrast, the offset corresponds to transitions from deep defect states into delocalized states. For the sample with 3 sccm of hydrogen flow at deposition (Figure 4.23 (b)), the values of $E_t$ increased with increasing time from 18 meV at 100 ns to 40 meV at 60 µs. For comparison, $E_t$ was about 12 meV (100 ns) and 15 meV (1 ms) for the reference sample at those times. Figure 4.23 (c) shows faster responses for the sample with 5 sccm. This effect is due to the increase of defects that reduces the distance between defects and a hopping transport (tunneling) appears instead of trap-limited transport.

#### 4.3.5.2 Summary of fits for tail energies ($E_t$) and the offsets (1, 3 and 5 sccm samples)

The estimation of $E_t$ and offset is calculated from exponential fits of SPV signal at different relaxation times. Figure 4.24 shows the calculation of $E_t$ from the fitted curve. Further information about the tail energies can be found in [104].

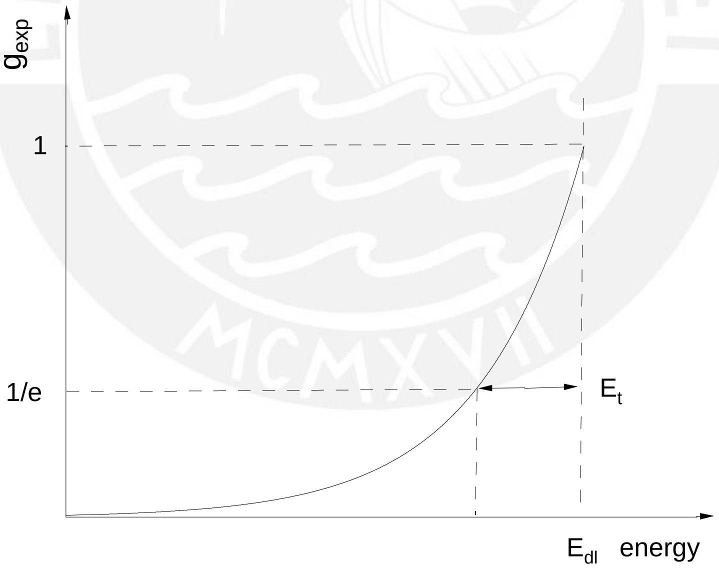

Figure 4.24: Estimation of tail energy ($E_t$) from normalized exponential fit. $E_{dl}$ indicates the energy onset of delocalized states as, for example, the band gap for fundamental absorption. $G_{exp}$ is the normalized exponential distribution.

Figure 4.25 is an example of the fitting of the SPV offset and the exponential tail energies for the Tb-AlN$_x$O$_y$:H layer deposited at $H_2$ flow of 3 sccm. The tail energies are higher at longer relaxation times.

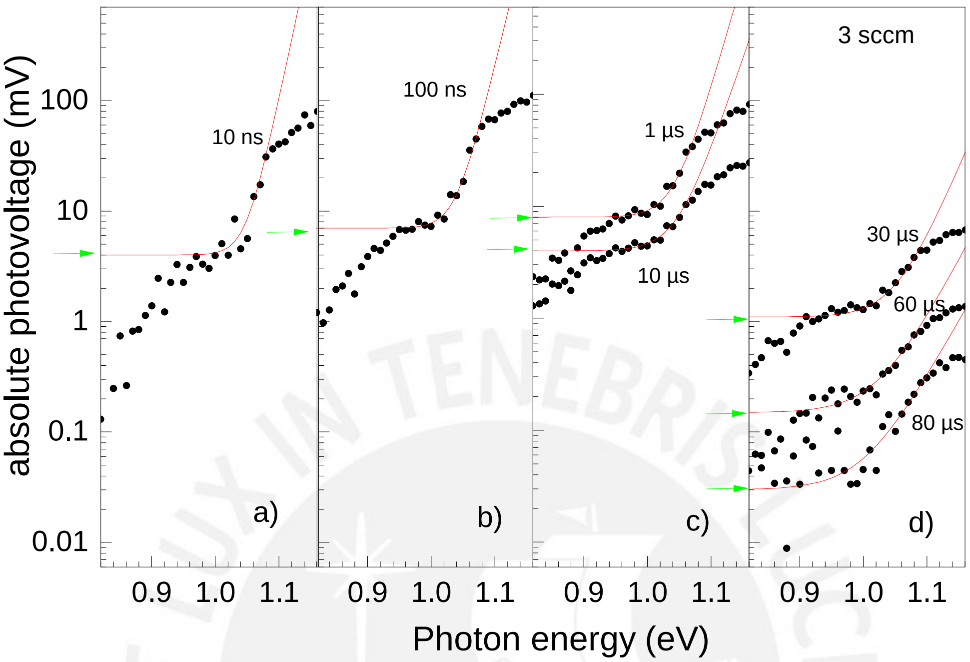

Figure 4.25: Example of offset estimation from fitting curves. SPV signals for different relaxation times (a): 10 ns, b): 100 ns, c): 1 µs and 10 µs, and, d): 30 µs, 30 µs and 80 µs) for the Tb-doped AlN$_x$O$_y$:H layer deposited at $H_2$ flow of 3 sccm. The arrows point to the estimated offsets.

Figure 4.26 shows the tendency of the energy tails ($E_t$) and offsets (deep defects related) over time. The tails and deep defects effects could be analyzed from these curves.

The dependencies of $E_t$ on $t_{relax}$ are shown in Figure 4.26 (a) for the samples with the Tb-doped AlN$_x$O$_y$:H layers. The values of $E_t$ for the sample with the AlN$_x$O$_y$:H layer deposited at $H_2$ flow of 1 sccm increased continuously with increasing relaxation from 16 meV at 10 ns over 22 meV at 100 µs to up to about 60 meV at 1 ms. In the sample with an AlN$_x$O$_y$:H layer deposited at an $H_2$ flow of 3 sccm, $E_t$ values increased with increasing relaxation time to about 45 meV at 80 µs. For the sample with the layer deposited at an $H_2$ flow of 5 sccm, $E_t$ increased strongly with increasing $t_{relax}$, reaching a value of approximately 40 meV after 3 µs. As time increased $t_{relax}$, Et decreased from more than 40 meV at 15 ns to 20 meV at 100 ns for the sample with the AlN$_x$O$_y$:H layer deposited at $H_2$ flow of 5 sccm.

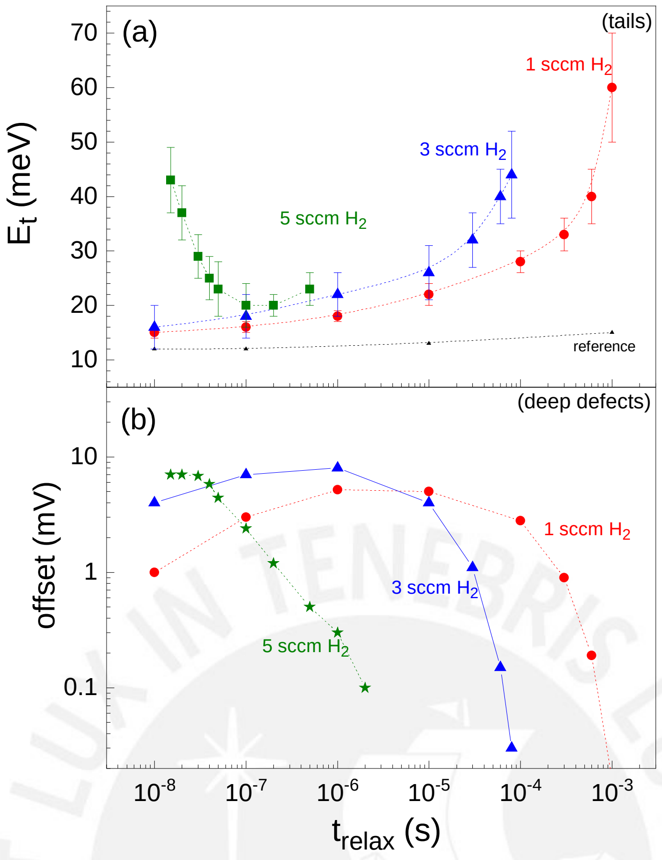

Figure 4.26: Dependencies of the energy parameter describing the exponential tails close to the bandgap (a) and of the offset of the baseline for the exponential fits (b) on the relaxation time for the Tb-doped $AlN_xO_y$:H/*c*-Si samples which were prepared at 1, 3 and 5 sccm $H_2$ flow (red circles, blue triangles, and green stars, respectively).

Figure 4.26 (b) shows the dependence of offsets normalized to SPVmax on $t_{relax}$ for samples with $AlN_xO_y$:H layers.

Another significant value that is possible to obtain from these fittings is the offset. The offset corresponds to the maximum SPV signal below the bandgap. It corresponds to the product of the charge separation length and the concentration of charge carriers separated from deep defects.

The highest values of the normalized offset were 0.014, 0.024, and 0.04 for samples with the $AlN_xO_y$:H layers deposited at $H_2$ flow 1, 3, and 5 sccm, respectively. In the case of samples with $AlN_xO_y$:H layers deposited at $H_2$ flow 1 and 3 sccm, the dependence of the normalized offset on $t_{relax}$ was fitted with exponentials, giving time constants (t) of 190 and 16 µs, respectively. In samples with the $AlN_xO_y$:H layer deposited at 5 sccm, the normalized offset could be fitted by a power law with a power coefficient of about 0.93.

The offset corresponds to the maximum SPV signal below the bandgap. It corresponds to the product of the charge separation length and the concentration of charge carriers separated from deep defects [51].

Based on this result, we can conclude that the 5 sccm sample exhibits faster relaxation due to the presence of deep defects. On the other hand, the 1 sccm exhibits slower relaxation and larger energy tails due to defect states located close to the bands or strain bonds in a defect-rich region near the surface of *c*-Si.

### 4.3.6 Superposed processes: Comparison between excitation below and above the band gap

At the sub-bandgap energies, only defect-related transitions can be measured, whereas, at the bandgap excitation, band-to-band transitions and defect-related transitions are measured simultaneously. In the case of Tb-doped $AlN_xO_y$:H with 1, 3, and 5 sccm of $H_2$ flow during deposition, the SPV signal resulting from the relaxation of charges trapped in deep defect states during excitation above the band gap energy has a slow response, whereas the relaxation of charges trapped in deep defect states occurs faster for sub-bandgap excitation.

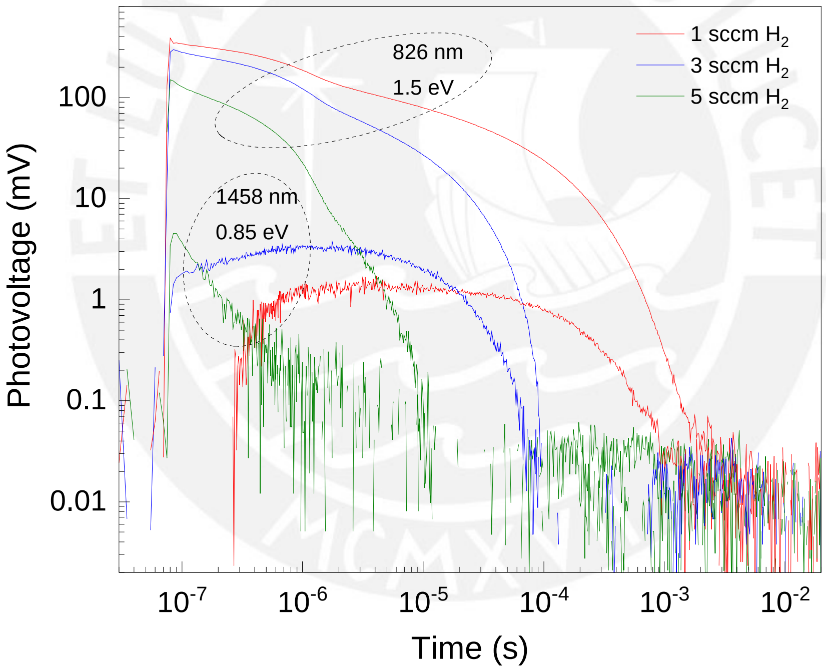

Figure 4.27: SPV transients for samples excited at 1.5 eV (826 nm, thin lines) and 0.85 eV (1458 nm, thick lines) for samples deposited at 1, 3 and 5 sccm $H_2$ flow (red, blue and green lines, respectively).

Figure 4.27 shows in a double logarithmic plot, the behavior of the transient SPV responses for the $AlN_xO_y$:H/*c*-Si(p) at 1.5 eV (826 nm) and 0.85 eV (1458 nm) of laser pulse excitation. At 1.5 eV (826 nm), the three samples have similar decay shapes but with different relaxation times. In the sub-bandgap excitation (0.85 eV, 1458 nm), the $AlN_xO_y$:H/*c*-Si(p) sample with 5 sccm of hydrogen flow at deposition has a faster decay than the other $AlN_xO_y$:H/*c*-Si(p) samples.

Figure 4.28 shows that at least two independent processes are present if the excitation above the bandgap energy is analyzed at an excitation wavelength of 810 nm at 1.53 eV. An approximation to two stretched exponential transients represent a slow process (I) and a fast process (II). According to the values of the stretched exponential parameters, a process I is independent of process II. The process I corresponds to the region dominated by the relaxation of charges excited and separated from localized trap states. Process II corresponds to the region dominated by the relaxation of charges excited from delocalized states in the bands.

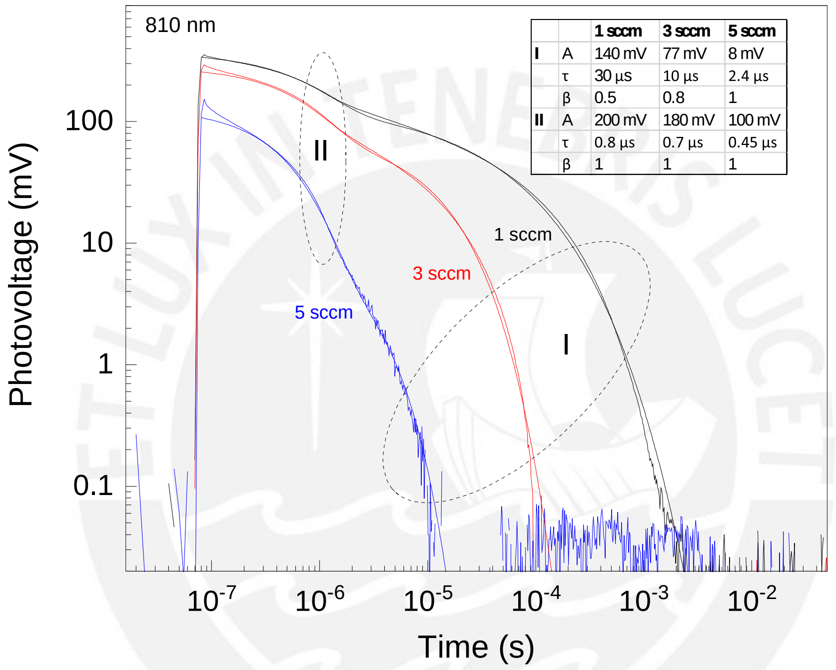

Figure 4.28: Two stretched exponential fits for SPV transients excited at 1.53 eV (810 nm) for samples deposited at 1, 3, and 5 sccm $H_2$ flow (black, red, and blue lines, respectively). The table shows the fitting parameters.

The slow process I has amplitudes, time constants, and stretching parameters of 140, 77, and 8 mV, of 30, 10, and 2.4 µs and 0.5, 0.8, and 1.0 for the $AlN_xO_y$:H/$c$-Si samples with 1, 3 and 5 sccm $H_2$ flow, respectively. The faster process II has amplitudes, time constants, and stretching parameters of 200, 180, and 100 mV, of 0.8, 0.7, and 0.45 µs, and of 1.0, 1.0, and 1.0 for the $AlN_xO_y$:H/$c$-Si samples which are prepared at 1, 3 and 5 sccm $H_2$ flow, respectively. The superposition principle allows the separation of these two independent processes. Process I is more dependent on the hydrogen flow at deposition, and process II is less dependent on the hydrogen flow at deposition. This analysis complements the energy tails and offsets observations.

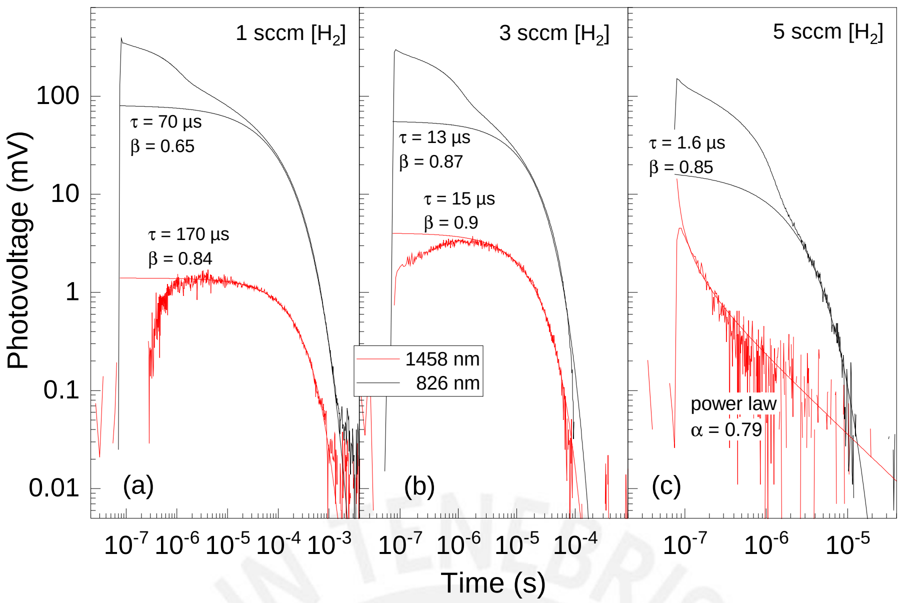

Figure 4.29: Stretched exponential fits for SPV transients excited at 1.50 eV (826 nm, black lines) and 0.85 eV (1458 nm, red lines) for *c*-Si/AlN$_x$O$_y$:H samples prepared with H$_2$ flow of 1 and 3 sccm; a) and b), respectively. Stretched exponential fit for SPV transients excited at 1.50 eV (826 nm) and power law fit at 0.85 eV (1458 nm) for *c*-Si/AlN$_x$O$_y$:H samples prepared with H$_2$ flow of 5 sccm; c).

Stretched exponentials were used to fit the slowly decaying parts of the SPV transients over roughly the last decade. As a result of the experiments with AlN$_x$O$_y$:H layers deposited at 1, 3, and 5 sccm, the time constants ($\tau$) and stretching parameters ($\beta$) were 70 µs and 0.65, 13 µs and 0.87, and 1.6 µs and 0.85, respectively (excitation at 826 nm with an energy of 1.864 eV).

Transients excited from deep defect states (see Figure 4.30) had a dominant positive signal component. In addition, stretched exponentials were used to fit the positive parts of the samples deposited at H$_2$ flow 1 and 3 sccm with t and b of 170 µs and 0.84 and 15 µs and 0.9, respectively (excitation at 1458 nm with 0.85 eV photon energy). For the sample with the AlN$_x$O$_y$:H layer deposited at 5 sccm and excited at the same photon energy, the transient could be fitted by a power law equal to 0.79.

The slower parts of the SPV transients had a similar dependence on the $t_{relax}$ as the normalized offsets. Normalized offsets also correlated with the fastest and slowest decays of SPV transients. This correlation means that the density of deep defect states limits the relaxation of SPV transients at longer times.

A hydrogen plasma treatment of crystalline silicon causes hydrogen to diffuse into the bulk of silicon, potentially causing defects. A disordered surface layer is formed during prolonged plasma treatment [41]. As demonstrated by the passivation of boron acceptors after the deposition of AlN$_x$O$_y$:H layers, hydrogen plasma was also present during the growth of $AlN_xO_y$:H layers. Increased $H_2$ flow led to higher offsets normalized to $SPV_{max}$ and a decrease in the slowest relaxation time, resulting in denser deep defect states (dangling bonds). It has been observed that the number of holes transferred from *c*-Si into surfaces at/near the surface increases with increasing defects density. In agreement with the observed reduction of $SPV_{max}$ with increasing $H_2$ flow, this increases partial screening of $Q_{fix(-)}$ by positively charged states at/near the interface.

Hydrogen incorporation causes stress between silicon bonds in addition to dangling bonds. The presence of exponential tails signifies weakened bonds or disorder [105]. Assuming strong accumulation, all defect states near the surface of *c*-Si(p) will be unoccupied in the idealized case. $E_t$ is mainly characterized by exponential tails below the conduction band edge of the sample with the $AlN_xO_y$:H layer deposited at $H_2$ flow equal to 1 sccm. With increasing trap energy, trapped electrons are less likely to escape via thermal excitation into the conduction band. Consequently, $E_t$ increased as $t_{relax}$ increased.

When defect states are densely populated, charge transfer between them becomes feasible (hopping transport). As SPV transients decay according to a power law, the relaxation of charge carriers separated in space is limited by an exponential distribution of localized states in energy [51]. The calculated values of $E_t$ range from 28 to 33 meV, which are in good agreement with the measured values. The slowest relaxation of charge carriers separated in space was limited by hopping transport over defects with an exponential energy distribution for the sample with an $AlN_xO_y$:H layer deposited at $H_2$ flow of 5 sccm.

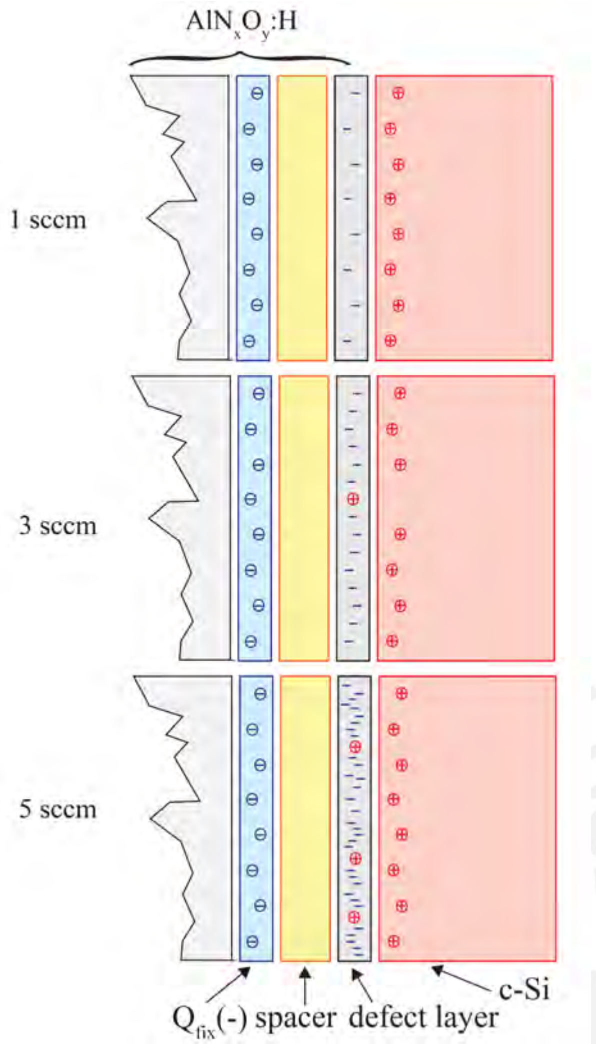

Figure 4.30: Idealized 4-layer-model for samples deposited at 1 sccm, 3 sccm, and, 5 sccm of $H_2$ flow at deposition of AlN$_x$O$_y$:H on *c*-Si(p) samples.

Figure 4.30 proposes layer models for the different distribution of defects for the AlN$_x$O$_y$:H on *c*-Si(p) samples, considering the analysis of the $E_t$ and the offset at different relaxation times. The density of defects at the AlN$_x$O$_y$:H on *c*-Si(p) sample with 5 sccm is noticeably higher than the other samples, and the distance among defects is close enough to have hoping transport (about the tunneling distance).

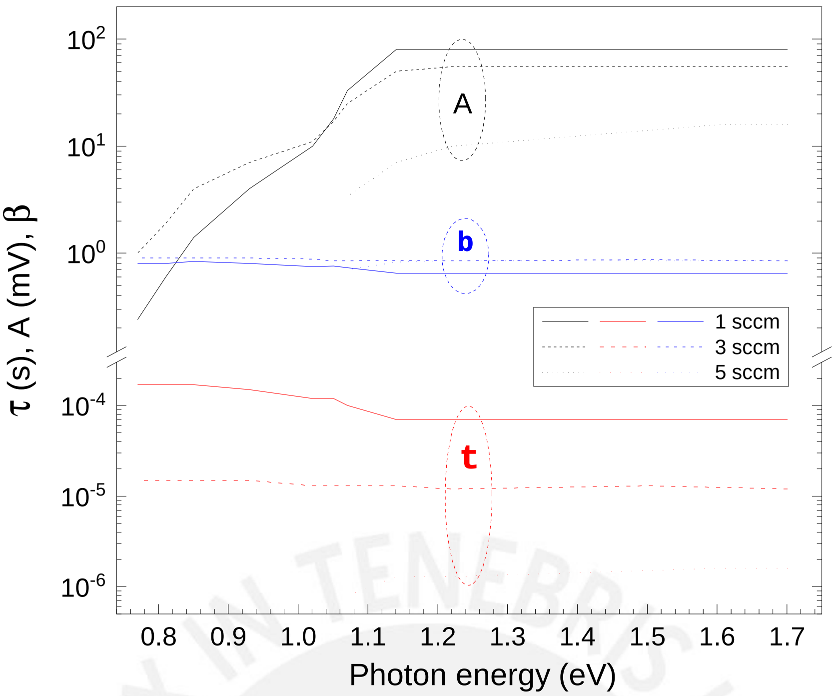

Figure 4.31: Variation of stretched exponential parameters (A, $\beta$ and $\tau$; black, red and blue lines, respectively) with photon energy (eV) for samples deposited at 1, 3 and 5 sccm (solid, dashed and short dashed lines, respectively).

Figure 4.31 shows the variation of the exponential parameter (A, $\beta$ and $\tau$) by photon energy (eV). These parameters have steady values for photon energies greater than the bandgap energy because at super bandgap transitions, the photogenerated carriers are mobile, and at sub-bandgap, part of the photogenerated carriers are localized. At the sub-bandgap regime, the parameters start to differ considerably. This effect is because all defects are excited at super-bandgap energies, and at sub-bandgap excitation, the excited defects depend on their energy distribution.

### 4.3.7 Hypothetical band diagrams of the bare silicon sample and the AlN$_x$O$_y$:H/$c$-Si samples

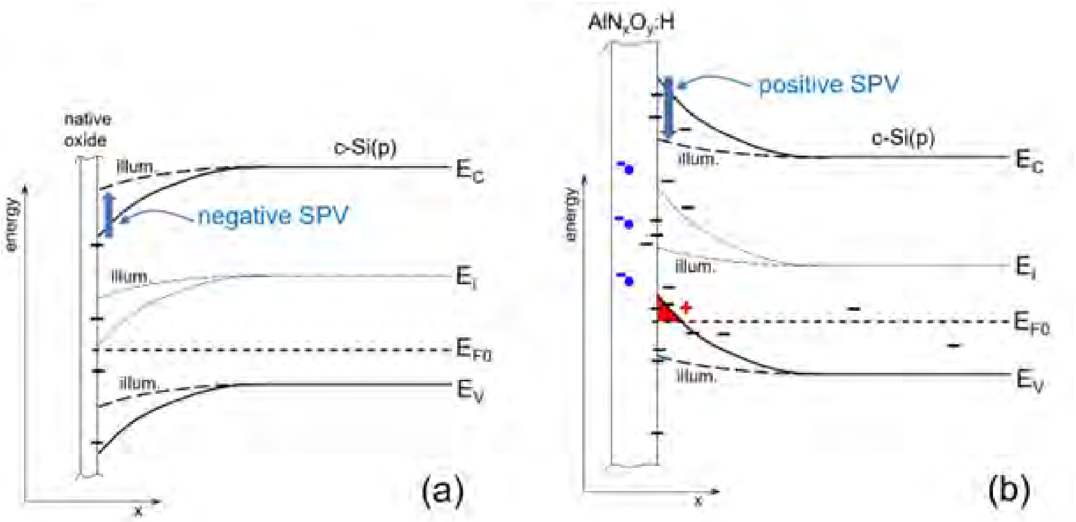

Figure 4.32: Final hypothetical band diagram taking into account the passivation of Boron acceptors [74]

Figure 4.32 describes the electronic properties of the AlN$_x$O$_y$:H/$c$-Si interfaces more accurately. The passivation of silicon atoms doped with boron is taken into account in the AlN$_x$O$_y$:H/$c$-Si band diagram as a $E_{F0}$ positive shift. The fixed negative charges at the AlN$_x$O$_y$:H layer bend the diagrams downward when it is illuminated (strong accumulation). The defects generation among the three AlN$_x$O$_y$:H/$c$-Si samples changes their SPV$_{max}$ (change in the $Q_{fix-net}$) and the relaxation timing.

# Chapter 5

# Summary and outlook

The generation of defects at Tb-doped $\mathrm{AlN}_x\mathrm{O}_y$:H / $c$-Si interfaces depended sensitively on the concentration of hydrogen during the $\mathrm{AlN}_x\mathrm{O}_y$:H layer deposition, and, aside from hydrogen passivation of Si interfaces, defect formation was a dominant contributor to the electronic properties at the interface. The extraction of defect concentrations and more detailed defect distributions in space and energy is still challenging since there are no available reliable simulation tools for SPV transients to date. The introduction of properties lumped to a geometric interface as tried for a-Si/$c$-Si heterojunctions [106] is not reliable in this case since charge transfer processes via localized states must be considered in a model for transient SPV spectroscopy at $\mathrm{AlN}_x\mathrm{O}_y$:H / $c$-Si(p) interfaces.

It has been demonstrated on the example of acceptor passivation and defect generation near $\mathrm{AlN}_x\mathrm{O}_y$:H / $c$-Si(p) interfaces that transient SPV spectroscopy provides access to electronic properties of buried interfaces of $c$-Si.

The main goal of transient SPV spectroscopy is to give reliable information of buried interfaces even under conditions where other methods like HF-CV or QSSPC are not able to offer conclusive information about the electronic properties of the interfaces. The range of time (up 12 orders of magnitude [107]) also can give additional information about the relaxation times of different processes involved (slow and fast).

With the appropriate mathematical tools like fitting with stretched exponential, it is possible to isolate processes that give SPV signals. In general, the scope of transient SPV analysis is extensive, and with other complementary measurement techniques, it is possible to arrive at substantial conclusions about the interfaces.

The optical properties of the Tb-doped $\mathrm{AlN}_x\mathrm{O}_y$:H can be studied in parallel with the electronic properties in order to obtain the best optimization due to electronic passivation, optical adaptation (downshift, down conversion), and antireflection accommodation.

This parallel study could arrive at the development of an electronic and an optical-optimized photovoltaic cell. For the case of electronic properties, the main technique should be transient SPV spectroscopy.

The downshift and down conversion layer are in constant study as in [22, 23, 27] while the electronic properties of the interface $\mathrm{AlO}_x\mathrm{N}_x$:H/$c$-Si are barely studied as in [14, 17] where effects like the passivation of acceptors and generation of defects by hydrogen are not taking in account.

Transient SPV provides additional information for the interface $AlO_xN_x$:H/$c$-Si such as the dynamics of the charge carriers relaxation and the energy tails that give an idea of the disorder at/near the interface. Taking in account this extra information, it is possible to design new experiments in order to eliminate constraints for passivation.

As an example, it is possible to change the conditions of the sputtering deposition, reducing the hydrogen flow during deposition and reducing the power, and verifying the new passivation condition by transient SPV, making SPV a potential technique for the analysis of passivation layers.

# Bibliography

[1] M. Green, E. Dunlop, J. Hohl-Ebinger, M. Yoshita, N. Kopidakis, X. Hao, Solar cell efficiency tables (version 57), Prog. Photovoltaics Res. Appl. 29 (2021) 3–15. (`https://doi.org/10.1002/pip.3371`).

[2] J. Liu, Y. Yao, S. Xiao, X. Gu, Review of status developments of high-efficiency crystalline silicon solar cells, J. Phys. D. Appl. Phys. 51 (2018). (`https://doi.org/10.1088/1361-6463/aaac6d`).

[3] L.C. Andreani, A. Bozzola, P. Kowalczewski, M. Liscidini, L. Redorici, Silicon solar cells: Toward the efficiency limits, Adv. Phys. X. 4 (2019). (`https://doi.org/10.1080/23746149.2018.1548305`).

[4] A.G. Aberle, Surface passivation of crystalline silicon solar cells: a review, Prog. Photovoltaics Res. Appl. 8 (2000) 473–487. (`https://doi.org/10.1002/1099-159X(200009/10)8:5<473::AID-PIP337>3.0.CO;2-D`).

[5] G. Dingemans, E. Kessels, Status and prospects of Al 2O 3-based surface passivation schemes for silicon solar cells, J. Vac. Sci. Technol. A Vacuum, Surfaces Film. 30 (2012) 1–27. (`https://doi.org/10.1116/1.4728205`).

[6] R.S. Bonilla, B. Hoex, P. Hamer, P.R. Wilshaw, Dielectric surface passivation for silicon solar cells: A review, Phys. Status Solidi Appl. Mater. Sci. 214 (2017) 1–30. (`https://doi.org/10.1002/pssa.201700293`).

[7] J. Schmidt, R. Peibst, R. Brendel, Surface passivation of crystalline silicon solar cells: Present and future, Sol. Energy Mater. Sol. Cells. 187 (2018) 39–54. (`https://doi.org/10.1016/j.solmat.2018.06.047`).

[8] Y. Lee, C. Park, N. Balaji, Y.J. Lee, V.A. Dao, High-efficiency Silicon Solar Cells: A Review, Isr. J. Chem. 55 (2015) 1050–1063. (`https://doi.org/10.1002/ijch.201400210`).

[9] S.W. Glunz, F. Feldmann, $SiO_2$ surface passivation layers – a key technology for silicon solar cells, Sol. Energy Mater. Sol. Cells. 185 (2018) 260–269. (`https://doi.org/10.1016/j.solmat.2018.04.029`).

[10] J. Yoo, J. So, G. Yu, J. Yi, Study on hydrogenated silicon nitride for application of high efficiency crystalline silicon solar cells, Sol. Energy Mater. Sol. Cells. 95 (2011) 7–10. (`https://doi.org/10.1016/j.solmat.2010.03.031`).

[11] T.T. Li, A. Cuevas, Effective surface passivation of crystalline silicon by rf sputtered aluminum oxide, Phys. Status Solidi - Rapid Res. Lett. 3 (2009) 160–162. (`https://doi.org/10.1002/pssr.200903140`).

[12] A. Morato, B. Vermang, H. Goverde, E. Cornagliotti, G. Meneghesso, J. John, J. Poortmans, Electrical characterization of ALD $Al_2O_3$ - $HfO_2$ and PECVD $Al_2O_3$ passivation layers for p-type CZ-Silicon PERC solar cells, Conf. Rec. IEEE Photovolt. Spec. Conf. (2012) 1077–1082. (`https://doi.org/10.1109/PVSC.2012.6317790`).

[13] D.K. Simon, P.M. Jordan, T. Mikolajick, I. Dirnstorfer, On the Control of the Fixed Charge Densities in $Al_2O_3$-Based Silicon Surface Passivation Schemes, ACS Appl. Mater. Interfaces. 7 (2015) 28215–28222. (`https://doi.org/10.1021/acsami.5b06606.`)

[14] G. Krugel, A. Sharma, A. Moldovan, W. Wolke, J. Rentsch, R. Preu, Passivation of solar cell emitters using aluminum nitride, Conf. Rec. IEEE Photovolt. Spec. Conf. (2013) 1249–1253. (`https://doi.org/10.1109/PVSC.2013.6744367`).

[15] J. Dulanto, M.A. Sevillano-Bendezu, R. Grieseler, J.A. Guerra, L. Korte, T. Dittrich, J.A. Töfflinger, Silicon interface passivation studied by modulated surface photovoltage spectroscopy, J. Phys. Conf. Ser. 1841 (2021). (`https://doi.org/10.1088/1742-6596/1841/1/012003`).

[16] Y. Xing, P. Han, S. Wang, P. Liang, S. Lou, Y. Zhang, S. Hu, H. Zhu, C. Zhao, Y. Mi, A review of concentrator silicon solar cells, Renew. Sustain. Energy Rev. 51 (2015) 1697–1708. (`https://doi.org/10.1016/j.rser.2015.07.035`).

[17] G. Krugel, A. Sharma, W. Wolke, J. Rentsch, R. Preu, Study of hydrogenated AlN as an anti-reflective coating and for the effective surface passivation of silicon, Phys. Status Solidi - Rapid Res. Lett. 7 (2013) 457–460. (`https://doi.org/10.1002/pssr.201307153`).

[18] G. Krugel, F. Jenkner, A. Moldovan, W. Wolke, J. Rentsch, R. Preu, Investigations on the passivation mechanism of AlN:H and AlN:H-SiN:H stacks, Energy Procedia. 55 (2014) 797–804. (`https://doi.org/10.1016/j.egypro.2014.08.062`).

[19] P. Repo, Y. Bao, H. Seppanen, P. Sippola, H. Savin, Silicon surface passivation with atomic layer deposited aluminum nitride, 2016 IEEE 43th Photovolt. Spec. Conf. PVSC 2016. (2016) 2967–2970. (`https://doi.org/https://doi.org/10.1109/PVSC.2016.7750205`).

[20] L. Montañez, J.A. Töfflinger, R. Grieseler, P. Fischer, A. Ben-Or, J.A. Guerra, R. Weingärtner, H.J. Osten, A. Kribus, Structural, optical, and interface properties of sputtered AlN thin films under different hydrogen dilution conditions, Mater. Today Proc. 5 (2018) 14765–14771. (`https://doi.org/10.1016/j.matpr.2018.03.066`).

[21] P.K. Parashar, S.A. Kinnunen, T. Sajavaara, J.J. Toppari, V.K. Komarala, Thermal atomic layer deposition of . $AlO_xN_y$ thin films for surface passivation of nano-textured flexible silicon, Sol. Energy Mater. Sol. Cells. 193 (2019) 231–236. (`https://doi.org/10.1016/j.solmat.2019.01.019`).

[22] K.Y. Tucto, W. Aponte, J.A. Dulanto, J.A. Töfflinger, J.A. Guerra, R. Grieseler, Combinatorial approach toward optimization of the light emission intensity of $AlO_xN_y$:$Yb^{3+}$ thin films, Appl. Opt. 58 (2019) 3097–3103. (`https://doi.org/10.1364/ao.58.003097`).

[23] K.Y. Tucto Salinas, L.F. Flores Escalante, J.A. Guerra Torres, R. Grieseler, T. Kups, J. Pezoldt, A. Osvet, M. Batentschuk, R. Weingärtner, Effect of post-annealing treatment on the structure and luminescence properties of AIN: $Tb^{3+}$ thin films prepared by radio frequency magnetron sputtering, Mater. Sci. Forum. 890 MSF (2017) 299–302. (`https://doi.org/10.4028/www.scientific.net/MSF.890.299`).

[24] L. Dumont, J. Cardin, C. Labbé, C. Frilay, P.M. Anglade, I.S. Yu, M. Vallet, P. Benzo, M. Carrada, D. Stiévenard, H. Merabet, F. Gourbilleau, First down converter multilayers integration in an industrial Si solar cell process, Prog. Photovoltaics Res. Appl. 27 (2019) 152–162. (`https://doi.org/10.1002/pip.3071`).

[25] L. Dumont, J. Cardin, P. Benzo, M. Carrada, C. Labbé, A.L. Richard, D.C. Ingram, W.M. Jadwisienczak, F. Gourbilleau, $SiN_x$:$Tb^{3+}$-$Yb^{3+}$, an efficient down-conversion layer compatible with a silicon solar cell process, Sol. Energy Mater. Sol. Cells. 145 (2016) 84–92. (`https://doi.org/10.1016/j.solmat.2015.09.031`).

[26] H.Q. Wang, M. Batentschuk, A. Osvet, L. Pinna, C.J. Brabec, Rare-earth ion doped up-conversion materials for photovoltaic applications, Adv. Mater. 23 (2011) 2675–2680. (`https://doi.org/10.1002/adma.201100511`).

[27] K. Tucto, L. Flores, J. Guerra, J. Töfflinger, J. Dulanto, R. Grieseler, A. Osvet, M. Batentschuk, R. Weingärtner, Production and Characterization of $Tb^{3+}/Yb^{3+}$ Co-Activated AlON Thin Films for Down Conversion Applications in Photovoltaic Cells, in: MRS Adv., Materials Research Society, 2017: pp. 2989–2995. (`https://doi.org/10.1557/adv.2017.478`).

[28] F. Benz, T. Walther, H.P. Strunk, Towards the structure of rare earth luminescence centres-terbium doped aluminium nitride as an example system, J. Phys. Conf. Ser. 471 (2013). (`https://doi.org/10.1088/1742-6596/471/1/012032`).

[29] F.S. Liu, W.J. Ma, Q.L. Liu, J.K. Liang, J. Luo, L.T. Yang, G.B. Song, Y. Zhang, G.H. Rao, Photoluminescence and characteristics of terbium-doped AlN film prepared by magnetron sputtering, Appl. Surf. Sci. 245 (2005) 391–399. (`https://doi.org/10.1016/j.apsusc.2004.10.034`).

[30] J.I. Pankove, Chapter 3 Hydrogenation of Defects in Crystalline Silicon, Semicond. Semimetals. 34 (1991) 35–47. (`https://doi.org/10.1016/S0080-8784(08)62858-6`).

[31] H. MäcKel, R. Lüdemann, Detailed study of the composition of hydrogenated $\mathrm{SiN}_x$ layers for high-quality silicon surface passivation, J. Appl. Phys. 92 (2002) 2602–2609. (`https://doi.org/10.1063/1.1495529`).

[32] A. Masuda, C. Niikura, Y. Ishibashi, H. Matsumura, Dominant parameter determining dangling-bond density in hydrogenated amorphous silicon films prepared by catalytic chemical vapor deposition, Sol. Energy Mater. Sol. Cells. 66 (2001) 259–265. (`https://doi.org/10.1016/S0927-0248(00)00182-3`).

[33] M. Bruel, Separation of silicon wafers by the smart-cut method, Mater. Res. Innov. 3 (1999) 9–13. (`https://doi.org/10.1007/s100190050119`).

[34] J.A. Guerra, F. De Zela, K. Tucto, L. Montañez, J.A. Töfflinger, A. Winnacker, R. Weingärtner, Effect of thermal annealing treatments on the optical activation of Tb3+-doped amorphous SiC:H thin films, J. Phys. D. Appl. Phys. 49 (2016) 375104. (`https://doi.org/10.1088/0022-3727/49/37/375104`).

[35] J.A. Guerra, J.R. Angulo, S. Gomez, J. Llamoza, L.M. Montañez, A. Tejada, J.A. Töfflinger, A. Winnacker, R. Weingärtner, The Urbach focus and optical properties of amorphous hydrogenated SiC thin films, J. Phys. D. Appl. Phys. 49 (2016) 195102.. (`https://doi.org/10.1088/0022-3727/49/19/195102`).

[36] J.I. Pankove, R.O. Wance, J.E. Berkeyheiser, Neutralization of acceptors in silicon by atomic hydrogen, Appl. Phys. Lett. 45 (1984) 1100–1102. (`https://doi.org/10.1063/1.95030`).

[37] N.M. Johnson, C. Herring, D.J. Chadi, Interstitial hydrogen and neutralization of shallow-donor impurities in single-crystal silicon, Phys. Rev. Lett. 56 (1986) 769–772. (`https://doi.org/10.1103/PhysRevLett.56.769`).

[38] J. Weber, S. Knack, O. V. Feklisova, N.A. Yarykin, E.B. Yakimov, Hydrogen penetration into silicon during wet-chemical etching, Microelectron. Eng. 66 (2003) 320–326. (`https://doi.org/10.1016/S0167-9317(02)00926-7`).

[39] A. Castaldini, D. Cavalcoli, A. Cavallini, E. Susi, Hydrogen-induced boron passivation in Cz Si, Appl. Phys. A Mater. Sci. Process. 75 (2002) 601–605. (`https://doi.org/10.1007/s003390101067`).

[40] B. Stegemann, P. Balamou, T. Lussky, K.M. Gad, D. Vossing, M. Kasemann, H. Angermann, Passivation of Crystalline Silicon Wafers by Ultrathin Oxide Layers: Comparison of Wet-chemical, Plasma and Thermal Oxidation Techniques, 2018 IEEE 7th World Conf. Photovolt. Energy Conversion, WCPEC 2018 - A Jt. Conf. 45th IEEE PVSC, 28th PVSEC 34th EU PVSEC. (2018) 2779–2782. (`https://doi.org/10.1109/PVSC.2018.8548154`).

[41] S. Nunomura, I. Sakata, K. Matsubara, Formation of electronic defects in crystalline silicon during hydrogen plasma treatment, AIP Adv. 9 (2019) 045110. (`https://doi.org/10.1063/1.5089202`).

[42] J. Steffens, M.A. Fazio, D. Cavalcoli, B. Terheiden, Multi-characterization study of interface passivation quality of amorphous sub-stoichiometric silicon oxide and silicon oxynitride layers for photovoltaic applications, Sol. Energy Mater. Sol. Cells. 187 (2018) 104–112. (`https://doi.org/10.1016/j.solmat.2018.07.024`).

[43] T. Dittrich, L.E. Valle Rios, S. Kapil, G. Gurieva, N. Rujisamphan, S. Schorr, Temperature dependent transient surface photovoltage spectroscopy of a Cu1.95Zn1.1Sn0.96Se4 kesterite single phase powder, Appl. Phys. Lett. 110 (2017) 023901. (`https://doi.org/10.1063/1.4973539`).

[44] S. Fengler, H. Kriegel, M. Schieda, H. Gutzmann, T. Klassen, M. Wollgarten, T. Dittrich, Charge Transfer in c-Si(n++)/$TiO_2$(ALD) at the Amorphous/Anatase Transition: A Transient Surface Photovoltage Spectroscopy Study, ACS Appl. Mater. Interfaces. 12 (2020) 3140–3149. (`https://doi.org/10.1021/acsami.9b17592`9.

[45] K.J. Yang, C. Hu, MOS capacitance measurements for high-leakage thin dielectrics, IEEE Trans. Electron Devices. 46 (1999) 1500–1501. (`https://doi.org/10.1109/16.772500`).

[46] J.A. Töfflinger, A. Laades, L. Korte, C. Leendertz, L.M. Montañez, U. Stürzebecher, H.P. Sperlich, B. Rech, PECVD-$AlO_x$/$SiN_x$ passivation stacks on wet chemically oxidized silicon: Constant voltage stress investigations of charge dynamics and interface defect states, Sol. Energy Mater. Sol. Cells. 135 (2015) 49–56. (`https://doi.org/10.1016/j.solmat.2014.09.024`).

[47] V. Dimitrova, D. Manova, T. Paskova, T. Uzunov, N. Ivanov, D. Dechev, Aluminium nitride thin films deposited by DC reactive magnetron sputtering, Vacuum. 51 (1998) 161–164. (`https://doi.org/10.1016/S0042-207X(98)00150-X`).

[48] M. Ishihara, S.. Li, H. Yumoto, K. Akashi, Y. Ide, Control of preferential orientation of AlN films prepared by the reactive sputtering method, Thin Solid Films. 316 (1998) 152–157. (`https://doi.org/10.1016/S0040-6090(98)00406-4`).

[49] J. Hyoung, J. Yong, J. Hyeok, Phase evolution in aluminum nitride thin films on Si (100). prepared by radio frequency magnetron sputtering, Thin Solid Films. 384 (2001) 166–172.

[50] Z. Vashaei, T. Aikawa, M. Ohtsuka, H. Kobatake, H. Fukuyama, S. Ikeda, K. Takada, Influence of sputtering parameters on the crystallinity and crystal orientation of AlN layers deposited by RF sputtering using the AlN target, J. Cryst. Growth. 311 (2009) 459–462. (`https://doi.org/10.1016/j.jcrysgro.2008.09.046`).

[51] T. Dittrich, S. Fengler, Surface Photovoltage Analysis of Photoactive Materials, World Scientific, Singapore, 2020.

[52] L. Kronik, Y. Shapira, Surface photovoltage phenomena: Theory, experiment, and applications, Surf. Sci. Rep. 37 (1999) 1–206. (`https://doi.org/10.1016/S0167-5729(99)00002-3`).

[53] D. Cavalcoli, A. Cavallini, Surface photovoltage spectroscopy - method and applications, Phys. Status Solidi. 7 (2010) 1293–1300. (`https://doi.org/10.1002/pssc.200983124`).

[54] V. Donchev, Surface photovoltage spectroscopy of semiconductor materials for optoelectronic applications, Mater. Res. Express. 6 (2019). (`https://doi.org/10.1088/2053-1591/ab3bf0`).

[55] P.M. Jordan, D.K. Simon, T. Mikolajick, I. Dirnstorfer, Trapped charge densities in Al2O3-based silicon surface passivation layers, J. Appl. Phys. 119 (2016). (`https://doi.org/10.1063/1.4953141`).

[56] A.G. Aberle, S.W. Glunz, W. Warta, Field effect passivation of high efficiency silicon solar cells, 29 (1993) 175–182.

[57] S.W. Glunz, D. Biro, S. Rein, W. Warta, Field-effect passivation of the SiO2-Si interface, J. Appl. Phys. 86 (1999) 683–691. (`https://doi.org/10.1063/1.370784`).

[58] S.M. Sze, M.K. Lee, No Title, n.d.

[59] W. Shockley, W.T. Read, Statistics of the recombinations of holes and electrons, Phys. Rev. 87 (1952) 835–842. (`https://doi.org/10.1103/PhysRev.87.835`).

[60] G. Dingemans, W.M.M. Kessels, Status and prospects of $Al_2O_3$ -based surface passivation schemes for silicon solar cells, J. Vac. Sci. Technol. A Vacuum, Surfaces, Film. 30 (2012) 040802. (`https://doi.org/10.1116/1.4728205`).

[61] R.N. Hall, Electron-Hole Recombination, (n.d.) 6.

[62] E. Lebedev, T. Dittrich, V. Petrova-Koch, S. Karg, W. Brütting, Charge carrier mobility in poly(p-phenylenevinylene) studied by the time-of-flight technique, Appl. Phys. Lett. 71 (1997) 2686–2688. (`https://doi.org/10.1063/1.120179`).

[63] E. Von Hauff, V. Dyakonov, J. Parisi, Study of field effect mobility in PCBM films and P3HT:PCBM blends, Sol. Energy Mater. Sol. Cells. 87 (2005) 149–156. (`https://doi.org/10.1016/j.solmat.2004.06.014`).

[64] J.M. Marshall, R.A. Street, M.J. Thompson, Electron drift mobility in amorphous Si:H, Philos. Mag. B Phys. Condens. Matter; Stat. Mech. Electron. Opt. Magn. Prop. 54 (1986) 51–60. (`https://doi.org/10.1080/13642818608243177`).

[65] C. Jacoboni, C. Canali, G. Ottaviani, A. Alberigi Quaranta, A review of some charge transport properties of silicon, Solid State Electron. 20 (1977) 77–89. (`https://doi.org/10.1016/0038-1101(77)90054-5`9.

[66] Z. Zhang, J.T. Yates, Band bending in semiconductors: Chemical and physical consequences at surfaces and interfaces, Chem. Rev. 112 (2012) 5520–5551. (`https://doi.org/10.1021/cr3000626`).

[67] A.R. Zanatta, Effect of thermal annealing treatments on the optical properties of rare-earth-doped AlN films, J. Phys. D. Appl. Phys. 42 (2009). (`https://doi.org/10.1088/0022-3727/42/2/025109`).

[68] R. Grieseler, T. Kups, M. Wilke, M. Hopfeld, P. Schaaf, Formation of Ti2AlN nanolaminate films by multilayer-deposition and subsequent rapid thermal annealing, Mater. Lett. 82 (2012) 74–77. (`https://doi.org/https://doi.org/10.1016/j.matlet.2012.05.055`).

[69] U. Hansen, P. Vogl, Hydrogen passivation of silicon surfaces: A classical molecular-dynamics study, Phys. Rev. B - Condens. Matter Mater. Phys. 57 (1998) 13295–13304. (`https://doi.org/10.1103/PhysRevB.57.13295`).

[70] L. Song, D. Yang, X. Yu, Investigation on the impact of hydrogen on the passivation of silicon surface states in clean and copper contaminated conditions, AIP Adv. 9 (2019). (`https://doi.org/10.1063/1.5122253`).

[71] Romanus, Henry: Siliziumkarbidelektronik - technologische und werkstoffwissenschaftliche Untersuchungen zur Metallisierung/Kontaktierung, Technische Universität Ilmenau, Diss., 2003

[72] S. Fengler, T. Dittrich, M. Schieda, H. Gutzmann, T. Emmler, M. Villa-Vidaller, T. Klassen, Characterization of BiVO4 powders and cold gas sprayed by surface photovoltage techniques, Catalysis Today 321-322 (2019) 34-40. (`https://doi.org/10.1016/j.cattod.2018.02.027`).

[73] I. Levine, O.G. Vera, M. Kulbak, D.R. Ceratti, C. Rehermann, J.A. Márquez, S. Levcenko, T. Unold, G. Hodes, I. Balberg, D. Cahen, T. Dittrich, Deep Defect States in Wide-Band-Gap ABX 3 Halide Perovskites, ACS Energy Lett. 4 (2019) 1150–1157. (`https://doi.org/10.1021/acsenergylett.9b00709`).

[74] J. Dulanto, S. Fengler, M.A. Sevillano-bendezú, R. Grieseler, J.A. Guerra, Hydrogen effects at sputtered Tb-doped $AlN_xO_y$:H/*c*-Si ( p ) interfaces: A transient surface photovoltage spectroscopy study. Thin Solid Films, 759 (2022). (`https://doi.org/10.1016/j.tsf.2022.139474`).

[75] S. Watanabe, In-situ infrared characterization of a chemically oxidized silicon surface dissolving in aqueous hydrofluoric acid, Surf. Sci. 341 (1995) 304–310. (`https://doi.org/10.1016/0039-6028(95)00672-9`).

[76] H. Schumacher, U. Künzelmann, B. Vasilev, K.J. Eichhorn, J.W. Bartha, Applications of microstructured silicon wafers as internal reflection elements in attenuated total reflection Fourier transform infrared spectroscopy, Appl. Spectrosc. 64 (2010) 1022–1027. (`https://doi.org/10.1366/000370210792434404`9.

[77] H.J. Lozykowski, W.M. Jadwisienczak, Thermal quenching of luminescence and isovalent trap model for rare-earth-ion-doped AlN, Phys. Status Solidi Basic Res. 244 (2007) 2109–2126. (`https://doi.org/10.1002/pssb.200642152`).

[78] A. Janotta, M. Schmidt, R. Janssen, M. Stutzmann, C. Buchal, Photoluminescence of Er3+-implanted amorphous hydrogenated silicon suboxides, Phys. Rev. B - Condens. Matter Mater. Phys. 68 (2003) 1–17. (`https://doi.org/10.1103/PhysRevB.68.165207`).

[79] D.B. Fenner, D.K. Biegelsen, R.D. Bringans, Silicon surface passivation by hydrogen termination: A comparative study of preparation methods, J. Appl. Phys. 66 (1989) 419–424. (`https://doi.org/10.1063/1.343839`).

[80] R. Roychowdhury, V.K. Dixit, G. Vashisht, T.K. Sharma, C. Mukherjee, S.K. Rai, S. Kumar, Surface and interface properties of $ZrO_2$ /GaAs, $SiO_2$ /GaAs and GaP/GaAs hetero structures investigated by surface photovoltage spectroscopy, Appl. Surf. Sci. 476 (2019) 615–622. (`https://doi.org/10.1016/j.apsusc.2019.01.103`).

[81] S.E. Challinger, I.D. Baikie, J.R. Harwell, G.A. Turnbull, ; Ifor, D.W. Samuel, An Investigation of the Energy Levels within a Common Perovskite Solar Cell Device and a Comparison of DC/AC Surface Photovoltage Spectroscopy Kelvin Probe Measurements of Different MAPBI 3 Perovskite Solar Cell Device Structures, MRS Advances (2017). (`https://doi.org/10.1557/adv.2017.72`)

[82] J. Zhao, B.A. Nail, M.A. Holmes, F.E. Osterloh, Use of Surface Photovoltage Spectroscopy to Measure Built-in Voltage, Space Charge Layer Width, and Effective Band Gap in CdSe Quantum Dot Films, J. Phys. Chem. Lett. 7 (2016) 3335–3340. (`https://doi.org/10.1021/acs.jpclett.6b01569`).

[83] S.D. Singh, S. Porwal, A.K. Sinha, T. Ganguli, Surface photovoltage spectroscopy of an epitaxial ZnO/GaP heterojunction, Semicond. Sci. Technol. 32 (2017). (`https://doi.org/10.1088/1361-6641/aa6424`).

[84] X. Wang, M. Juhl, M. Abbott, Z. Hameiri, Y. Yao, A. Lennon, Use of QSSPC and QSSPL to monitor recombination processes in p-type silicon solar cells, Energy Procedia. 55 (2014) 169–178. (`https://doi.org/10.1016/j.egypro.2014.08.110`).

[85] M. Goodarzi, R. Sinton, D. Macdonald, Quasi-steady-state photoconductance bulk lifetime measurements on silicon ingots with deeper photogeneration, AIP Adv. 9 (2019). (`https://doi.org/10.1063/1.5086378`).

[86] N. Preissler, D. Amkreutz, J. Dulanto, J.A. Töfflinger, C.T. Trinh, M. Trahms, D. Abou-Ras, H. Kirmse, R. Weingärtner, B. Rech, R. Schlatmann, Passivation of Liquid-Phase Crystallized Silicon With PECVD-SiNx and PECVD-SiNx/SiOx, Phys. Status Solidi Appl. Mater. Sci. 215 (2018). (`https://doi.org/10.1002/pssa.201800239`).

[87] N. Preissler, J.A. Töfflinger, O. Gabriel, P. Sonntag, D. Amkreutz, B. Stannowski, B. Rech, R. Schlatmann, Passivation at the interface between liquid-phase crystallized silicon and silicon oxynitride in thin film solar cells, Prog. Photovoltaics Res. Appl. 25 (2017) 515–524. (`https://doi.org/10.1002/pip.2852`).

[88] H. Angermann, Passivation of structured p-type silicon interfaces: Effect of surface morphology and wet-chemical pre-treatment, Appl. Surf. Sci. 254 (2008) 8067–8074. (`https://doi.org/10.1016/j.apsusc.2008.03.022`).

[89] W. Lu, C. Leendertz, L. Korte, J.A. Töfflinger, H. Angermann, Passivation properties of subnanometer thin interfacial silicon oxide films, Energy Procedia. 55 (2014) 805–812. (`https://doi.org/10.1016/j.egypro.2014.08.063`).

[90] J.A. Tofflinger, A. Laades, C. Leendertz, L.M. Montanez, L. Korte, U. Sturzebecher, H.P. Sperlich, B. Rech, PECVD-AlO$_x$/SiN$_x$ passivation stacks on silicon: Effective charge dynamics and interface defect state spectroscopy, Energy Procedia. 55 (2014) 845–854. (`https://doi.org/10.1016/j.egypro.2014.08.068`).

[91] I. Levine, G. Hodes, H.J. Snaith, P.K. Nayak, How to Avoid Artifacts in Surface Photovoltage Measurements: A Case Study with Halide Perovskites, J. Phys. Chem. Lett. 8 (2017) 2941–2943. (`https://doi.org/10.1021/acs.jpclett.7b01332`).

[92] T. Dittrich, M. Schwartzkopff, E. Hartmann, J. Rappich, On the origin of the positive charge on hydrogenated Si surfaces and its dependence on the surface morphology, Surf. Sci. 437 (1999) 154–162. (`https://doi.org/10.1016/S0039-6028(99)00712-8`).

[93] T. Dittrich, T. Burke, F. Koch, J. Rappich, Passivation of an anodic oxide/p-Si interface stimulated by electron injection, J. Appl. Phys. 89 (2001) 4636–4642. (`https://doi.org/10.1063/1.1356431`).

[94] C. Di Valentin, G. Palma, G. Pacchioni, Ab initio study of transition levels for intrinsic defects in silicon nitride, J. Phys. Chem. C. 115 (2011) 561–569. (`https://doi.org/10.1021/jp106756f`).

[95] W.L. Warren, J. Kanicki, E.H. Poindexter, Paramagnetic point defects in silicon nitride and silicon oxynitride thin films on silicon, Colloids Surfaces A Physicochem. Eng. Asp. 115 (1996) 311–317. (`https://doi.org/10.1016/0927-7757(96)03595-9`).

[96] W. Füssel, M. Schmidt, H. Angermann, G. Mende, H. Flietner, Defects at the Si/SiO2 interface: Their nature and behaviour in technological processes and stress, Nucl. Instruments Methods Phys. Res. Sect. A Accel. Spectrometers, Detect. Assoc. Equip. 377 (1996) 177–183. (`https://doi.org/10.1016/0168-9002(96)00205-7`).

[97] O.A. Dicks, J. Cottom, A.L. Shluger, V. V. Afanas'Ev, The origin of negative charging in amorphous Al 2 O 3 films: The role of native defects, Nanotechnology. 30 (2019) 1–14. (`https://doi.org/10.1088/1361-6528/ab0450`).

[98] E.O. Johnson, Large-Signal Surface Photovoltage Studies with Germanium, Phys. Rev. 111 (1958) 153–166. (`https://doi.org/10.1103/PhysRev.111.153`).

[99] T.-T.A. Li, A. Cuevas, Role of hydrogen in the surface passivation of crystalline silicon by sputtered aluminum oxide, Prog. Photovoltaics Res. Appl. 19 (2011) 320–325. (`https://doi.org/https://doi.org/10.1002/pip.1031`).

[100] H. Katto, Surface State Density Evaluation Using High-Frequency, 627 (1974).

[101] E.H. Nicollian, J.R. Brews, MOS (Metal Oxide Semiconductors) Physics and Technology, (1982). (`https://doi.org/10.1116/1.571867`).

[102] J.S. Thorp, D. Evans, M. Al-Naief, M. Akhtaruzzaman, The dielectric properties of aluminium nitride substrates for microelectronics packaging, J. Mater. Sci. 25 (1990) 4965–4971. (`https://doi.org/10.1007/BF00580114`).

[103] M.A. Sevillano-Bendezú, J.A. Dulanto, L.A. Conde, R. Grieseler, J.A. Guerra, J.A. Töfflinger, Capacitance voltage curve simulations for different passivation parameters of dielectric layers on silicon, J. Phys. Conf. Ser. 1433 (2020). (`https://doi.org/10.1088/1742-6596/1433/1/012007`).

[104] S. Kugler, What is the origin of tail states in amorphous semiconductors?, J. Phys. Conf. Ser. 253 (2010). (`https://doi.org/10.1088/1742-6596/253/1/012013`).

[105] J. Robertson, Deposition mechanism of hydrogenated amorphous silicon, J. Appl. Phys. 87 (2000) 2608–2617. (`https://doi.org/10.1063/1.372226`).

[106] L. Korte, A. Laades, K. Lauer, R. Stangl, D. Schaffarzik, M. Schmidt, Surface photovoltage investigation of recombination at the a-Si/c-Si heterojunction, Thin Solid Films. 517 (2009) 6396–6400. (`https://doi.org/10.1016/j.tsf.2009.02.090`).

[107] T. Dittrich, S. Fengler, M. Franke, Transient surface photovoltage measurement over 12 orders of magnitude in time, Rev. Sci. Instrum. 88 (2017) 053904. (`https://doi.org/10.1063/1.4983079`).